

ABSTRACT

Title of Dissertation: FINELY-DISCRETIZED LATTICE MODELS
FOR THERMODYNAMIC PROPERTIES OF FLUIDS

Sarvin Moghaddam, Doctor of Philosophy, 2003

Dissertation directed by: Professor Mikhail Anisimov
Department of Chemical Engineering
Institute for Physical Science and Technology
University of Maryland

Professor Athanassios Z. Panagiotopoulos
Department of Chemical Engineering
Princeton University

The demand for exploring thermodynamic and structural properties of complex fluids and their mixtures using molecular simulation methods sparks the need for efficient computational techniques. One such method is the fine-lattice discretization technique, for which these calculations can run up to two orders of magnitude faster than the off-lattice calculations. Generally, a major obstacle to simulating real systems is the computational time required for evaluating the potential energy. In fine-lattice discretization techniques, the potentials of intermolecular interactions are calculated once at the beginning of the simulation and are used repeatedly during the simulation. In this thesis, this technique is used along with grand canonical histogram reweighting Monte Carlo calculations to obtain the

coexistence properties of various non-polar and polar real and model fluids. Moreover, mixed-field finite-size scaling methods have been used to determine critical parameters of the systems studied.

New intermolecular potential models have been developed for diatomic molecules using off-lattice calculations to reproduce experimentally observed coexistence densities, vapor pressures, and critical parameters. The goal was to investigate an important problem in fine-lattice discretization technique, namely, how to build fine-lattice models reproducing properties of diatomic molecules and other systems of interest. The results reported indicate that it is possible to obtain a good description of the phase behavior of models of real systems such as nitrogen, carbon dioxide, and water over a broad range of temperatures. It has been observed that the structural properties of lattice models depend heavily on the lattice discretization parameter, which controls how closely the lattice system approaches the continuum behavior.

We have found that deviations of the critical temperatures are stronger by a factor of 5 for dipolar dumbbell model, compared to non-polar fluid models, “monomers” and “dimers” with one and two Buckingham exponential-6 sites, respectively. For the trimer model with quadrupolar interactions, the critical temperatures are less sensitive to the lattice discretization parameter.

The observed effect of the lattice discretization parameter on estimates for the thermodynamic and structural properties of fluids raises the need for a theoretical investigation. We have studied the subject analytically in one-dimensional space for a hard-core potential model and numerically for a hard-core with a square-well and a variety of logarithmic repulsive potentials. We have found that the smoothness of the repulsive part of the function is largely responsible for the speed of

convergence of critical parameters to their continuum counterparts. A numerical study of the two- and three-dimensional cases is presented and the dependence of the lattice discretization parameter on the number of lattice points contained within a hard-core sphere has been investigated. The distribution of the lattice points oscillates around a limiting form for the lattice discretization parameter.

FINELY-DISCRETIZED LATTICE MODELS
FOR THERMODYNAMIC PROPERTIES OF FLUIDS

by

Sarvin Moghaddam

Dissertation submitted to the Faculty of the Graduate School of the
University of Maryland, College Park in partial fulfillment
of the requirements for the degree of
Doctor of Philosophy
2003

Advisory Committee:

Professor Mikhail Anisimov, Chair/Advisor
Professor Athanassios Z. Panagiotopoulos, Co-Chair/Co-Advisor
Professor Michael E. Fisher
Professor Sandra C. Greer
Professor Jan V. Sengers

©Copyright by
Sarvin Moghaddam
2003

DEDICATION

To my beloved parents

and

to Majid, my husband and my best friend, for his limitless love and support.

ACKNOWLEDGEMENTS

I would like to thank my advisor, Professor Athanassios Z. Panagiotopoulos for his continuous support, advice and encouragement during my studies. He gave me the opportunity to work on different subjects and problems. His ideas and enthusiasm have made my research experience productive and enjoyable.

I would also like to thank Professor Michael E. Fisher for his guidance and collaboration particularly in the theoretical studies summarized in the last chapter of this dissertation. I learned a lot from him and it was my pleasure working with him. I also thank Professor Mikhail Anisimov for his help and advice throughout the final stage of my graduate studies. I am thankful to other members of the dissertation committee, Professor Jan V. Sengers and Professor Sandra C. Greer for kindly reviewing this dissertation and serving on my thesis committee. My thanks also go to my friends in Princeton University, Daniel Cheong, Phil Lenart, and Owen Hehmeyer, for their help while I was working remotely and had no access to my computer in Princeton. I am grateful to both Marilyn Spell and Caricia Claremont at the Institute for Physical Science and Technology for their help and support during my stay at the Institute for Physical Science and Technology. Funding for this research was provided by the Department of Energy, Office of Basic Energy Sciences (DE-FG0201ER15121). Additional support was provided by ACS-PRF (Grant No. 38165-AC9). I am also grateful for the one month support provided by Professor Mikhail Anisimov and Professor Jan V. Sengers through the Division of Chemical Sciences, Geosciences, and Biosciences, Office of

Basic Energy Sciences, Department of Energy under Grant No. DE-FG02-95ER-14509.

Last, but not least, I express my sincere gratitude to my parents for everything they did for me in my life and to my husband, Majid Raissi-Dehkordi, for his help and support throughout the wonderful years that I have spent with him. He was a source of inspiration during all these years for me and I am deeply indebted to him for his endless love and patience.

TABLE OF CONTENTS

List of Tables	viii
List of Figures	x
1 Introduction and Outline	1
2 Simulation Methodologies	5
2.1 Introduction	5
2.2 Molecular simulation methods	7
2.3 Grand canonical histogram reweighting Monte Carlo	8
2.4 Mixed-field finite-size scaling	11
2.5 Fine-lattice discretization method	15
2.6 Intermolecular potentials	17
3 Phase Equilibria of Diatomic Molecules and <i>N</i>-alkanes	22
3.1 Introduction	22
3.1.1 Diatomic molecules	22
3.1.2 <i>N</i> -alkanes	23
3.2 Models and simulation details	25
3.3 Results and discussion	27

3.3.1	<i>N</i> -butane	27
3.3.2	Diatomic molecules	31
3.4	Conclusions	37
4	Phase Equilibria of Real Non-polar and Polar Fluids	38
4.1	Polar fluids, carbon dioxide and water	38
4.2	Model development and methods	42
4.3	Results and discussion	46
4.3.1	Nitrogen model	46
4.3.2	Carbon dioxide model	47
4.3.3	Water model	54
4.3.4	Water structure - canonical Monte Carlo simulations	59
4.4	Conclusions	70
5	Lattice Discretization Effects on the Critical Parameters of Model Non-polar and Polar Fluids¹	72
5.1	Introduction	72
5.2	Simulation methods	73
5.3	Results and discussion	75
5.3.1	Non-polar model	75
5.3.2	Polar model	82
5.3.3	Non-polar + polar model	87
5.4	Conclusions	87
6	Determination of Second Virial Coefficients by Grand Canonical Monte Carlo Simulations¹	91
6.1	Introduction	91

6.2	Methods	93
6.3	Results and discussion	95
6.4	Conclusions	101
7	Theory of Fine-lattice Discretization for Near Critical Fluids	102
7.1	Introduction	102
7.2	Theoretical background	104
7.3	The one-dimensional models	106
7.3.1	Hard-core model	106
7.3.2	New approach for choosing the lattice spacing in hard-core model	109
7.3.3	Square-well model	112
7.3.4	New approach for choosing the lattice spacing in square-well model	113
7.3.5	Logarithmic hard-core model	116
7.3.6	Logarithmic hard-core model with a jump	121
7.3.7	Cubic model	127
7.4	Higher-dimensional models	132
7.4.1	Lattice discretization theory	136
7.4.2	Approximation of the error	137
8	Summary and Suggestions for Future Work	144
	Bibliography	150

LIST OF TABLES

3.1	Torsional potential parameters for the new model, taken from Jorgensen <i>et al.</i> [1] and the model used by Errington and Panagiotopoulos, EP model.	28
3.2	Potential parameters and critical properties for diatomic models. . .	31
4.1	Potential parameters for nitrogen, carbon dioxide, and water.	43
4.2	Structural parameters for nitrogen, carbon dioxide, and water.	45
4.3	Critical temperature and critical density of the carbon dioxide models studied. The data lie with a level of confidence of approximately 68 percent.	49
4.4	Estimates of critical temperature with different lattice discretization parameter, ζ , for the water model studied.	54
4.5	Critical temperature and critical density as a function of system size for the water models studied.	58
4.6	Geometric properties of various discretized water models compared with the continuum model ($\zeta = \infty$).	61
5.1	Critical parameters for the “Exp-6 monomer” model.	77
5.2	Critical parameters for the “Exp-6 dimer” model.	78

5.3	Structural parameters for the dumbbell models. “NC” is the number of configurations with bond length between 1σ and 1.2σ on the lattice with discretization parameter ζ . “DM” and “CH” are the average molecular dipole moment (for the “fixed charge model”) and average electrostatic charge (for the “fixed dipole model”), respectively.	83
5.4	Critical parameters for the “dumbbell” and “trimer” models, with identical dipole and quadrupole moments.	86
6.1	Reduced second virial coefficient, calculated analytically and by simulation for both “LJ” and “Exp-6” models with $L^* = 5$	97

LIST OF FIGURES

2.1	Matching of the scaled order parameter distribution to the universal curve for the Ising three-dimensional universality class, indicated by the continuous line. Points are from the present simulations for the nitrogen model in Chapter 3.	13
2.2	Schematic illustration of the lattice discretization process for $\zeta = 1, 2, 3,$ and 5 . A two-dimensional hard-core model is shown for simplicity, even though all calculations were performed for three-dimensional systems. The full circle represents the particle diameter whereas the dashed line circle shows the excluded points for other equal-sized particles.	16
2.3	Phase diagram of the discretized restricted primitive model (RPM) from reference [2]. Points are for $\zeta = 3$ (triangles), 4 (stars), 5 (squares), and the continuum-space RPM (solid line).	17
2.4	Phase diagram for the Lennard-Jones (LJ) lattice models from reference [3]. Points are for $\zeta = 1$ (crosses), 2 (x's), 3 (diamonds), 5 (squares), 10 (circles), and continuum-space LJ model (solid line).	18
2.5	Potential energy, $U(r)$, vs. distance, r , for the following models: $\alpha = 12$ (solid line), $\alpha = 14$ (dashed line), and $\alpha = 16$ (dotted line).	21

3.1	Phase behavior of the n -butane model from histogram reweighting GCMC simulations. Errington and Panagiotopoulos model [4] (open circles), new model (open triangles), and experimental data [5] (solid line and filled circle).	29
3.2	Percent deviation from experiment for the vapor pressure for n -butane from histogram reweighting GCMC simulations. The open circle symbols represent the EP model and the cross symbols represent the new model.	30
3.3	Phase behavior of the diatomic model, N_2 , from histogram reweighting GCMC simulations. $\alpha = 12$ (open squares), $\alpha = 14$ (open stars), $\alpha = 16$ (open triangles), and experimental data [6] (solid line). . . .	32
3.4	Phase behavior of the nitrogen model from histogram reweighting GCMC. New model (open stars) and experimental data [6] (solid line).	33
3.5	Vapor pressure of the nitrogen model. Symbols are the same as in Fig. 3.4.	34
3.6	Critical temperatures, T_c , as a function of $L^{-(\theta+1)/\nu}$, with $\theta = 0.52$ and $\nu = 0.63$ [7] for nitrogen model.	34
3.7	Phase behavior of the fluorine model from histogram reweighting GCMC simulations. New model (open stars) and experimental data [6] (solid line).	35
3.8	Vapor pressure for the fluorine model. Symbols are the same as in Fig. 3.7.	36

4.1	Phase behavior of the nitrogen model from histogram reweighting GCMC simulations: N_2 model with $\zeta = 12$ (open stars), off-lattice data (open circles), and experimental data [6] (filled triangles). . . .	46
4.2	Phase behavior of the carbon dioxide model from histogram reweighting GCMC simulations. $(EP)_{CO_2}$ model with $\zeta = 8$ and $L^* = 7$ (open stars), off-lattice data (open circles), and experimental data [6] (filled diamonds).	48
4.3	Phase behavior of the carbon dioxide model from histogram reweighting GCMC simulations. $(EP)_{CO_2}$ model with $\zeta = 12$ and $L^* = 7$ (open stars), $(EP)_{CO_2}$ model with $\zeta = 20$ and $L^* = 7$ (open circles), off-lattice data (open squares), and experimental data [6] (filled diamonds).	49
4.4	Phase behavior of the carbon dioxide model from histogram reweighting GCMC simulations. Harris model with $\zeta = 8$ and $L^* = 7$ (open stars), off-lattice data (open squares), and experimental data [6] (filled circles).	50
4.5	Matching of the scaled order parameter distribution to the universal curve for the Ising three-dimensional universality class, indicated by the continuous line. Points are from our simulations for the $(EP)_{CO_2}$ model with $\zeta = 8$ and $L^* = 7$	51
4.6	Phase behavior of the carbon dioxide model from histogram reweighting GCMC simulations: $(EP)_{CO_2}$ model with $\zeta = 8$ and $L^* = 10$ (open stars), off-lattice data (open circles), and experimental data [6] (filled diamonds).	52

4.7	Matching of the scaled order parameter distribution to the universal curve for the Ising three-dimensional universality class, indicated by the continuous line. Points are from our simulations for the (EP) _{CO₂} model with $\zeta = 8$ and $L^* = 10$	53
4.8	Phase behavior of the water model from histogram reweighting GCMC simulations. (EP) _{H₂O} model with $\zeta = 32$ and $L^* = 5.4$ (open stars), off-lattice data (open triangles), and experimental data [6] (filled circles).	55
4.9	Matching of the scaled order parameter distribution (as obtained by the method indicated in Sec. 2.4) to the universal curve for the Ising three-dimensional universality class: see the continuous line. Points are from our simulations for the (EP) _{H₂O} model with $\zeta = 32$ and $L^* = 5.4$	56
4.10	Matching of the scaled order parameter distribution to the universal curve for the Ising three-dimensional universality class, indicated by the continuous line. Points are from our simulations for the (EP) _{H₂O} model with $\zeta = 32$ and $L^* = 6.7$	57
4.11	Phase behavior of the water model from histogram reweighting GCMC simulations. (EP) _{H₂O} model with $\zeta = 32$ and $L^* = 6.7$ (open stars), off-lattice data (open triangles), and experimental data [6] (filled circles).	58
4.12	Density profile of discretized models of SPC/E water at $T = 400$ K. The curves from bottom to top are for $\zeta = 10, 11, 12, 20, 21, 22, 30,$ and ∞	62

4.13	Oxygen-oxygen radial distribution functions of discretized models of SPC/E water at $T = 400$ K. The curves are the same as Fig. 4.12.	63
4.14	Oxygen-hydrogen radial distribution functions of discretized models of SPC/E water at $T = 400$ K. The curves are the same as Fig. 4.12.	64
4.15	Hydrogen-hydrogen radial distribution functions of discretized models of SPC/E water at $T = 400$ K. The curves are the same as Fig. 4.12.	65
4.16	Snapshot of a configuration of SPC/E water at $T = 400$ K. with $\zeta = 11$.	66
4.17	Density profile of discretized models of SPC/E water at $T = 550$ K. The curves from bottom to top are for $\zeta = 10, 11, 12, 20, 21, 22, 30,$ and ∞ .	67
4.18	Oxygen-oxygen radial distribution functions of discretized models of SPC/E water at $T = 550$ K. The curves are the same as Fig. 4.17.	67
4.19	Oxygen-hydrogen radial distribution functions of discretized models of SPC/E water at $T = 550$ K. The curves are the same as Fig. 4.17.	68
4.20	Hydrogen-hydrogen radial distribution functions of discretized models of SPC/E water at $T = 550$ K. The curves are the same as Fig. 4.17.	68
4.21	Density profile of discretized models of SPC/E water at $T = 640$ K. The curves are the same as Fig. 4.17.	69
4.22	Oxygen-oxygen radial distribution functions of discretized models of SPC/E water at $T = 640$ K. The curves are the same as Fig. 4.17.	69
5.1	Matching of the scaled order parameter distribution to the universal curve for the Ising three-dimensional universality class, indicated by the continuous line for the dumbbell model with $\zeta = 10$. Open circles: $L^* = 12$ and open triangles: $L^* = 15$.	74

5.2	Reduced critical temperature, T_c^* , as a function of $1/\zeta^6$ for the “Exp-6 monomer” model with $L^* = 7$ (filled squares), $L^* = 10$ (filled stars), and $L^* = 12$ (filled circles). The dashed line shows the power-law least squares fitting to the data.	79
5.3	Reduced critical temperature, T_c^* , as a function of $1/\zeta^7$ for the “Exp-6 dimer” model with $L^* = 7$ (filled squares), $L^* = 10$ (filled stars), and $L^* = 12$ (filled circles). The dashed line shows the power-law least squares fitting to the data.	80
5.4	Reduced critical temperature, T_c^* , as a function of $(L^*)^{-(\theta+1)/\nu}$ with $\zeta = 10$, for the “Exp-6 monomer” model.	81
5.5	Reduced critical temperature, T_c^* , as a function of $(L^*)^{-(\theta+1)/\nu}$ with $\zeta = 10$, for the “Exp-6 dimer” model.	81
5.6	Schematic illustration of two polar models considered in this work. (a) The “dumbbell” model; (b) the “trimer” model.	82
5.7	Reduced critical temperature, T_c^* , as a function of $1/\zeta^2$ for the “dumbbell” model with $L^* = 12$, same charge (filled triangles), same dipole (open triangles) and with $L^* = 15$, same charge (filled circles), same dipole (open circles). The dashed line shows the power-law least squares fitting to the data.	84
5.8	Reduced critical temperature, T_c^* , as a function of $1/\zeta^9$ for the “Polar+Exp-6” model with $L^* = 7$ (filled squares), $L^* = 10$ (filled stars), and $L^* = 12$ (filled circles). The dashed line shows the power-law least squares fitting to the data.	88

6.1	Second virial coefficient for ethane, B_2 , as a function of temperature, T . The stars represent calculations for the “ethane” model using GCMC with $L^* = 5$ and circles represent the experimental data [8].	99
6.2	Second virial coefficient for propane, B_2 , as a function of temperature, T . The stars represent calculations for the “propane” model using GCMC with $L^* = 5$ and circles represent the experimental data [8].	100
7.1	Reduced critical density as a function of $1/n$ for HC Model.	108
7.2	Reduced critical temperature as a function of $1/n$ for HC Model. . .	108
7.3	The insensitivity of the discretized potential function to the value of δ	110
7.4	Reduced critical density as a function of $1/n$ for SW Model.	113
7.5	Reduced critical temperature as a function of $1/n$ for SW Model. .	114
7.6	Optimization factor δ as a function of $1/n$ for SW model.	115
7.7	Boltzmann factor with different values of $\beta\epsilon$	117
7.8	Reduced critical density as a function of $1/n^2$ for LGHC model with no temperature effect.	118
7.9	Reduced critical temperature as a function of $1/n^2$ for LGHC model with no temperature effect.	119
7.10	Reduced critical density as a function of $1/n^2$ for LGHC model with some temperature effect.	120
7.11	Reduced critical temperature as a function of $1/n^2$ for LGHC model with some temperature effect.	120

7.12	Different logarithmic potential models with $y_0 = 0.0$ (stars), $y_0 = 0.25$ (crosses), $y_0 = 0.5$ (open squares), $y_0 = 0.75$ (open diamonds), and $y_0 = 2.0$ (open circles).	121
7.13	Reduced critical density as a function of $1/n$ for LGHCj Model with no temperature effect with $y_0 = 0.25$ (open stars), $y_0 = 0.5$ (open circles) and $y_0 = 0.75$ (right triangles).	122
7.14	Reduced critical temperature as a function of $1/n$ for LGHCj model with no temperature effect. Symbols are the same as Figure 7.13.	123
7.15	Reduced critical density as a function of $1/n$ for LGHCj model with some temperature effect. Symbols are the same as Figure 7.13.	123
7.16	Reduced critical temperature as a function of $1/n$ for LGHCj model with some temperature effect. Symbols are the same as Figure 7.13.	124
7.17	Reduced critical temperature as a function of $1/n$ for LGHCj model with $y_0 = 2.0$ and no temperature effect considered.	124
7.18	Reduced critical density as a function of $1/n$ for LGHCj model with $y_0 = 2.0$ and no temperature effect considered.	125
7.19	Reduced critical temperature as a function of $1/n$ for LGHCj model with $y_0 = 2.0$ when some temperature effect is considered.	125
7.20	Reduced critical density as a function of $1/n$ for LGHCj model with $y_0 = 2.0$ when some temperature effect is considered.	126
7.21	Boltzmann factor, $\exp[-\beta\varphi(r)]$, vs. distance, r , for cubic model.	127
7.22	Reduced critical density as a function of $1/n^4$ for cubic model with no temperature effect.	128
7.23	Reduced critical temperature as a function of $1/n^4$ for cubic model with no temperature effect.	129

7.24	Reduced critical density as a function of $1/n^4$ for cubic model with some temperature effect.	130
7.25	Reduced critical temperature as a function of $1/n^4$ for cubic model with some temperature effect.	131
7.26	Reduced critical density obtained with both analytical (full stars) and VdW approximation method (open circles) for a one-dimensional system.	133
7.27	Reduced critical temperature obtained with both analytical (full stars) and VdW approximation method (open circles) for a one-dimensional system.	134
7.28	Reduced critical density obtained via VdW approximation method in $d = 3$	135
7.29	Reduced critical temperature obtained via VdW approximation method in $d = 3$	135
7.30	$N(\zeta) - V(\zeta)$ for different values of ζ in $d = 3$	137
7.31	RMS versus ζ for $d = 3$	139
7.32	RMS being smooth with 3 points versus ζ for $d = 3$	139
7.33	RMS being smooth with 5 points versus ζ for $d = 3$	140
7.34	The plots from top to bottom are for $\zeta = 1-10000, 1000-10000, 2000-10000, 4000 - 10000, \dots$, and $8000 - 10000$ for $d = 3$, respectively.	140
7.35	The fractional error for $d = 2$ versus $1/\zeta^{3/2}$	141
7.36	The fractional error for $d = 3$ versus $1/\zeta^2$	141
7.37	Second virial coefficient for the hard-core model with integer (stars) and real (open squares) values of ζ	143
7.38	Second virial coefficient for the LJ model at $T_c^* = 1.299$	143

8.1 Density profile of water models at $T = 400$ K with $\zeta = 11$: Buckingham Exp-6 model (dashed-dotted line), SPC/E model (dotted line), and continuum model (solid line). 148

Chapter 1

Introduction and Outline

The design of processes in chemical industry, such as distillation, adsorption, and liquid-liquid extraction, requires quantitative estimates of the thermodynamic properties of the participating substances and of their mixtures. Understanding the phase equilibria and thermodynamic properties of model fluids, real fluids, and solids is of great interest for developing efficient chemical processes. In principle, thermodynamic properties can be obtained directly from quantum and statistical mechanics, but this is a very difficult numerical problem and has not been achieved accurately for molecules more complicated than H_2 . Laboratory facilities are limited to a finite range of temperature and pressure in generating the thermodynamic properties and obtaining experimental data of good quality is an expensive proposition. Molecular simulations can in principle yield predictions outside the range of experimental investigation. It was not long ago that deriving phase equilibria even for very simple systems by simulations was an ordeal. Phase equilibria were obtained by formulation of the equation of state from simulations at various state points [9]. The introduction of the Gibbs Ensemble technique simplified the calculation of the coexisting properties of the fluids with a single simulation [10–12]. A

limitation of the Gibbs ensemble method is that finite-size effects near the critical point are often difficult to characterize and control, due to the variable extent of the two simulation regions [11, 13–16]. By contrast, for grand canonical Monte Carlo simulations, such effects are well understood and easily controlled [17, 18]. In addition, the grand canonical ensemble appears to have an increased statistical efficiency compared to Gibbs ensemble Monte Carlo [19] for identical systems and conditions. More recently, histogram reweighting grand canonical Monte Carlo simulations [20, 21] along with mixed-field finite-size scaling concepts have been used for obtaining the critical parameters and phase behavior properties with a good degree of accuracy [18, 22, 23]. In histogram reweighting, the frequencies of observing a particular number of particles and specified energy density are collected, which data can in turn be extended to different chemical potentials and temperatures [24, 25], and the thermodynamic properties of the system can be obtained by rescaling of the parameters using basic statistical mechanics. All these methodological advances have significantly simplified the use of molecular simulations for getting the desired phase equilibria for real fluids.

The research reported in this thesis has focused on investigations of thermodynamic properties of fluids at a molecular level by using intermolecular potential models and statistical mechanical theories. Using advanced methods and powerful computers, the behavior of materials on a microscopic level has been studied and based on these studies one can predict macroscopic properties of the specified systems. Grand canonical histogram reweighting Monte Carlo calculations have been performed to obtain thermodynamic properties, mainly liquid-vapor coexistence data. Critical parameters are determined from mixed-field finite-size scaling methods.

The lack of appropriate intermolecular potential functions is still one of the main problems in using atomistic simulation methodologies in practice. Most currently available intermolecular potentials are not optimized for important properties such as phase coexistence, vapor pressure, and critical behavior, over a broad range of temperatures and densities. The models are limited to a finite range of temperatures close to ambient conditions. So the objective of the work in Chapter 3 is to improve the mathematical models that describe the intermolecular potentials for a variety of systems far from ambient temperature and pressure.

Monte Carlo simulations involving polar systems, either ions or partial charges, are especially time-consuming when applying periodic boundary conditions, requiring the use of Ewald [26, 27] summation or a similar technique. This can result in intractably long computation times for systems of even modest size. Lattice models have been used extensively in polymer physics (e.g., the bond fluctuation model [28, 29]), protein [30–32], thin film simulations [33] and for studies of phase transitions and critical phenomena [34–42]. The greatest advantage of these models is computational efficiency with respect to time and length scales. Through the study of larger systems, finite-size effects near critical points that result from the divergence of the correlation length can be greatly diminished. It has been shown that lattice simulations can effectively capture the phase behavior of both the restricted primitive model (RPM) electrolyte [2] and Lennard-Jones monomeric fluids [3] on fine enough lattices with considerably less computational effort than in continuum-space calculations. The degree of discretization is of utmost importance: a coarsely discretized lattice simulation will be computationally faster to run, but may not be physically meaningful, while fine discretization will capture continuum behavior better, but may not provide significant time savings. For a

simulation to be useful in modelling, its results must be nearly indistinguishable from similar simulations performed in the continuum-space. This work, reported in this thesis, aims to develop a methodology to enable the investigation of a variety of fluids and their mixtures which are currently too difficult to simulate directly in continuum-space. The concept of finely discretized lattices is applied to a variety of real fluids in Chapter 4, where the phase behavior and critical points of the various discretized models and whether they capture qualitatively their continuum counterparts is also investigated. In Chapter 5, the effect of lattice discretization is studied extensively for a different number of non-polar and polar model fluids. In Chapter 6, we address the direct determination of second virial coefficients using grand canonical Monte Carlo simulations. Chapter 7 is devoted to a theoretical investigation of fine-lattice discretization theory for near critical fluids. In the final chapter the main results of the thesis are briefly summarized and possible directions for further research are discussed.

Chapter 2

Simulation Methodologies

2.1 Introduction

In experimental studies of phase equilibria, although the phase behavior is known for the conditions under which the experiments were performed, the data by themselves do not allow an engineer to predict phase coexistence properties for different conditions. Since chemical engineers typically have to design processes for a wide range of temperatures, pressures, and mixture compositions, the use of experiments to determine the phase coexistence properties of fluids and their mixtures can quickly become impractical. Because of the limited amount of experimental data available and the cost in both time and money of collecting new data, a large effort has gone into the development of equation of state models. The main shortcoming of equation of state models is that their predictive powers are generally limited to the temperatures and pressures for which the model was fitted to experimental data. Use of the model at other conditions may result in predictions that are seriously in error. An alternative to equation of state models is to use molecular simulation techniques for the prediction of phase equilibrium for

fluids and their mixtures. The first computer simulations of thermodynamic properties of fluids were performed at Los Alamos [43] and served as the basis of the modern Monte Carlo methodology. In order to be able to calculate accurate phase coexistence properties from simulation, the free energy as a function of density is needed; this was the motivation behind the development of “umbrella sampling” techniques [44–46]. The calculation of phase coexistence from molecular simulation was greatly simplified by the technique of Gibbs ensemble Monte Carlo [10–12]. The Gibbs ensemble Monte Carlo methodology provides a direct and efficient route to the phase coexistence properties of fluids, for calculations of moderate accuracy [47]. Grand canonical Monte Carlo simulations, when combined with histogram reweighting [20, 21], have the potential for higher accuracy, especially when equilibria at a large number of state points are to be determined [47]. When combined with finite-size scaling technique, grand canonical histogram reweighting Monte Carlo simulations can be used to obtain reliable estimates of critical parameters directly from simulations. In Section 2.2 the molecular simulation methods are explained briefly. In Sections 2.3 and 2.4 histogram reweighting grand canonical Monte Carlo and mixed-field finite-size scaling concepts are reviewed, respectively. Section 2.5 deals with the fine-lattice discretization method which is based on the discretization methodology introduced by Panagiotopoulos and Kumar [2]. The last section of this chapter describes applications of different intermolecular potential models and the recent developed potentials for thermodynamic properties, mainly phase coexistence applications.

2.2 Molecular simulation methods

Molecular simulation generates information at the microscopic level (atomic and molecular positions and/or velocities) and the conversion of this very detailed information into macroscopic terms (pressure, internal energy, etc.) is the subject of statistical mechanics. The two best known computer simulation methods are Monte Carlo (MC) and molecular dynamics (MD). The name “Monte Carlo” was chosen because of the use of random numbers in the calculation. Monte Carlo is a stochastic process in which points in phase space are sampled with a frequency proportional to their Boltzmann weight. The properties are then determined by averaging over the regions sampled. An implementation of the Metropolis [48] scheme is as follows. A number of particles is confined in a box or cell and one particle with energy $U(r^N)$ is chosen at random. A random displacement is given to the particle as $r' = r + \Delta$, the new energy $U(r'^N)$ is calculated, and then the move will be accepted with probability [49]:

$$\text{acceptance } (old \rightarrow new) = \min \left(1, \exp \left[-\beta [U(r'^N) - U(r^N)] \right] \right), \quad (2.1)$$

where “*old*” represents the initial and “*new*” the new configuration. If rejected, the old configuration is kept. This process is repeated until the system loses its memory of the initial condition and reaches a steady state (with properties fluctuating around a mean value with no long-term drift), presumed to be the equilibrium state. Properties are then measured over a sufficiently large number of samples to obtain a desired statistical accuracy.

Molecular dynamics simulation is a technique to compute the equilibrium and transport properties of a classical many-body system. Molecular dynamics is a deterministic method in which the motion of molecules is determined by the forces acting between the particles. The forces are calculated and Newton’s second law is

integrated with a sufficiently small time step to determine the new positions of the particles. This computation is done for all the molecules so their trajectories can be followed in space and time. After equilibration as for Monte Carlo, the properties are measured. The results are expected to be the same from both techniques for ergodic systems. The MD method is generally more expensive, but can be used for getting time-dependent, non-equilibrium, and transport properties [50, 51].

2.3 Grand canonical histogram reweighting Monte Carlo

Grand canonical Monte Carlo simulations are performed in a simulation box with volume V . Monte Carlo simulation aims to provide information about the properties of a macroscopic sample. Since the number of degrees of freedom that can be handled in simulations vary between a few hundred up to a few thousand, it is very important to choose boundary conditions that mimic a bulk system, surrounding the sample. Accordingly, periodic boundary conditions are enforced with a minimum image convention [51] that limits the number of interactions that need to be taken into account. The input parameters to the simulation are temperature, T , and chemical potential, μ . Three types of movements are performed during the simulations. The particles are displaced, created, and annihilated using the standard acceptance criteria [50, 51]. Displacements of particles are accepted with the following rule:

$$\text{acceptance}_{\text{displace}}(old \rightarrow new) = \min \left(1, \exp\{-\beta[U(r'^N) - U(r^N)]\} \right). \quad (2.2)$$

Particles are added and annihilated with acceptance ratios:

$$\begin{aligned} \text{acceptance}_{\text{add}} (old \rightarrow new) = & \quad (2.3) \\ \min \left(1, \frac{V}{\Lambda^3(N+1)} \exp\{\beta[\mu - U(N+1) + U(N)]\} \right) \end{aligned}$$

and

$$\begin{aligned} \text{acceptance}_{\text{delete}} (old \rightarrow new) = & \quad (2.4) \\ \min \left(1, \frac{\Lambda^3 N}{V} \exp\{-\beta[\mu + U(N-1) - U(N)]\} \right), \end{aligned}$$

where “*old*” represents the initial configuration of the space and “*new*” the configuration after the move has been done, while r^N represents the spatial configuration and $\Lambda = \sqrt{h^2/2\pi mk_B T}$ is the thermal de Broglie wavelength. It is necessary to have a reasonable percentage of accepted moves of each type in order to obtain good statistics. The probability of observing N particles with their corresponding energies, E , is collected in a histogram. The probability function follows the relationship:

$$f_1(N, E) = \frac{\Omega(N, V, E) \exp(-\beta_1 E + \beta_1 \mu_1 N)}{\Xi(\beta_1, V, \mu_1)}, \quad (2.5)$$

where $\Omega(N, V, E)$ is the microcanonical partition function (density of states) and $\Xi(\beta_1, V, \mu_1)$ is the grand canonical partition function, while β is the reciprocal temperature ($= 1/k_B T$, where k_B is Boltzmann’s constant). Neither Ω nor Ξ is known, but Ξ is a constant for the given input parameters. Since $f_1(N, E)$ can be measured during the simulation, the density of states and its corresponding thermodynamic function can be determined. The entropy can be evaluated by a simple transformation of the above equation as:

$$S(N, V, E) = \ln \Omega(N, V, E) \quad (2.6)$$

$$= \ln f_1(N, E) + \beta_1 E - \beta_1 \mu_1 N + C, \quad (2.7)$$

where C is a run-specific constant equal to the logarithm of the grand partition function for the chemical potential and temperature of the run, $\ln \Xi(\beta_1, V, \mu_1)$. For a new simulation with a different temperature, T_2 , and chemical potential, μ_2 , one would expect a new distribution, $f_2(N, E)$, with:

$$\frac{f_2(N, E)}{f_1(N, E)} \propto \exp[(\beta_2\mu_2 - \beta_1\mu_1)N - (\beta_2 - \beta_1)E]. \quad (2.8)$$

The above relationship applies when the collected histograms have some overlaps with each other. After different histograms have been obtained, they have to be combined to one histogram. Ferrenberg and Swendsen have developed a technique [20, 21] which ensures the minimum deviation between predicted and observed histograms. The distribution $P_{\mu, \beta}(N, E)$ for a given number of particles and energy that results from combining R runs assuming that they all have the same statistical efficiency is:

$$P_{\mu, \beta}(N, E) = \frac{\sum f_n(N, E) \exp(\beta\mu N - \beta E)}{\sum K_m \exp(\beta_m\mu_m N - \beta_m E - C_m)}, \quad (2.9)$$

where K_m is the total number of observation for run m . The constants C_m are obtained using an iterative relationship:

$$\exp(C_m) = \sum_N \sum_E P_{\mu_n, \beta_n}(N, E). \quad (2.10)$$

Given an initial guess for the weight, the two equations can be iterated until convergence is achieved. Once this has been achieved all thermodynamic properties of the system such as mean configurational energy and mean density can be obtained by computing

$$\langle U \rangle_{\mu, \beta} = \sum_N \sum_E P(N, E; \mu, \beta) E \quad (2.11)$$

and

$$\langle \rho \rangle_{\mu, \beta} = \frac{1}{V} \sum_N \sum_E NP(N, E; \mu, \beta) N. \quad (2.12)$$

The pressure of the system is related to the area under the three-dimensional probability distribution by:

$$\begin{aligned}\beta PV &= \ln(\mu, V, \beta) + \text{constant} \\ &= \ln \sum_N \sum_E \Omega(N, V, E) \exp[-\beta E + \beta \mu N] + \text{constant}.\end{aligned}\quad (2.13)$$

The area under the probability distribution gives a reliable estimate of the partition function, which is required to determine the additive constant in Eq. 2.13. To determine this constant, the partition function is calculated at low densities. A plot of $\ln \Xi$ vs. N gives a straight line of unit slope, which verifies that the system behaves as an ideal gas at these conditions. It is then possible to extrapolate $\ln \Xi$ to the $N = 0$ limit, with the y intercept representing the additive constant.

2.4 Mixed-field finite-size scaling

Recent advances in the determination of critical parameters for fluids lacking special symmetries have been based on the concept of mixed-field finite-size scaling and have been reviewed in detail by Wilding and Bruce [18, 22]. Near the critical point the correlation length of fluctuations exceeds the microscopic length scale. In the standard approach, critical points are estimated using mixed-field finite-size scaling analysis under the assumption of Ising-type criticality. An (unnormalized) order parameter $x = (\delta N - s\delta E)$ is first constructed from the number of particles, N , and energy, E , where $\delta N = N - N_c$, $\delta E = E - E_c$, and s is a field-mixing parameter. The probability distribution of this order parameter, $P_L(x)$, is obtained by histogram reweighting of the raw simulation data. The ordering parameter is then normalized to zero mean and unit variance. The resulting distributions are compared to the Ising-class limiting critical point distribution. The method is ap-

plied to different systems of interest using a code developed in our group, where the temperature, chemical potential, and field mixing parameter are optimized using a downhill simplex optimization method in order to obtain the critical temperature, the critical chemical potential, the critical density, and the field mixing parameter, s , so as to minimize the sum of the absolute deviations between the observed and Ising-class limiting distribution. A typically successful example of the matching of some data (obtained below) to the universal curve is shown in Fig. 2.1; on the other hand, for some of our data (e.g., shown in Fig. 4.9) the matching between the Ising universal distribution and our data is not so satisfactory. Generally, it seems that too small a system size is the main reason for the relatively poor matching. However, statistical noise can be another reason for not having a good match between our data and the universal curve, especially when the computational cost to reduce the degree of the statistical noise is prohibitively high with the existing methods and the available CPU capacity.

Further evidence of Ising criticality can be found when corrections to scaling of the critical temperature and critical density are analyzed through the scaling relations

$$\rho_c^*(L^*) - \rho_c^*(\infty) \propto L^{*-(1-\alpha)/\nu} \quad (2.14)$$

and

$$T_c^*(L^*) - T_c^*(\infty) \propto L^{*-(\theta+1)/\nu}, \quad (2.15)$$

where $\rho_c^*(L^*)$ and $T_c^*(L^*)$ are the apparent size-dependent dimensionless critical density and critical temperature obtained by finite-size scaling analysis, and $\rho_c^*(\infty)$, $T_c^*(\infty)$ are the infinite system values. The exponents in Eqs. 2.14 and 2.15 for the three-dimensional Ising universality are $(\alpha, \nu) \approx (0.109, 0.630)$ and $(\theta, \nu) \approx (0.52, 0.630)$ [7].

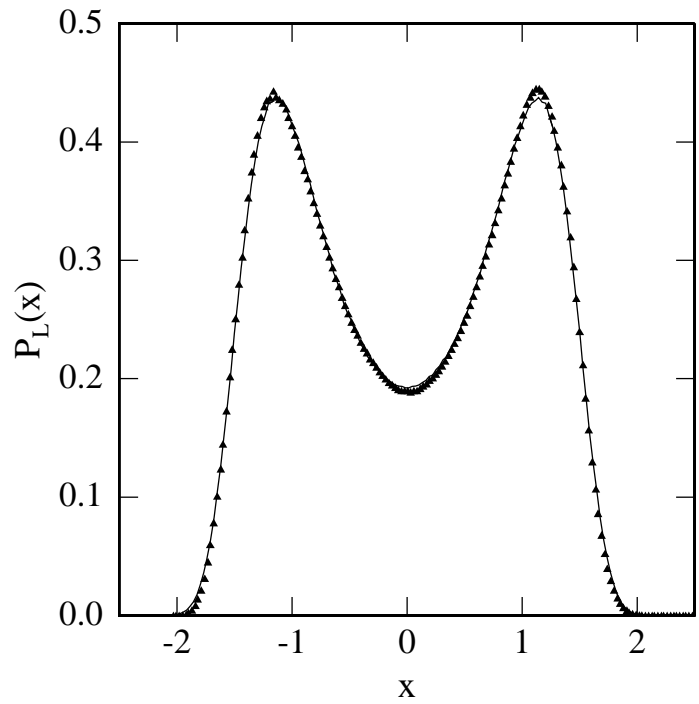


Figure 2.1: Matching of the scaled order parameter distribution to the universal curve for the Ising three-dimensional universality class, indicated by the continuous line. Points are from the present simulations for the nitrogen model in Chapter 3.

Scaling theory has been a powerful tool for gaining insight into critical phenomena [37–42]. Experimentally, a scaling equation of state has been confirmed for many fluids [52–55]. The asymptotic scaling of fluid criticality requires two scaling fields, namely a thermal field, \tilde{t} , and an ordering field, \tilde{h} , that in leading order, are both linear combinations of the bare fields, $t \propto T - T_c$ and $h \propto \mu - \mu_c$ [56]. Bruce and Wilding considered only the mixing of t and h into the relevant scaling \tilde{h} and \tilde{t} [57, 58]. On the basis of these assumptions, however, the second derivative of the chemical potential along the phase boundary turns out to remain finite at the critical temperature, and, hence, this approach is inadequate to account for a Yang-Yang anomaly [59]. Yang and Yang proved that the divergence of the constant-volume specific heat at a gas-liquid critical point implies that either the second derivative of the pressure or the second derivative of the chemical potential or both diverge when temperature approaches the critical temperature along the phase boundary. The necessity of allowing for pressure casts doubt on the validity of recently devised finite-size algorithms for extrapolating the effective coexistence curves obtained in precise modern simulations of continuum fluid models. Fisher and Orkoulas [60] have argued that in order to describe the Yang-Yang anomaly, the pressure deviation, $P - P_c$, must mix into the scaling fields, especially into ordering field \tilde{h} , and they have presented strong evidence that the second derivative of the chemical potential on the vapor pressure curve diverges like the specific constant-volume heat when temperature approaches the gas-liquid critical point from below, for both propane and carbon dioxide [60]. The anomalies in e.g., argon and helium, might well be significantly smaller, where this idea is supported by simulations of the hard-core square-well fluid [61]. However, we have not considered any pressure mixing for the calculation of critical points using the mixed-field

finite size technique [56].

2.5 Fine-lattice discretization method

The key idea underlying this method is illustrated schematically in Fig. 2.2. Consider a pure fluid of N single-site particles of characteristic diameter σ , interacting with any intermolecular potential, $U(r^N)$, where r^N denotes the positions of the N particles. The potential may or may not have hard-core interactions and could be non-pairwise-additive. One can construct a series of lattice models in which allowable positions for the centers of particles are on a grid of characteristic spacing λ . While any lattice type could be considered in principle, we use the simple cubic lattice as the basis for all calculations. The lattice discretization parameter, defined as the ratio of the particle diameter to the lattice spacing, $\zeta = \sigma/\lambda$, controls how closely the lattice model approaches the continuum behavior. For low ζ values, the underlying lattice could have a strong effect on the thermodynamic and structural properties of the system. Previous work has established that for particles interacting via hard-core plus Coulombic potential (RPM electrolyte [62, 63]), a value of $\zeta = 5$ [2], and for particles interacting via Lennard-Jones potential [64, 65], a value of $\zeta = 10$ [3], are already sufficiently high so that the systems have qualitatively and almost quantitatively the same phase behavior as the continuum analogs. The phase behavior of both systems is shown in Figs 2.3 and 2.4, respectively, where T and ρ are the dimensionless temperature and density.

The potential energy of interaction between any two sites on the lattice is

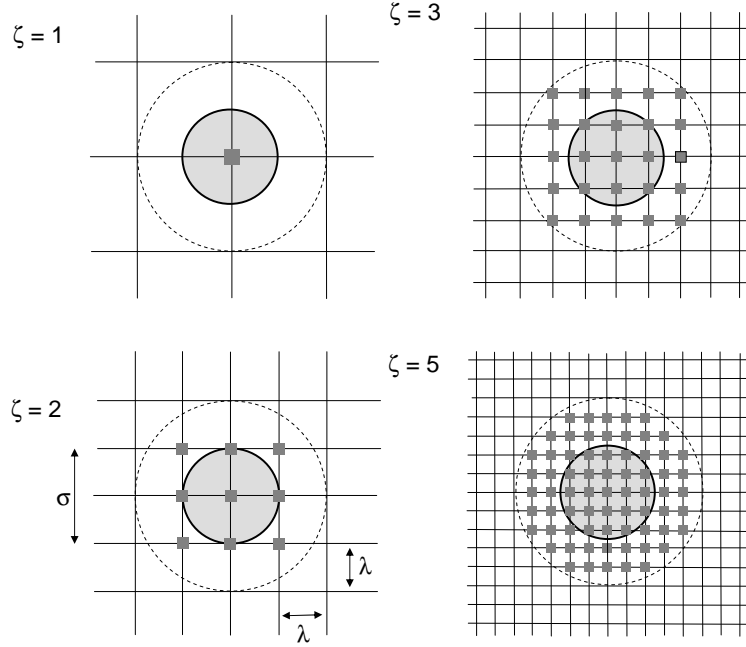


Figure 2.2: Schematic illustration of the lattice discretization process for $\zeta = 1, 2, 3,$ and 5 . A two-dimensional hard-core model is shown for simplicity, even though all calculations were performed for three-dimensional systems. The full circle represents the particle diameter whereas the dashed line circle shows the excluded points for other equal-sized particles.

translationally invariant. The energy of interaction can be written as:

$$U(r_{ij}) = U(|x_i - x_j|, |y_i - y_j|, |z_i - z_j|), \quad (2.16)$$

where $x, y,$ and z are integers between 0 and $L \times \zeta - 1$. $L \times \zeta$ must be an integer, even though L and ζ can take any real value individually, in order to allow periodic boundary conditions on the simple cubic lattice. Eq. 2.16 suggests that the potential of interaction can be calculated once at the beginning of a simulation and stored in an array of length $(L \times \zeta)^3$. It is been shown for particles interacting via

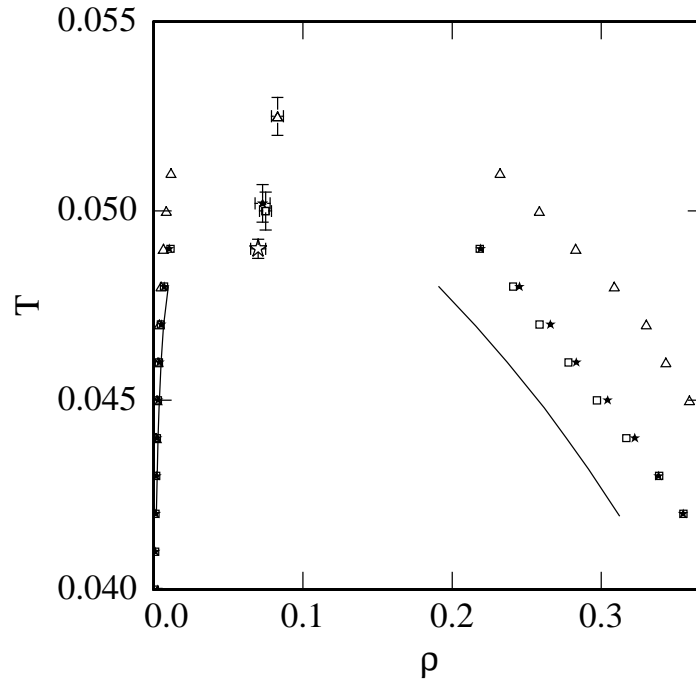


Figure 2.3: Phase diagram of the discretized restricted primitive model (RPM) from reference [2]. Points are for $\zeta = 3$ (triangles), 4 (stars), 5 (squares), and the continuum-space RPM (solid line).

the Lennard-Jones potential and via Coulombic plus hard-core potentials, that this method is more efficient by a factor between 10-20 and 100 [2, 3, 66], respectively, relative to calculations in continuum-space. The speedup ratio may be sensitive to coding details, machine architecture, and compilation parameters.

2.6 Intermolecular potentials

Here, we give an overview of the main contributions to forces between molecules. They can be separated into two main types: “long-range” and “short-range”. The

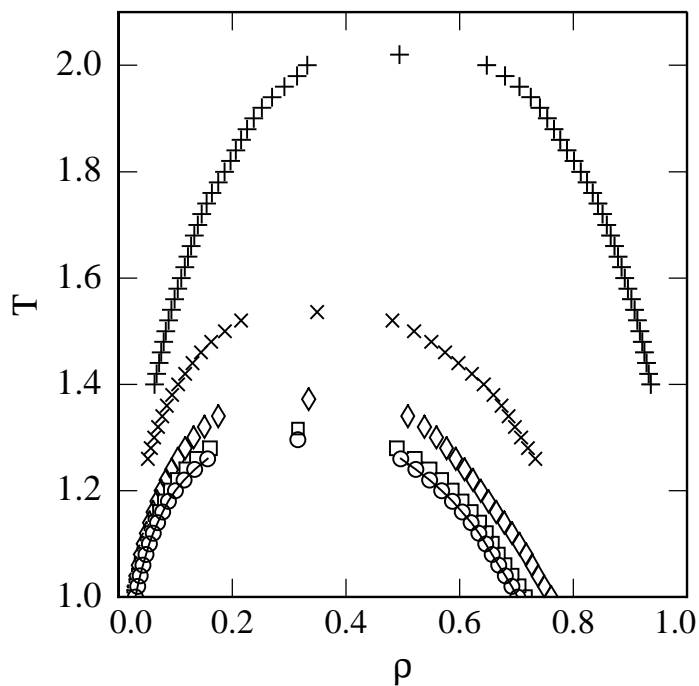


Figure 2.4: Phase diagram for the Lennard-Jones (LJ) lattice models from reference [3]. Points are for $\zeta = 1$ (crosses), 2 (x's), 3 (diamonds), 5 (squares), 10 (circles), and continuum-space LJ model (solid line).

long-range effects are of three kinds: electrostatic, induction and dispersion. The electrostatic effects arise from the straightforward classical interactions between the static charge distributions of the two molecules. They are strictly pairwise additive and may be either attractive or repulsive. Induction effects arise from the distortion of a particular molecule in the electric field of all the neighbors, and are always attractive and they are strongly non-additive. Dispersion arises because the charge distributions of the molecules are constantly fluctuating as the electrons move quantum mechanically. The motions of the electrons in the two molecules become correlated, in such a way that lower energy configurations are favored and

higher energy ones disfavored. The average effect is a lowering of the energy, and since the correlation effect becomes stronger as the molecules approach each other, the result is an attraction. Further contributions to the energy arise at short range, that is, at distances where the molecular wavefunctions overlap significantly. The most important of these are exchange and repulsion [67].

The simplest intermolecular potential used to describe the repulsion forces between molecules is the hard sphere potential. This potential has one parameter, the sphere diameter σ . If the molecules are within one diameter of each other their interaction energy is infinite, otherwise it is zero. This potential has no attractive part, but does simulate the steep repulsive part of realistic potentials [62]. An extended model of the hard sphere model that includes an attractive term and yet is simple enough to handle analytically is the square well potential. The pair potential between two particles, separated by a distance r , $U(r)$, is infinite for distances less than σ , $-\epsilon$ for distances between σ and $\lambda\sigma$, and equal to zero for r greater than $\lambda\sigma$. While these potentials are useful as points of reference, they are not appropriate for real fluids. The most well known analytical expression with adjustable parameters for $U(r)$ is [62]

$$U(r) = \frac{n\epsilon}{n-6} \left(\frac{n}{6}\right)^{6/(n-6)} \left[\left(\frac{\sigma}{r}\right)^n - \left(\frac{\sigma}{r}\right)^6 \right], \quad (2.17)$$

where σ is the distance at which $U(r) = 0$, and ϵ is the depth of the well. The exponent n is usually taken to be an integer between 9 and 15. For $n = 12$, $U(r)$ is the well known Lennard-Jones 6-12 potential (abbreviated as “LJ” from this point on) [64, 65]:

$$U_{LJ}(r) = 4\epsilon \left[\left(\frac{\sigma}{r}\right)^{12} - \left(\frac{\sigma}{r}\right)^6 \right]. \quad (2.18)$$

The modified Buckingham exponential-6 potential [68] (abbreviated as “Exp-6” from this point on) is a four parameter model of the form:

$$U_{Exp-6}(r) = \begin{cases} \epsilon \left[\frac{6}{\alpha - 6} \exp \left(-\alpha \left[\frac{r}{r_m} - 1 \right] \right) - \frac{\alpha}{\alpha - 6} \left(\frac{r_m}{r} \right)^6 \right] & \text{if } r \geq r_{max} \\ +\infty & \text{if } r < r_{max} \end{cases} \quad (2.19)$$

where ϵ , r_m , and α are model parameters. The parameter r_m denotes the radial distance at which the potential has a minimum. The cutoff distance r_{max} is the smallest positive value for which $dU(r)/dr = 0$ and may be obtained iteratively from Eq. 2.19. The reason a cutoff distance is required is that at very short distances, the original Exp-6 potential becomes negative. While canonical ensemble Monte Carlo or molecular dynamics simulations never sample this unphysical “attractive” region, this is not the case on trial insertions in grand canonical simulations. The characteristic size parameter, σ , for this potential is defined by that value of r for which $U(r) = 0$ and is obtained numerically; likewise ϵ is the well depth of the potential. Fig. 2.5 illustrates the change of shape of the potential function as the repulsion exponent is increased from $\alpha = 12$ to 14, and 16. It has been shown that the greater flexibility of the Buckingham potential increased the accuracy with which one can predict the phase coexistence curve and vapor pressure of a simple fluid such as methane from a united atom model [25]. The accuracy attained is higher in comparison with the Lennard-Jones potential, although at the cost of introducing one extra parameter in the potential model.

The inverse-square Coulomb force between two charged atoms, or ions, is the strongest of the physical forces, stronger even than chemical binding forces. The energy for the Coulombic interaction between two charges Q_1 and Q_2 is given by:

$$U(r) = \frac{Q_1 Q_2}{4\pi\epsilon\epsilon_0 r}, \quad (2.20)$$

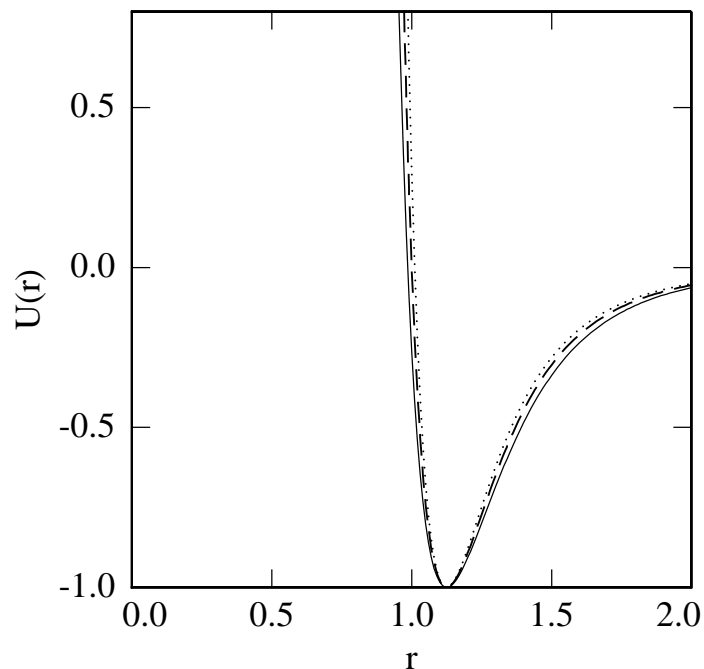


Figure 2.5: Potential energy, $U(r)$, vs. distance, r , for the following models: $\alpha = 12$ (solid line), $\alpha = 14$ (dashed line), and $\alpha = 16$ (dotted line).

where ϵ is the relative permittivity or dielectric constant of the medium, ϵ_0 is the permittivity of vacuum, and r the distance between the two charges. Expressions for dipoles and quadrupoles are more complicated [69]. All the potentials mentioned above are two-body potentials which only count the forces between two particles in the absence of any other particle. Three- and higher-body interactions count the interactions between two particles in the presence of a third body. Considering this effect makes the potentials very complex and computationally expensive. So in practice most of the potentials considered, only represent the forces between two bodies; this is known as the “pairwise additivity” approximation [50, 62].

Chapter 3

Phase Equilibria of Diatomic Molecules and *N*-alkanes

3.1 Introduction

3.1.1 Diatomic molecules

Computer simulations have contributed significantly to the understanding of the properties of diatomic molecules. The objectives of such calculations are twofold. On one hand, they allow us to explore potential models which are sufficiently simple to be related to statistical mechanical theories, or to serve as prototypes for anisotropic systems. On the other hand, the simulations of real systems, and eventually the diatomic potentials can serve as a reference system for future studies.

One of the simplest anisotropic pair potentials is two spherical centers with a fixed separation between them known as Lennard-Jones centers at a fixed distance potential (2LJC). Ooi and Oobatake numerically estimated the parameters

of Lennard-Jones parameters between atoms (hydrogen, oxygen, and nitrogen) from second virial coefficients [70]. Barojas *et al.* [71], Cheung and Powles [72] studied the 2LJ potential with a reduced bond length value of $l^* \equiv l/\sigma = 0.329$, corresponding to nitrogen, which predicts the thermodynamic and structural properties of liquid nitrogen satisfactorily. Sweet and Steele [73] calculated the second virial coefficients for the Lennard-Jones potential and found that the experimental results for nitrogen could be fitted just for a reduced range of 0 to 0.4. These results illustrate the difficulty of obtaining an intermolecular potential from the second virial coefficient. Singer *et al.* presented the thermodynamic properties for $l^* = 0.505 - 0.793$, and attempted to model liquid F_2 , Cl_2 , and Br_2 [74, 75]. Powles and Gubbins measured the second virial coefficients of liquid nitrogen and oxygen using the LJ potential so that they fit the experimental data [76]. After that diatomic molecules simulated by 2LJC potential have been the subject of extensive MD calculations by Barojas *et al.* [71] and Kriebel *et al.* [77]. Generally good agreement between the experimental and simulation data was obtained in all studies for thermophysical and thermodynamical properties, except for the critical properties. Gallassi and Tildesley studied the phase behavior of Lennard-Jones diatomics as a function of the bond-length [78]. Their potential for chlorine did an excellent job even in producing the liquid-vapor coexistence curve and even in reproducing the experimental critical points to within a few percent.

3.1.2 *N*-alkanes

Hydrocarbon molecules are important for both (petro-)chemical and biological applications. The simplest hydrocarbons are the *n*-alkanes, which are linear chains

of methylene groups with a methyl group at both ends. A good starting point for development of intermolecular potential models for the phase behavior of real fluids is thus *n*-alkanes. Two different approaches for dividing *n*-alkanes into interaction sites are usually followed when building a molecular force field. The first approach is to treat each hydrogen and carbon atom as an interaction site. The second approach is to unite each carbon and its bonded hydrogen into a single interaction site known as a methyl or methylene group. An alternative to the united atom model is the more realistic all-atom representation. With this model, interaction sites are placed at all carbon and hydrogen centers, which increases the number of interaction sites by a factor of three and the computational demand by an order of magnitude.

Two recently proposed models, TraPPE [79, 80] and NERD [81, 82], use a united-atom, Lennard-Jones potential to describe the non-bonded interactions. The TraPPE force field overestimates the vapor pressures, with the deviation from experiment greatest at low reduced temperatures. The NERD model exhibits similar behavior for longer chains, with the results being closer to experimental value than the TraPPE model. In general, the new model of Errington and Panagiotopoulos produces the vapor pressure to a higher level of accuracy and the agreement is best for shorter chain lengths [4]. The model slightly overestimates the critical pressures and underestimates the vapor pressure at low reduced temperatures for longer chains. The critical parameters are in good agreement with experimental results. The Exp-6 model reproduces the experimental saturated liquid and vapor densities and vapor pressures for ethane through octane to within average absolute deviations of a few percent and critical parameters are also found to be in good agreement with experiment.

In this chapter, new models are developed for diatomic molecules including nitrogen, chlorine, and fluorine, that give good descriptions of the phase behavior and vapor pressure over a large temperature range. The performance of the models developed in this work has been evaluated to determine the phase behavior and critical parameters of the same systems by the use of the discretization methodology.

3.2 Models and simulation details

The objective is to come up with parameters for the non-bonded interactions that fit the experimental data of the specific systems under development. We have used the Exp-6 intermolecular potential in order to enable comparisons with previous studies in [4]. Truncation of the potential has an important effect on the phase behavior and the critical properties. In the present study, we are interested in obtaining the properties of the full potential and long-range corrections are applied in every simulation. Corrections are performed with the method of Theodorou and Suter [83]. In this approach, all interactions between molecules and their minimum image neighbors are included and the long-range correction is calculated by integrating the potential in two parts. The first part is from $L/2$ to $\sqrt{3}/2L$ using the corrected radial distribution function given by Eq. 13 in Ref. [83]. The second part is calculated by assuming $g(r) = 1$ and integrating from $\sqrt{3}/2L$ to ∞ . The bonded interactions are described by stretching, bending, and torsional potentials which are obtained by fitting to *ab initio* data. We use the data available for the bonded interactions as our initial guess.

As our simulation methodology, a series of grand canonical simulations is computed in the vicinity of the coexistence curve in continuum-space. The sequence

of runs starts with collecting a histogram near critical conditions. These runs at critical conditions cover a broad range of particles and energies and can be used as bridges between the liquid and gas states. Histogram reweighting is then used to get the coexistence properties over a limited range of temperatures. To increase the temperature range, some additional runs are done at lower temperatures. The second run is completed at a temperature of $T = T_c - \Delta T$ and at chemical potentials of $\mu = \mu_c \pm \Delta\mu$. Both $\Delta T(\text{K})$ and $\Delta\mu(k_B T/N)$ are chosen such that good overlaps between histograms are obtained. The three histograms are then combined by the method of Ferrenberg and Swendsen [20, 21] and again the coexistence density and activity are determined. The process is repeated for temperatures of $T = T_c - 2\Delta T$, $T = T_c - 3\Delta T$, and $T = T_c - 4\Delta T$ until the whole temperature range is covered. The critical properties are obtained using the mixed-field finite-size scaling method.

The model parameters, in our study, ϵ , σ , and α have to be chosen so such that the final thermodynamic properties fit the experimental data. The initial values for ϵ and σ are chosen from literature values and rescaled using the principle of corresponding states to match the critical temperature and density of the corresponding real system. The α value varies between 12 and 22, so in our study, we examine all possible choices and choose the best value that fits the experimental data. The other input parameters that have to be imposed on the system are the parameters that determine the structural form of the fluid to be studied. The bond length, bond bending angle, and torsional parameters potential are known as the structural properties of molecules, which should be all defined when creating the model molecules. For each of the molecules studied, the volume of the simulation box is selected so that the critical density of the given system corresponds to

approximately 80 particles. Statistical uncertainties are estimated by performing three duplicate sets of runs at identical conditions with different seeds for the random number generator. The “ran2” routine [84] which has a period of 2.3×10^{18} and no low-order serial correlations, is used. A random initial configuration is used for vapor phase simulations, while liquid phase simulations are started from the final configuration of a previous run. Most of the simulations are equilibrated for 1 million Monte Carlo steps (MCS). Vapor phase simulations are run for 5 million MCS, while simulations in the liquid phase run for 10 (MCS) or more. We use Pentium III 733 MHz computers to run our simulations and usually the runs take a few hours to complete.

3.3 Results and discussion

3.3.1 *N*-butane

The potential model developed for *n*-butane by Errington and Panagiotopoulos [4] (abbreviated as EP model from this point on), reproduces the experimental saturated liquid, vapor densities, and vapor pressure to within average absolute deviations of few percent. The critical temperature and critical density were also found to be in good agreement with experiment. The torsional parameters used for the EP model were taken from Smit *et al.* [85], where the torsional parameters for the TraPPE [79, 80] and NERD [81, 82] models are twice their counterparts in [85] and they are taken from [1]. Here, we use the EP model but with the torsional values used for the TraPPE and NERD models and we refer to this model as the “new” model. We need to emphasize that the only difference between the new and the EP models is that the torsional parameters used for the new model, which were

Table 3.1: Torsional potential parameters for the new model, taken from Jorgensen *et al.* [1] and the model used by Errington and Panagiotopoulos, EP model.

Model	EP	New
V_0	0	0
V_1	355.03	710.06
V_2	-68.19	-136.38
V_3	791.32	1582.64

also used for the TraPPE and NERD models, are twice those of the EP model. As mentioned in the previous section, for creating the n -butane chain like the other n -alkanes, the bond length, bond bending angles, and torsional angles of the specific system should be specified for the system. The CH3-CH3, CH3-CH2, and CH2-CH2 bond lengths are set to 1.839, 1.687 and 1.535Å, respectively [4]. The bond angles for the new model are generated according to the bending potential:

$$U_{\text{bend}}(\theta) = \frac{K_\theta}{2}(\theta - \theta_{\text{eq}})^2, \quad (3.1)$$

with $K_\theta = 62500 \text{ K/rad}^2$, $\theta_{\text{eq}} = 114^\circ$, and the torsion angle is defined by the potential:

$$U_{\text{tor}}(\phi) = V_0 + \frac{V_1}{2}(1 + \cos(\phi)) + \frac{V_2}{2}(1 + \cos(2\phi)) + \frac{V_3}{2}(1 + \cos(3\phi)), \quad (3.2)$$

with torsional parameters set as in Table 3.1.

The phase coexistence is shown in Fig. 3.1 for both the new model and the EP model, respectively. The excellent agreement of the phase coexistence behaviors for the two n -butane models indicates that the dependence of this property on torsional parameters is very weak. This point is further emphasized in Fig. 3.2,

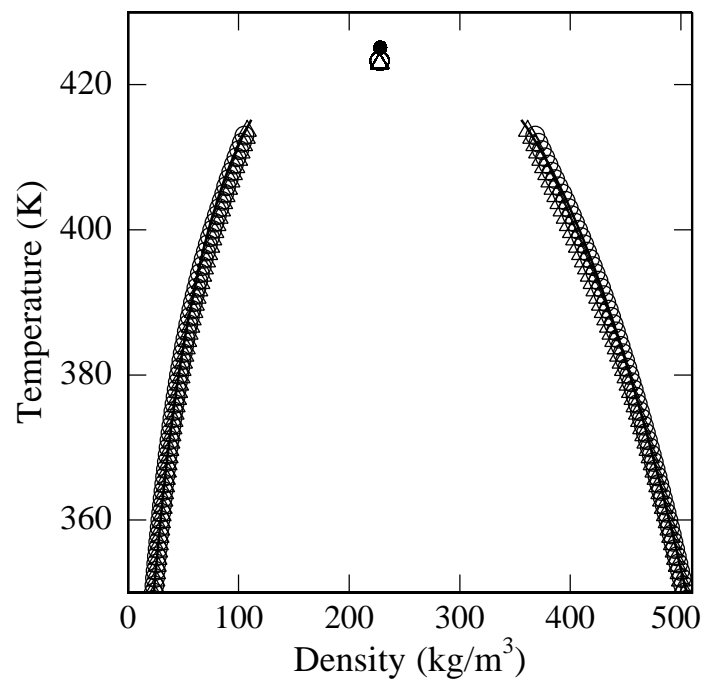


Figure 3.1: Phase behavior of the *n*-butane model from histogram reweighting GCMC simulations. Errington and Panagiotopoulos model [4] (open circles), new model (open triangles), and experimental data [5] (solid line and filled circle).

where the percent deviation of the new and EP models from experimental values are plotted as a function of temperature for the vapor pressure. Over the temperature range selected, the new model does not deviate by more than a few percent for the vapor pressure.

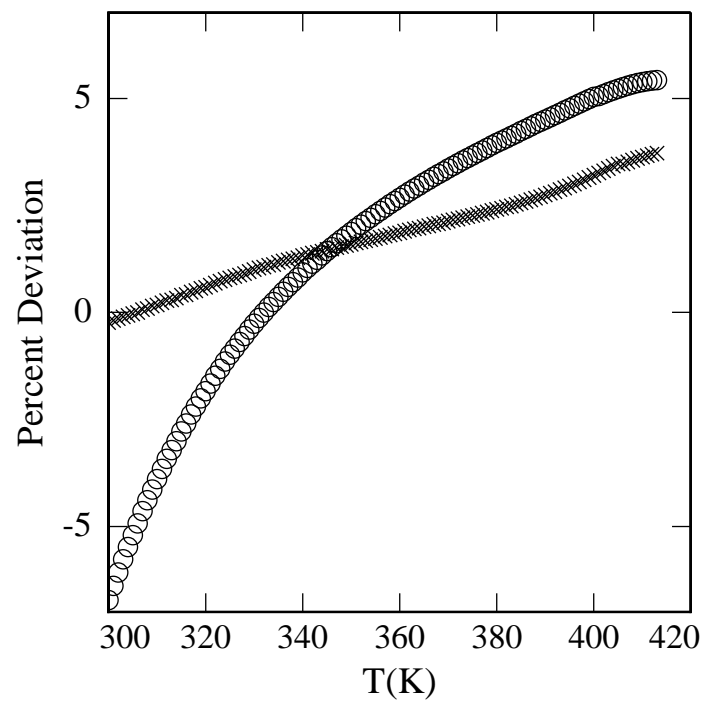


Figure 3.2: Percent deviation from experiment for the vapor pressure for *n*-butane from histogram reweighting GCMC simulations. The open circle symbols represent the EP model and the cross symbols represent the new model.

Table 3.2: Potential parameters and critical properties for diatomic models.

Molecule	$\epsilon/k_B(\text{K})$	$\sigma(\text{\AA})$	α	$\ell^* = \ell/\sigma$	$T_c(\text{K})$	$\rho_c(\text{kg/m}^3)$	$P_c(\text{MPa})$
N ₂	37.3	3.310	14	0.33	126.15±0.05	316.9±0.9	3.4±0.7
F ₂	54.85	2.825	14	0.51	143.84±0.04	578.7±0.8	5.2±0.6
Cl ₂	184.95	3.357	14	0.63	416.67±0.05	591.5±0.9	8.1±0.6

3.3.2 Diatomic molecules

The main task of this part of our work is to obtain good models for diatomic molecules such as N₂, O₂, F₂, and Cl₂. We started with N₂. During the fitting process the bond length was kept fixed. The three parameters of the Exp-6 group were adjusted to obtain an optimum description of phase coexistence, vapor pressure, and critical parameters. The values for the two $\epsilon/k_B = 37.3$ K and $\sigma = 3.310\text{\AA}$ input parameters were obtained from the literature [4], as was the bond length ($l = 1.085\text{\AA}$) between two atoms. Three different models with α values 12, 14, 16, and a reduced bond length value of $\ell^* = l/\sigma = 0.33$ were examined. As is shown in Fig. 3.3, $\alpha = 14$ seems to be a good starting point for the α value. The model parameters for nitrogen, fluorine, and chlorine models are listed in Table 3.2.

Coexistence densities of the nitrogen model predicted by the new model are compared to experimental values in Fig. 3.4. The experimental coexisting densities and pressures are obtained from NIST - Chemistry WebBook [6]. The uncertainties of the simulated points are less than the symbol size. Overall, there is a good agreement between the saturated liquids and gas densities of the new model and experimental data over the temperature range. The vapor pressure of the new

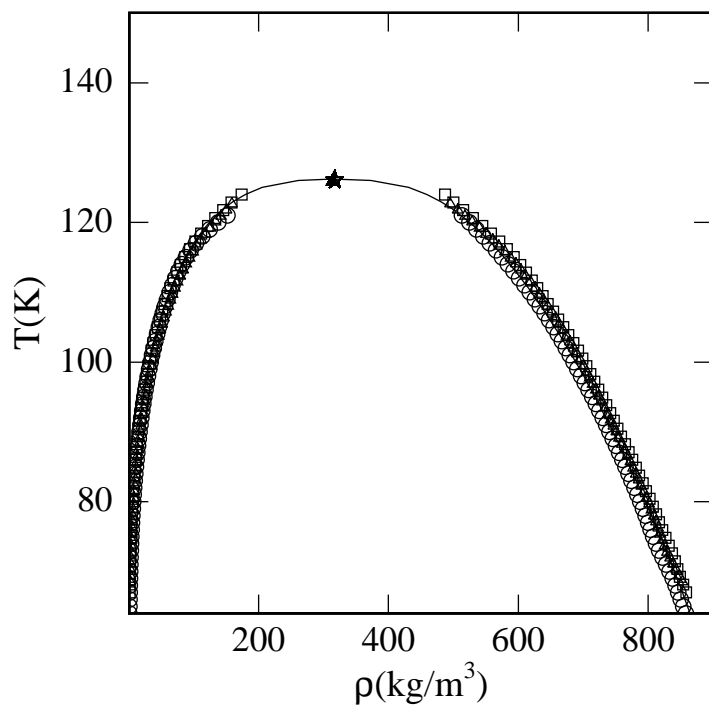


Figure 3.3: Phase behavior of the diatomic model, N_2 , from histogram reweighting GCMC simulations. $\alpha = 12$ (open squares), $\alpha = 14$ (open stars), $\alpha = 16$ (open triangles), and experimental data [6] (solid line).

model is presented in Fig. 3.5. Again, the agreement between the experimental data and the model is good. There is a big deviation at lower temperatures due to high density at low temperature where the liquid needs a large amount of CPU time to get equilibrated with reasonable acceptance ratios for both displacement and addition/deletion movements. Our CPU capacity did not allow us to have good histograms for the high density region. The critical parameters of the models studied are presented in Table 3.2. The vapor pressure was fitted to the equation:

$$\ln P^{sat} = a_o + \frac{a_1}{T}, \quad (3.3)$$

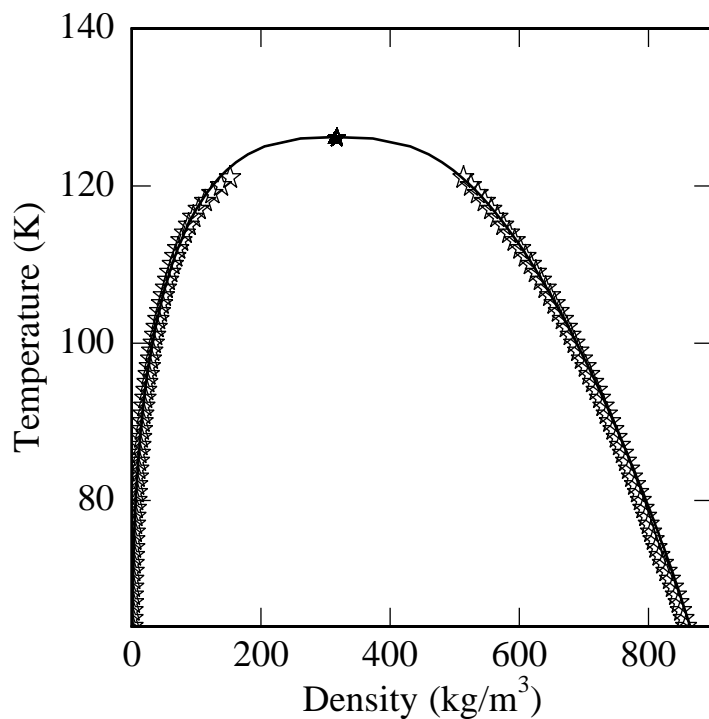


Figure 3.4: Phase behavior of the nitrogen model from histogram reweighting GCMC. New model (open stars) and experimental data [6] (solid line).

and the critical pressure was calculated by extrapolating the vapor pressure curve to the critical temperature. In order to see the effect of volume on the critical parameters, two other system sizes were also used for the nitrogen model. Grand canonical simulations were completed with volumes twice and half of the original volume. In Fig. 3.6, we plot the critical temperature, as a function of $L^{(-\theta+1)/\nu}$, where L is the length of the simulation box, with $\theta = 0.52$ and $\nu = 0.630$ [7]. Size effects are pronounced near the critical condition and we do not see any difference away from the critical point. Phase diagram and vapor pressure curves for F_2 are shown in Figs. 3.7 and 3.8 as part of our work.

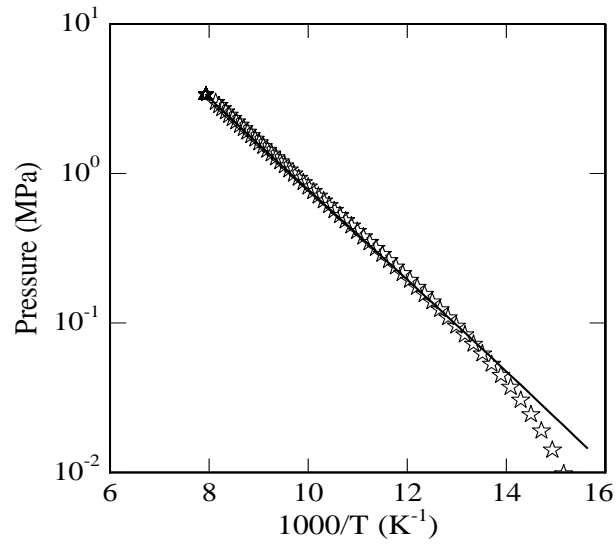


Figure 3.5: Vapor pressure of the nitrogen model. Symbols are the same as in Fig. 3.4.

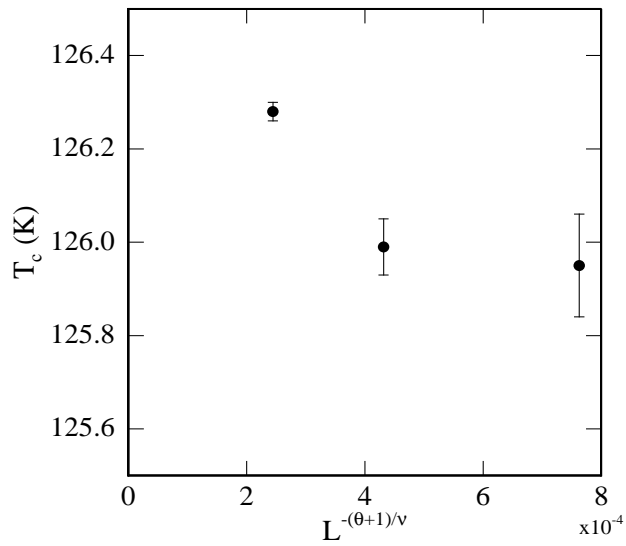


Figure 3.6: Critical temperatures, T_c , as a function of $L^{-(\theta+1)/\nu}$, with $\theta = 0.52$ and $\nu = 0.63$ [7] for nitrogen model.

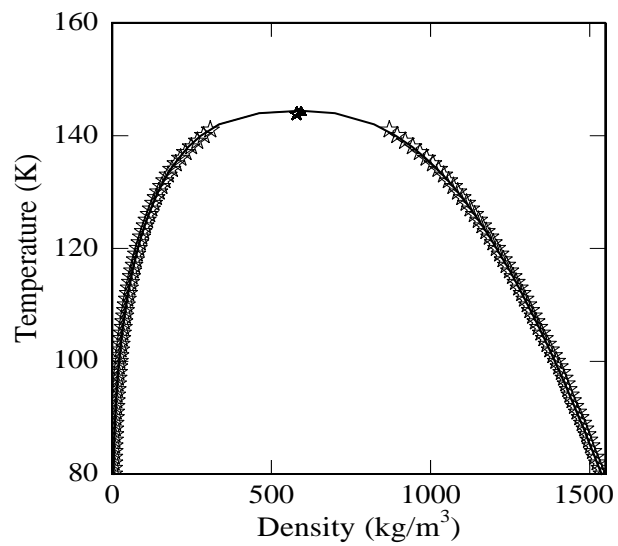


Figure 3.7: Phase behavior of the fluorine model from histogram reweighting GCMC simulations. New model (open stars) and experimental data [6] (solid line).

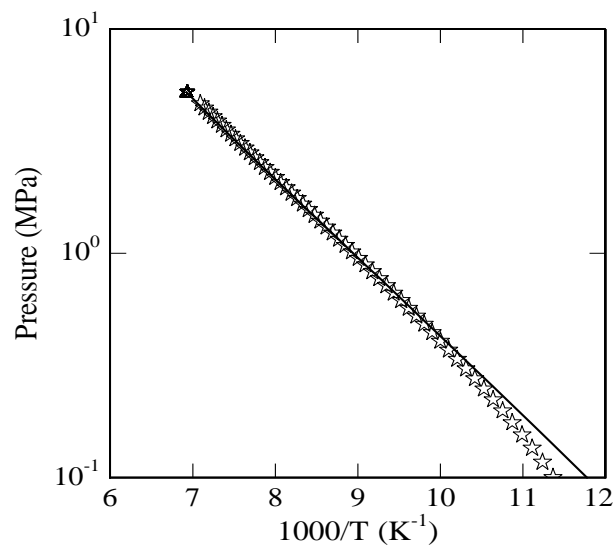


Figure 3.8: Vapor pressure for the fluorine model. Symbols are the same as in Fig. 3.7.

3.4 Conclusions

In this chapter new intermolecular potential models for diatomic molecules, mainly nitrogen, chlorine, and fluorine have been developed and parameterized to the vapor-liquid coexistence properties far from ambient temperature and pressure. The models utilize the Buckingham exponential-6 potential to describe the non-bonded repulsive/dispersion interactions. Histogram reweighting grand canonical Monte Carlo methods were used to obtain the model parameters. The new models reproduce the experimental saturated liquid and vapor densities, vapor pressure and critical parameters. All the phase coexistence properties are calculated using simulations in continuum-space. The models obtained in this work for the diatomic real fluids can be used in next the chapter as a starting point for calculating the thermodynamic properties of real fluids, but in lattice space using the fine-lattice discretization methodology which will be explained in detail.

Chapter 4

Phase Equilibria of Real Non-polar and Polar Fluids

4.1 Polar fluids, carbon dioxide and water

No molecules carry net charges, but many possess an electric dipole. Such molecules are called polar molecules. The dipoles of some molecules depend on their environment, and can change substantially when they are transferred from one medium to another, especially when molecules become ionized in a solvent. Water is a dipolar molecule [69]. Because of the importance of water in many disciplines of science, and in technological applications, and its importance for biological processes, the development of empirical intermolecular potentials for water has received much attention. This information is crucial for a variety of traditional and novel chemical engineering applications where water is used at extreme conditions, including its critical and supercritical regions both as a pure liquid and in aqueous solutions [86]. Fixed-point charge models of water are commonly used because of their simplicity and their successful description of the structure of liquid

water near ambient conditions. In all of these models it is assumed that the water molecules interact through a Lennard-Jones potential between the oxygens, and through Coulombic potentials between one negative charge located at the oxygen and two positive charges located at the hydrogens. Models of this type include the Bernal-Fowler [87], ST2 [88], TIPS2 [89], TIP4P [90], SPC [91], SPC/E [92], and MSOC/E [93]. Because most of these potentials were optimized to describe the liquid phase of water at ambient conditions, the models are inadequate at high temperatures and most predict a critical temperature lower than the experimental value. The new fixed-point charge potential model of Errington and Panagiotopoulos [94, 95] using the Buckingham Exponential-6 group at the oxygen center and a set of three point charges, improves the description of water over current fixed-point charge models. The new model reproduces the critical temperature to within 0.2%, the critical density to within 8%, and saturated liquid densities to within an average of 2.5%. Vapor pressures are also in good agreement with experiment, and the model second virial coefficient is in better agreement with experiment than other fixed-point charge models. The negative-positive and positive-positive radial distribution functions are in better agreement with experiment than current models, but the new model does not describe correctly the second shell of the negative-negative radial distribution function. It is well known that water has a relatively large molecular polarizability and, thus, interactions which are not pair-additive are expected to be important in any model potential that would describe a large variety of water data. An alternative is the fluctuating charge model in which the point charges on atomic sites are allowed to fluctuate in response to the water environment [96, 97]. Another alternative, a polarizable model describing both the static and dynamic properties of water over a wide range of densities and temper-

atures, was the topic of several studies over the past years [98–102]. None of the advanced simulation studies of four dipole-polarizable and two fluctuating-charge water force fields have demonstrated a satisfactory description of the vapor-liquid coexistence curve from room temperature to the critical region. Recent work of Chen *et al.* [103, 104] uses an improved polarizable force field by accounting an additional coupling between the Lennard-Jones interaction parameters for a pair of oxygen sites and their partial charged (electronic configuration). Although, Chen *et al.* recommend their polarizable SPC model for phase equilibrium calculations at elevated temperatures (above 400 K), their investigation did not result in a simple polarizable force field that works satisfactorily from the triple point to the boiling point of water.

Carbon dioxide is another example of a polar fluid. Carbon dioxide has a substantial quadrupole moment. The molecule is also highly polarizable, with the effective electrostatic moments varying with temperature and density. There have been several previous studies aimed at developing potential models for this fluid. A common approach is to use point charges to model the polar interactions. This type of approach has many attractive features. The model is simple and relatively straightforward to simulate. The computational demand of such a model is comparatively low. The drawback of this model is its inability to capture multi-body effects. The electrostatic moment of the molecule is fixed and therefore cannot fluctuate in response to the local environment. As a result, the effects of polarizability must implicitly be taken into account via the point charges. To account for this, the dipole moment of many point charge models is set significantly higher than the bare pure-fluid properties can be achieved. Harris and Yung have proposed [105] a point charge model for carbon dioxide. A point charge was placed on each atomic

center to emulate the quadrupole moment. The magnitude of the point charges was selected to reproduce the experimental quadrupole moment. The model accurately reproduces the saturated densities and vapor pressures.

In this work, Monte Carlo simulations of real polar molecules on a discretized lattice, where each atom overlaps multiple lattice sites, have been investigated to provide comparable results with off-lattice simulations in one-tenth the computation time. We have investigated the models studied by Errington and Panagiotopoulos in [95] and in [106] for off-lattice water and carbon dioxide, respectively. A discretization of $\zeta = 10$ is required in atomic systems such as LJ and Exp-6 atoms, in order to reproduce the continuum counterparts, whereas for molecular systems, the finer discretization level ($\zeta = 12$) is required to capture the features of intermolecular bonding such as bond lengths and bond angles [107]. Thus provided one uses a value of $\zeta > 12$ one can have an estimate of the errors induced by fine lattice discretization method. For a lattice simulation to be useful in modeling, its results should be nearly indistinguishable from similar simulations performed in the continuum-space. This work aims to develop a methodology to enable the investigation of real systems simulated in lattice space but reasonably comparable with off-lattice simulations. Using this technique, the fine lattice discretization method can be expand to more complex polar models and also their mixtures with less computational expense. A significant barrier for simulating these systems is the computational time required to evaluate the potential energy, whereas here, as described in detail in Section 2.5, a lattice interaction matrix can be evaluated once at the start and be used repeatedly during the simulation to save significant CPU time.

4.2 Model development and methods

Each of the models used in this chapter incorporates a united -atom description of the molecules. The non-polar pairwise additive intermolecular interactions were described by Lennard-Jones (LJ) or Buckingham exponential-6 (Exp-6) potentials. For nitrogen, interaction sites were placed at the nitrogen centers, and for carbon dioxide interaction sites were placed at the carbon and oxygen centers. A single site was placed at the oxygen center for water. The Lorentz-Berthelot combining rules for σ and ϵ were used for the interactions between unlike molecules [108]. The geometric mean combining rule was used for the parameter α in the potential model.

$$\sigma_{ij} = (\sigma_{ii} + \sigma_{jj})/2, \quad (4.1)$$

$$\epsilon_{ij} = \sqrt{\epsilon_{ii}\epsilon_{jj}}, \quad (4.2)$$

and

$$\alpha_{ij} = \sqrt{\alpha_{ii}\alpha_{jj}}. \quad (4.3)$$

The polar interactions were modeled with point charges. The charges were placed at the carbon and oxygen centers for carbon dioxide and three point charges were used for water, one at the oxygen center and two at “pseudo hydrogen” sites. A “pseudo hydrogen” is defined as an interaction site at which a point charge is placed without a corresponding LJ or Exp-6 group. This combination leads to the following expression for the energy of interaction between two molecules

$$U = \sum_i \sum_{i < j} u_{ij}^{np} + \sum_{\gamma=1}^3 \sum_{\delta=1}^3 \frac{1}{4\pi\epsilon_o} \frac{q_\gamma q_\delta}{r_{\gamma\delta}}, \quad (4.4)$$

the first term of Eq. 4.4 describes the non-polar energy, where u_{ij}^{np} is either the Lennard-Jones (LJ) or exponential-6 potential (Exp-6). The second term accounts

Table 4.1: Potential parameters for nitrogen, carbon dioxide, and water.

Molecule	Type	Group	Model	$\epsilon/k_B(\text{K})$	$\sigma(\text{\AA})$	α	q(e)
nitrogen	Exp-6	N	New	37.30	3.310	14	-
carbon dioxide	LJ	C	Harris	28.13	2.757		+0.6512
	Exp-6		(EP) _{CO₂}	28.07	2.753	14	+0.6466
	LJ	O	Harris	80.51	3.033		-0.3255
	Exp-6		(EP) _{CO₂}	83.20	3.029	14	-0.3233
water	Exp-6	O	(EP) _{H₂O}	159.78	3.195	14	-0.7374
	LJ		SPC/E	78.21	3.167	12	-0.8476
		H	(EP) _{H₂O}	-	-	-	+0.3687
		H	SPC/E	-	-	-	+0.4238

for the Coulombic energy of interaction between point charges. The parameters q_γ and q_δ are the values of given point charges, $r_{\gamma\delta}$ is the distance between two point charges and ϵ_o is the permittivity of a vacuum. The parameters for each model studied in this chapter are summarized in Table 4.1.

As our primary goal is to build fine-lattice models to reproduce the properties of real systems studied in Chapter 3, we use the intermolecular potential model obtained for nitrogen in that chapter in order to test the applicability of the lattice discretization technique. For carbon dioxide, two sets of potential parameters are considered, one from Harris and Yung [105] (abbreviated as ‘‘Harris model’’ from this point on), the second one from Errington and Panagiotopoulos [106] (abbreviated as (EP)_{CO₂} model from this point on). For the water case study, the well known SPC/E (simple point charge/extended) model [92] and also the model proposed by Errington and Panagiotopoulos [95] (abbreviated as (EP)_{H₂O} model

from this point on) are considered for intermolecular potential parameters. Here, we extend the previous work by studying the same models but in lattice space and with an emphasis on whether the thermodynamic properties of the new proposed lattice methodology are comparable to the off-lattice results studied for both polar real systems, carbon dioxide and water.

While the interaction energy parameters remain unchanged, the bond length and bond angles must be altered to force each bond to span an integer number of lattice spaces while adhering as closely as possible to continuum values. Unfortunately, this procedure can lead to sizeable errors due to restrictions placed on separation distance, where a site's location can only be described by any number between zero and box length in all the dimensions. The set of configurations for a particular value of ζ were determined in the following manner: the lattice spacing σ/ζ was fixed and the minimum and maximum allowable values for the bond lengths and bond angles were set to particular values. All possible configurations of a model molecule on a lattice were found between these parameters. The structural parameters of the models studied are shown in Table 4.2 for different values of ζ . For example, if $\zeta = 8$, one possible configuration for carbon-dioxide model would be

$$\begin{bmatrix} 0 & 0 & 0 \\ -3 & -1 & -1 \\ 3 & 1 & 1 \end{bmatrix} \quad (4.5)$$

in which the first line represents the position of carbon atom and latter two lines are the coordinates of the two oxygens, all in number of lattice units. In this example, the bond length between each carbon and oxygen is 1.1338\AA and the bond angle is 180° , compared with the continuum values of 1.1433\AA and 180° . In principle and as it is obvious from the Table 4.2, the deviation between the average bond length

Table 4.2: Structural parameters for nitrogen, carbon dioxide, and water.

Molecule	ζ	bond length(\AA)	bond angle($^\circ$)
Nitrogen	12	0.3273	-
Carbon dioxide	8	1.1338	180.00
	12	1.1173	180.00
	20	1.1224	180.00
	∞	1.1433	180.00
Water	8	1.0500	109.47
	13	1.0607	109.47
	21	1.0609	109.08
	32	1.0677	109.47
	∞	1.0668	109.50

in lattice and continuum spaces does not necessarily decrease on increasing the ζ value. However, the possible number of configurations increases upon increasing the lattice discretization parameter, ζ , but there was no observed difference in the final phase envelope results, if the number of configurations is of order 10, 100, or 1000. For simplicity and to save computational time a set with smallest number of configurations were chosen.

The multihistogram reweighting grand canonical Monte Carlo method was used for obtaining the thermodynamic properties, mainly the phase behavior (for details of the simulation see Chapter 3). Both models belong to the same universality class and we use the finite size scaling method of Bruce and Wilding [18, 22] to estimate the critical points.

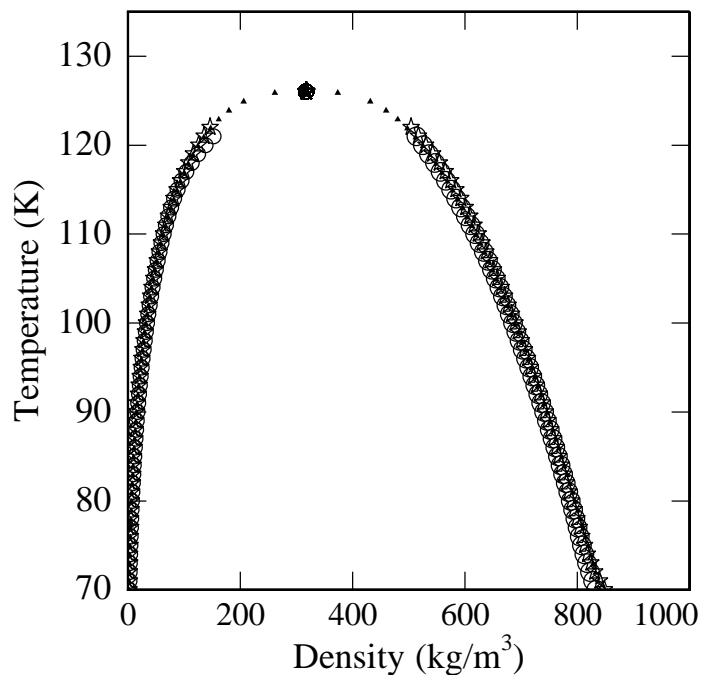


Figure 4.1: Phase behavior of the nitrogen model from histogram reweighting GCMC simulations: N_2 model with $\zeta = 12$ (open stars), off-lattice data (open circles), and experimental data [6] (filled triangles).

4.3 Results and discussion

4.3.1 Nitrogen model

Since the phase behavior of LJ particles was qualitatively captured by a lattice discretization value of $\zeta = 10$ [3], we expected to be able to capture the phase behavior of nitrogen by a value of $\zeta = 12$. The coexistence behavior of the nitrogen model with a lattice discretization parameter of $\zeta = 12$ is compared to both experimental and off-lattice values in Fig. 4.1, where the uncertainties of the simulated points are less than the size of the symbol. The off-lattice data are based

on the calculations in Chapter 3 for the nitrogen model, but in continuum-space. The saturated densities and critical parameters, mainly critical temperature and critical density are in good agreement with experiment. In next subsections we apply the fine-lattice discretization technique to more complicated molecules such as carbon dioxide and water.

4.3.2 Carbon dioxide model

The coexisting densities for $(EP)_{CO_2}$ model with a lattice discretization parameter of $\zeta = 8$, is compared to both experimental and off-lattice values in Fig. 4.2. The uncertainties of the simulated points are less than the size of the symbol. The saturated liquid densities are in good agreement with both off-lattice and experimental data. The saturated gas densities deviate a little bit for higher temperatures but for lower temperatures, the agreement with both experimental and off-lattice simulations data is good. The phase coexistence results for $(EP)_{CO_2}$ carried out with $\zeta = 10$ and 12 are shown in Fig. 4.3. To our surprise, the same trend for higher values of temperatures in gas region is observed for both systems. The Harris model [105] in lattice space using a lattice discretization parameter, $\zeta = 8$, was also studied. Phase coexistence data for Harris model in both lattice and continuum spaces are shown in Fig. 4.4. The critical temperature and critical density for all the models studied with the corresponding off-lattice data are shown in Table 4.3. Overall, the agreement for phase behavior and critical points are good and within symbol size. All the carbon dioxide models studied up to this point were calculated in a system size of $L^* = L/\sigma = 7$, where L^* is the dimension of the box in reduced units. Fig. 4.5 illustrates our results for the critical ordering distribution at the estimated critical point for $\zeta = 8$ and $L^* = 7$. It is believed

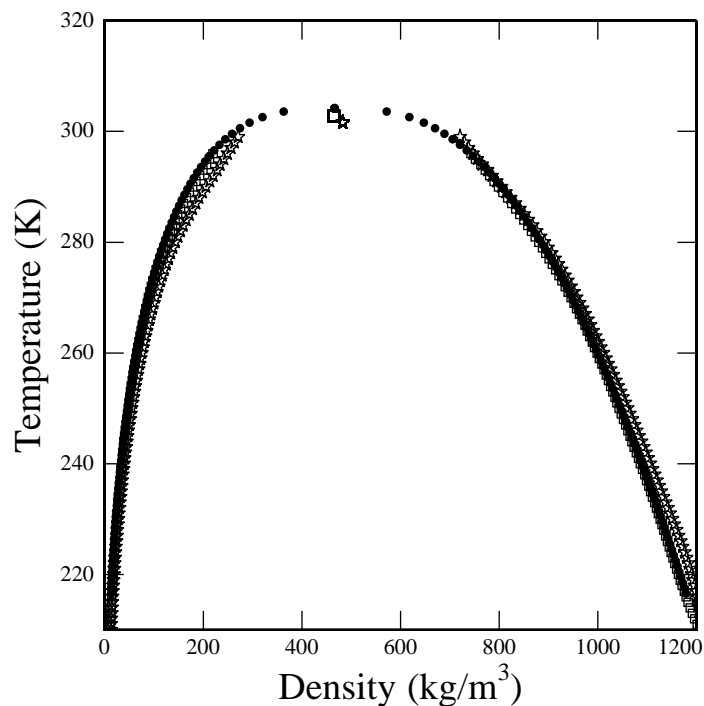


Figure 4.2: Phase behavior of the carbon dioxide model from histogram reweighting GCMC simulations. $(EP)_{CO_2}$ model with $\zeta = 8$ and $L^* = 7$ (open stars), off-lattice data (open circles), and experimental data [6] (filled diamonds).

that the deviation from the Ising distribution is not a consequence of inadequate sampling but a finite-size effect. However, Fig. 4.6 shows the coexistence data for the carbon dioxide model with $\zeta = 8$, but $L^* = 10$, and to our surprise, the same trend is observed for bigger system size. The critical ordering distribution at the estimated critical point for $\zeta = 8$, but $L^* = 10$ is shown in Fig. 4.7 and the matching is perfect.

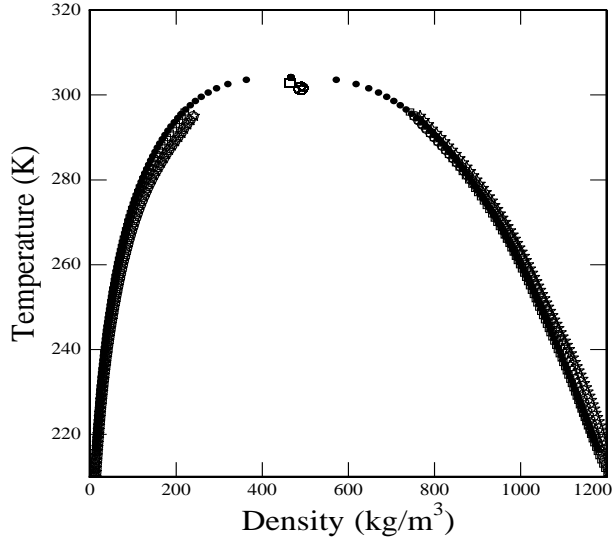


Figure 4.3: Phase behavior of the carbon dioxide model from histogram reweighting GCMC simulations. $(EP)_{CO_2}$ model with $\zeta = 12$ and $L^* = 7$ (open stars), $(EP)_{CO_2}$ model with $\zeta = 20$ and $L^* = 7$ (open circles), off-lattice data (open squares), and experimental data [6] (filled diamonds).

Table 4.3: Critical temperature and critical density of the carbon dioxide models studied. The data lie with a level of confidence of approximately 68 percent.

Molecule	Type	L^*	ζ	$T_c(K)$	$\rho_c(kg/m^3)$
Carbon dioxide	$(EP)_{CO_2}$	7	8	301.6 ± 0.3	483 ± 4
	Harris	7	8	302.7 ± 0.2	481 ± 5
	$(EP)_{CO_2}$	7	12	301.7 ± 0.4	492 ± 4
	$(EP)_{CO_2}$	7	20	301.5 ± 0.3	490 ± 3
	$(EP)_{CO_2}$	10	8	301.9 ± 0.2	486 ± 2
	$(EP)_{CO_2}$	7	∞	302.8 ± 0.5	465 ± 1
	Experiment	-	∞	304.1	466.5

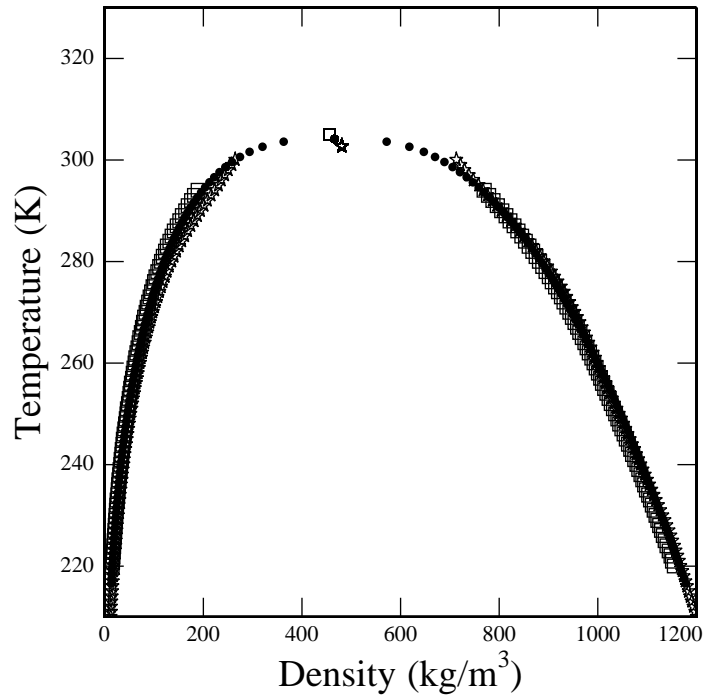


Figure 4.4: Phase behavior of the carbon dioxide model from histogram reweighting GCMC simulations. Harris model with $\zeta = 8$ and $L^* = 7$ (open stars), off-lattice data (open squares), and experimental data [6] (filled circles).

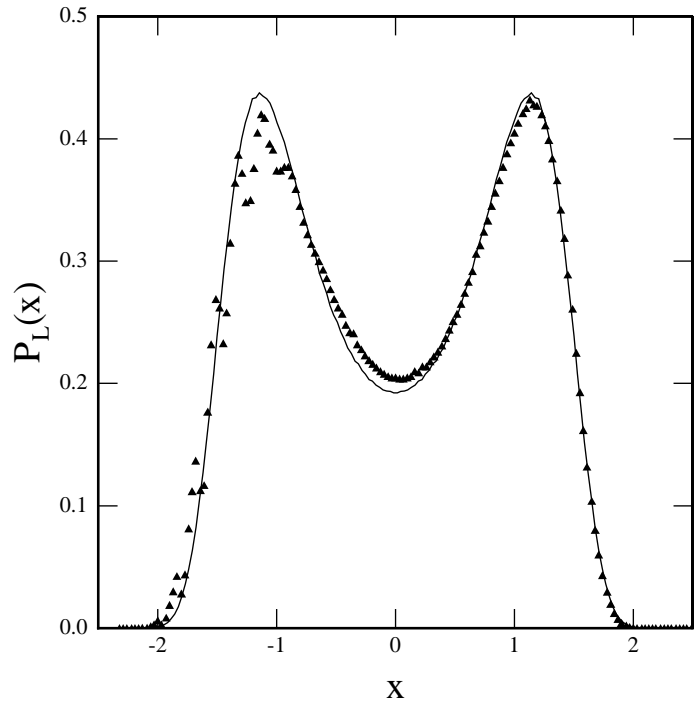


Figure 4.5: Matching of the scaled order parameter distribution to the universal curve for the Ising three-dimensional universality class, indicated by the continuous line. Points are from our simulations for the $(EP)_{\text{CO}_2}$ model with $\zeta = 8$ and $L^* = 7$.

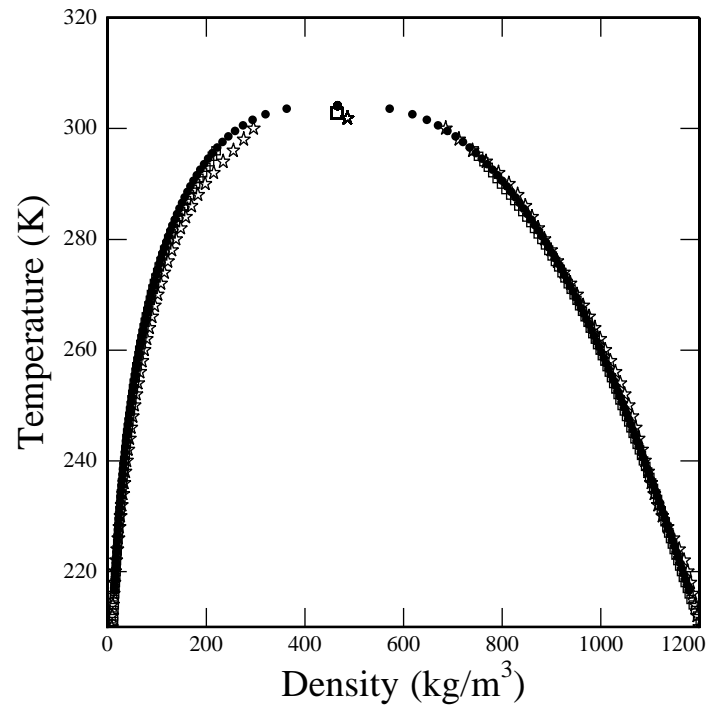


Figure 4.6: Phase behavior of the carbon dioxide model from histogram reweighting GCMC simulations: $(EP)_{\text{CO}_2}$ model with $\zeta = 8$ and $L^* = 10$ (open stars), off-lattice data (open circles), and experimental data [6] (filled diamonds).

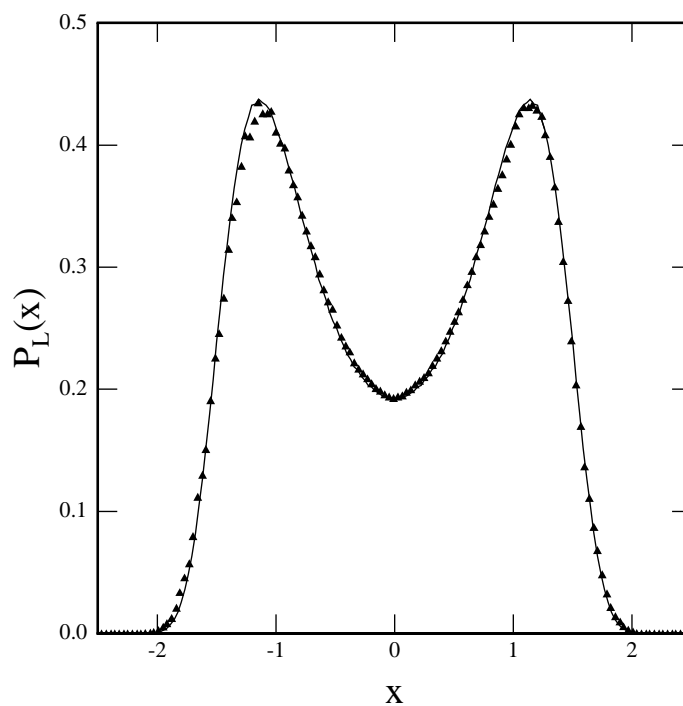


Figure 4.7: Matching of the scaled order parameter distribution to the universal curve for the Ising three-dimensional universality class, indicated by the continuous line. Points are from our simulations for the $(EP)_{\text{CO}_2}$ model with $\zeta = 8$ and $L^* = 10$.

Table 4.4: Estimates of critical temperature with different lattice discretization parameter, ζ , for the water model studied.

Molecule	ζ	$T_c(\text{K})$
water	8	608 ± 1
	13	623 ± 1
	21	628 ± 1
	32	637 ± 1
	∞	645.9 ± 1.1

4.3.3 Water model

Estimates of the critical temperatures of the water models studied in lattice space are shown in Table 4.4 along with the off-lattice ($\zeta = \infty$) value. The comparison of the critical temperatures of four different water models with the off-lattice value shows that water properties are strongly influenced by the structural properties of the configurations used during the simulation. The study shows that the set of configurations with bigger lattice discretization parameter, ζ , has the closest average bond length value to the off-lattice value and there is a good agreement between the off-lattice and lattice phase coexistence data. Small changes in the bond length resulting from different lattice discretization parameters introduce large deviations in the critical temperature and subsequently the coexistence behavior, where the deviations of the average bond lengths in lattice space and continuum-space are clearly below 2%. As shown in Fig. 4.8, the saturated liquid density results compare well with the off-lattice simulation results. However the saturated gas density shows a small deviation at temperatures close to critical

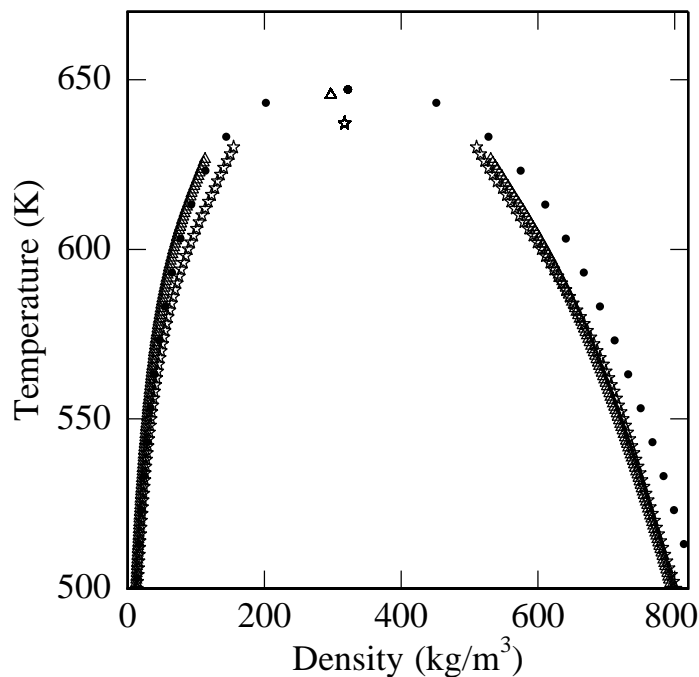


Figure 4.8: Phase behavior of the water model from histogram reweighting GCMC simulations. $(EP)_{\text{H}_2\text{O}}$ model with $\zeta = 32$ and $L^* = 5.4$ (open stars), off-lattice data (open triangles), and experimental data [6] (filled circles).

temperature. The collapse of the measured $P_L(x)$ on the universal Ising ordering operator distribution is shown in Fig. 4.9. As it is obvious from the Fig 4.9, the small system size of the simulation affects the low density part of the curve. Deviations between our results and Ising universality class are obvious in the low-density region, here, we decided to work with bigger system size, since this insures that proper matching between the results from our simulation and the Ising universality is obtained and finite size effect has diminished to a larger extent. Here and in the following the phase behavior results are calculated in a system size of $L^* = 6.7$ and the $P_L(x)$ distribution function is shown in Fig. 4.10. As it is shown in Fig. 4.10,

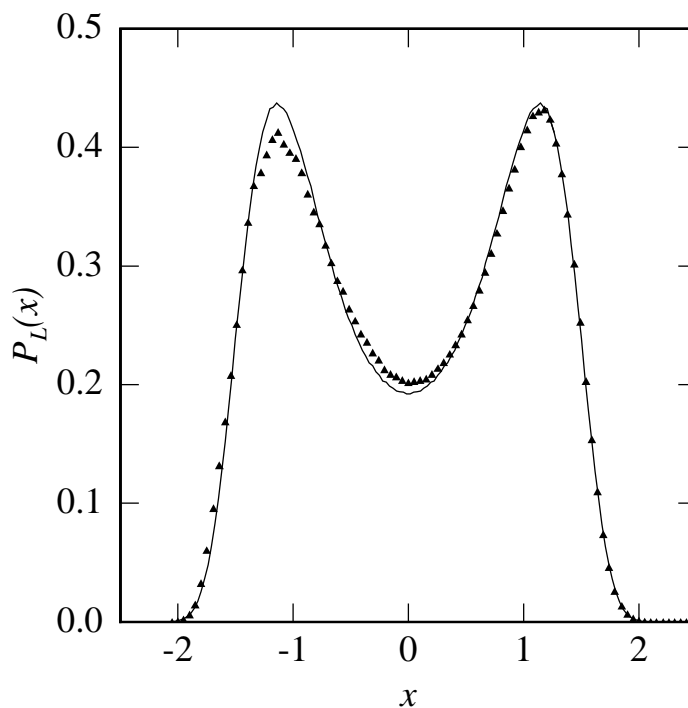


Figure 4.9: Matching of the scaled order parameter distribution (as obtained by the method indicated in Sec. 2.4) to the universal curve for the Ising three-dimensional universality class: see the continuous line. Points are from our simulations for the $(\text{EP})_{\text{H}_2\text{O}}$ model with $\zeta = 32$ and $L^* = 5.4$.

the system size effect has diminished to a large extent for this system size and as shown in Fig. 4.11, the lattice model accurately predicts the saturated liquid densities over the entire range. The gas saturated densities are underestimated at higher temperatures close to critical temperature, but in overall they are in good agreement at lower temperature values. We still postulate that the small deviation for saturated gas densities for temperatures close to critical temperature is due to either system size effect or the errors due to the restrictions placed on structural properties of the molecules in lattice space, but the computational cost to investi-

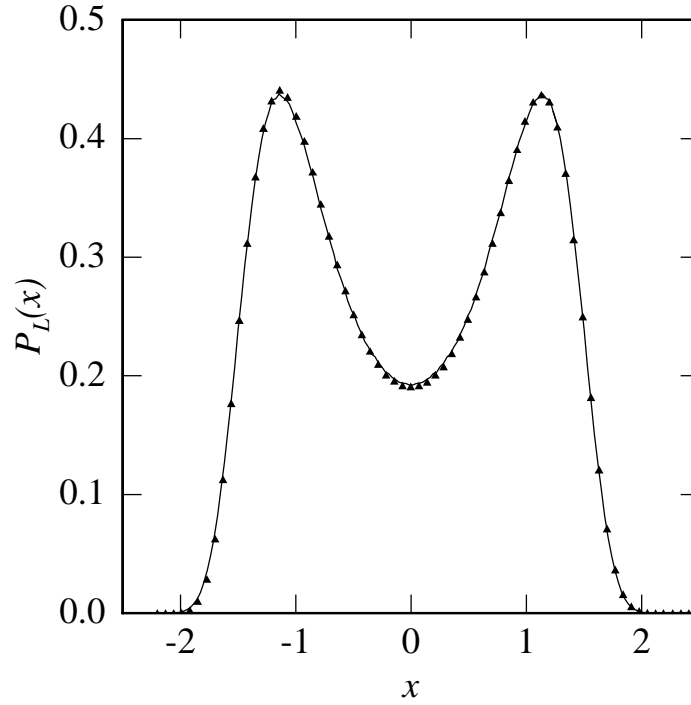


Figure 4.10: Matching of the scaled order parameter distribution to the universal curve for the Ising three-dimensional universality class, indicated by the continuous line. Points are from our simulations for the $(\text{EP})_{\text{H}_2\text{O}}$ model with $\zeta = 32$ and $L^* = 6.7$.

gate this feature is prohibitively high and prevented us from further investigation. The approach for solving this problem is discussed as part of the future work. the critical temperature and critical density for the water model with $\zeta = 32$, in two different system sizes are shown in Table 4.5.

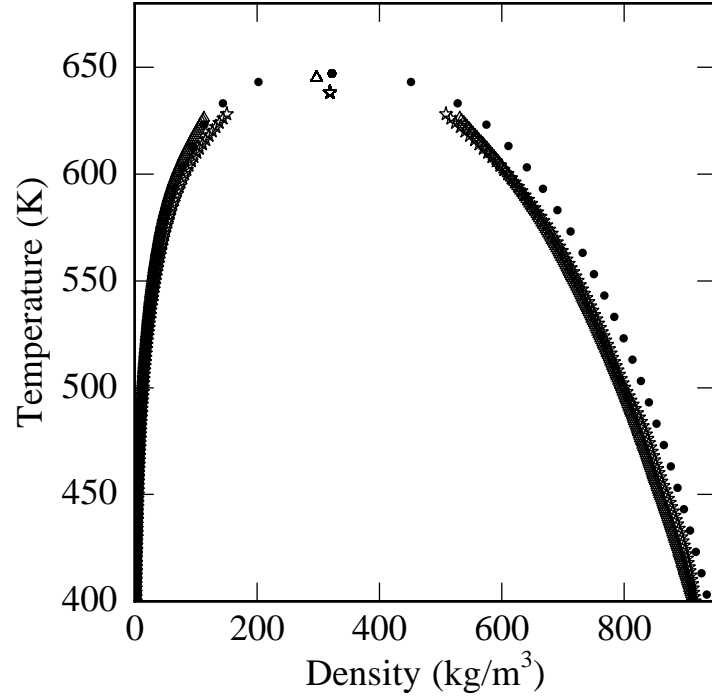


Figure 4.11: Phase behavior of the water model from histogram reweighting GCMC simulations. (EP)_{H₂O} model with $\zeta = 32$ and $L^* = 6.7$ (open stars), off-lattice data (open triangles), and experimental data [6] (filled circles).

Table 4.5: Critical temperature and critical density as a function of system size for the water models studied.

Molecule	Type	L^*	ζ	$T_c(\text{K})$	$\rho_c(\text{kg/m}^3)$
water	(EP) _{H₂O}	5.4	∞	645.9 ± 1.1	297 ± 5
	(EP) _{H₂O}	5.4	32	637.1 ± 0.9	317 ± 4
	(EP) _{H₂O}	6.7	32	638.2 ± 0.8	319 ± 5
Experiment	-	-	∞	647.1	322

4.3.4 Water structure - canonical Monte Carlo simulations

In the work of Lock [109], it is shown that the agreement between discretized and continuum models of SPC/E [92] is heavily dependent upon the exact value of the lattice discretization parameter, ζ . For example, some discretized models were observed to “freeze” into a hexagonal ice-like structure at temperatures up to $T = 550$ K. It was shown that changes in the lattice spacing as small as 0.01 nm can have surprisingly strong effects on the structural properties of discretized models, resulting in solid-like order at temperatures much higher than the experimental melting point. In this part of the thesis, some calculations are reported that have been done to investigate the effect of lattice discretization on structural properties at temperatures close and far from critical point. In this stage of the work, we are interested in working in dense systems where the acceptance of adding and removing a particle is too low to ensure equilibrium in a reasonable amount of time; thus all simulations have been performed in the canonical ensemble. In the canonical Monte Carlo (NVT) method, the number of particles N , the temperature T , and volume V are fixed. The partition function and probability density for this ensemble is defined as

$$Q(N, V, T) \equiv \frac{1}{\Lambda^{3N}} \int dr^N \exp[\beta U(r^N)], \quad (4.6)$$

where $\Lambda = \sqrt{\frac{h^2}{2\pi m k_B T}}$ is the thermal de Broglie wavelength. From the partition function, it follows that the probability of finding configuration r^N given by distribution is:

$$\mathcal{P}(r^N) \propto \exp[\beta U(r^N)]. \quad (4.7)$$

Eqs. 4.6 and 4.7 are the basic equations for a simulation in the canonical ensemble. Each step consists of either a translation or rotation on one molecule chosen

at random. Translation and rotation moves are attempted equally often. When attempting a rotation move, the trial structure is chosen from a subset of the reservoir to encompass those structures most similar to current structure. In this way, considerable care is taken to ensure that all subsets overlap so that each molecule can sample all structures from the reservoir over the course of the simulation.

To study the situation, we consider a linear graph of nodes and connecting bonds or links. The number of nodes is taken equal to the number of structures in the reservoir, with each node representing one of the structures. The connectivity between any two nodes is defined based on the possibility of transition between the corresponding structures in a single step. Obviously, if a wider range of rotation angles is selected for the moves, each node will be connected to a larger number of nodes compared to the case with a limited rotation angle. Our main concern in these experiments is to make sure all structures are visited by the system and none of them are left out. This is equivalent to ensuring that the graph is connected i.e., there is a path between any two nodes on the graph. For each choice of the rotation range, we constructed the adjacency matrix of the corresponding graph. For a graph with N nodes, The adjacency matrix $A = [a_{ij}]$; $i, j = 1, \dots, N$ is defined as

$$a_{ij} = \begin{cases} 1 & \text{if node } i \text{ is connected to } j \\ 0 & \text{otherwise} \end{cases} \quad (4.8)$$

Obviously, A is a symmetric matrix. It is also well-known that A in fact shows the number of paths with unit length between any two nodes. Similarly, each element $[a_{ij}^n]$ of matrix A^n shows the number of paths with length n between nodes i and j . Since we were only interested in the existence of at least one path of any length between any two nodes, in our experiments, we need to calculate all A^n matrices

Table 4.6: Geometric properties of various discretized water models compared with the continuum model ($\zeta = \infty$).

ζ	bond length(Å)	bond angle(°)	dipole moment(D)
10	1.0011	107.46	2.41
11	1.0241	108.44	2.44
12	0.9870	110.92	2.28
20	1.0011	107.46	2.41
21	1.0031	108.78	2.38
22	1.0134	108.87	2.40
30	0.9969	109.36	2.35
∞	1.00	109.5	2.35

for $n = 1, 2, \dots, N$ and check if for any i and j at least one $[a_{ij}^n]$ element is non-zero.

Using the definition of matrix exponentials, we simply calculated

$$B = A + \frac{A^2}{2!} + \frac{A^3}{3!} + \dots = e^A - I \quad (4.9)$$

and made sure all elements of B are greater than zero.

The effects of the underlying lattice on water's density profile over a wide range values of $\zeta = 10, 11, 12, 20, 21, 22,$ and 30 , for different temperatures of, $T = 640$ K and 550 K, and 400 K are studied with a reduced density close to 1. The simple averages of the bond angles, bond lengths, and dipole moments for a sample of discretized water molecules at various ζ are shown in Table 4.6. Only density profiles in the z -direction are shown, although the density profiles in all dimensions have been calculated and have been found isotropic.

In Fig. 4.12, the profiles of seven discretized models and the continuum

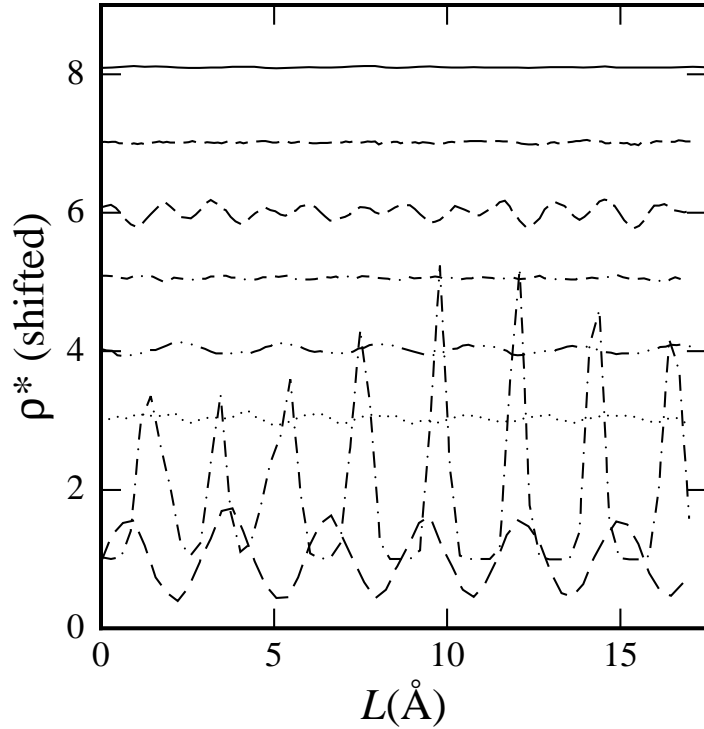


Figure 4.12: Density profile of discretized models of SPC/E water at $T = 400$ K. The curves from bottom to top are for $\zeta = 10, 11, 12, 20, 21, 22, 30,$ and ∞ .

model are shown. As expected, the profile for the continuum model ($\zeta = \infty$) is almost perfectly flat; there is no underlying structure in the fluid. This is also true for discretized models with $\zeta = 21$ and 30 . As it is shown in Fig. 4.12, there are clearly some ordering in the fluid for discretized models with discretization values of $\zeta = 10, 11, 12, 20,$ and 22 , at $T = 400$ K. It is striking that some strong underlying structures are formed for a ζ value of 11 and to a minor extent for the other discretized models. The same trend is seen here as was observed by Lock [109], except that some underlying structures are also shown for $\zeta = 12$. The oxygen-oxygen radial distribution function $g(\text{OO})$ (negative-negative) for these

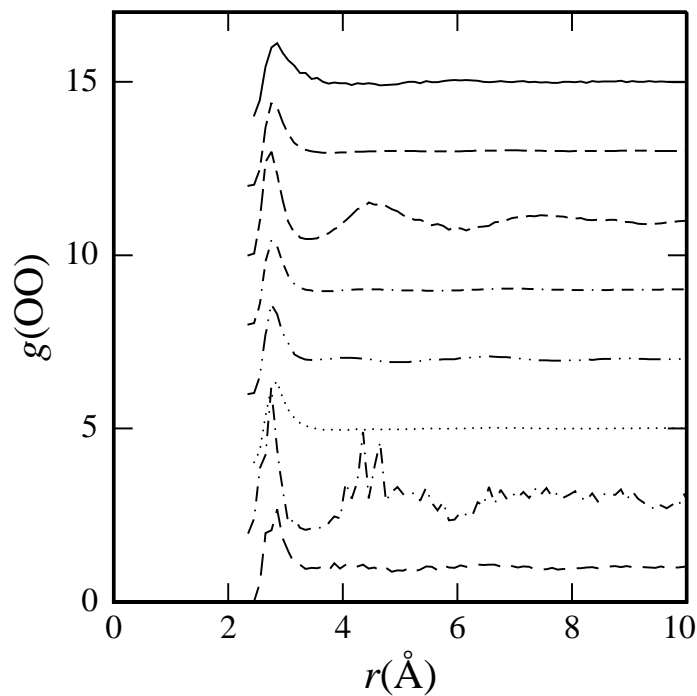


Figure 4.13: Oxygen-oxygen radial distribution functions of discretized models of SPC/E water at $T = 400$ K. The curves are the same as Fig. 4.12.

seven discretized models are shown in Fig. 4.13. The models that show flat profiles also show continuum-like radial distribution function as this is true for all the discretized models except for $\zeta = 11$ and 22. The anomalies are much less extensive for $\zeta = 10$ and disappeared for $\zeta = 12$ and 20. Lock [109] found the same strong anomalies for $\zeta = 11$ and 22, and to a minor extent for $\zeta = 10$ and 22. As it is obvious for the discretized lattice model with $\zeta = 11$, the radial distribution shows ordered structures that one would not expect for a liquid. The oxygen-hydrogen (negative-positive) and hydrogen-hydrogen (positive-positive) radial distribution functions are also shown in Figs. 4.14 and 4.15, respectively. The results observed for discretized model with $\zeta = 11$, are intriguing, as they suggest that there

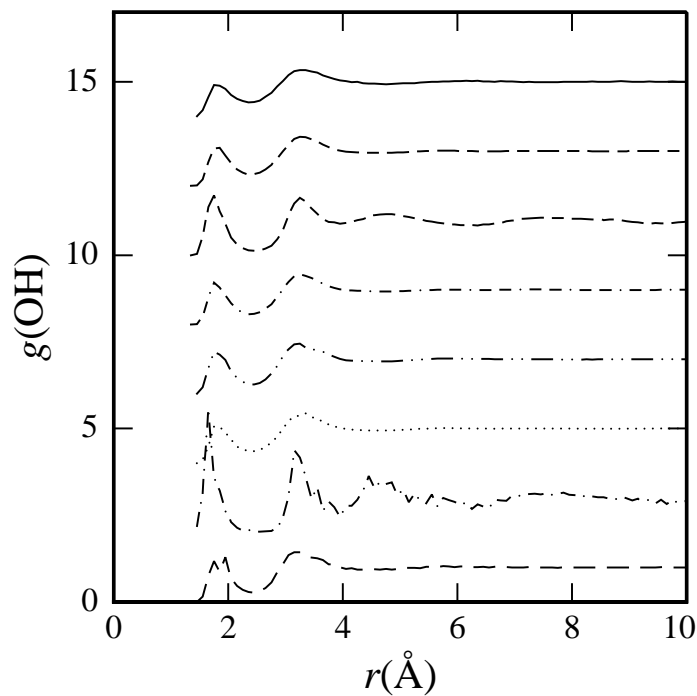


Figure 4.14: Oxygen-hydrogen radial distribution functions of discretized models of SPC/E water at $T = 400$ K. The curves are the same as Fig. 4.12.

is a distinct structure in the fluid. To determine the structure more carefully, we looked at snapshot of its configuration at the end of the simulations. The sample for $\zeta = 11$ is shown in Fig. 4.16 and one can see unmistakably hexagonal structures similar to Ice-Ih.

The ordered structures present at $T = 400$ K do not persist at higher temperatures as seen in Fig. 4.17. In fact, as it is shown in Fig. 4.17, there appears to be no underlying structure for all discretized models studied at this temperature, namely, $T = 550$ K. On the other hand, Lock [109] observed some order in the fluid structure at this temperature for $\zeta = 11$ and to a minor extent for $\zeta = 10$. The radial distribution functions g for these seven discretized models along with

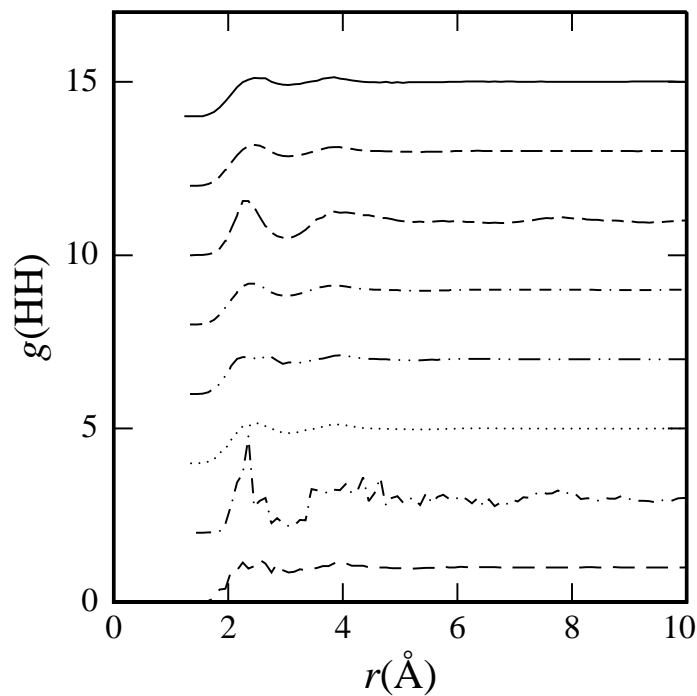


Figure 4.15: Hydrogen-hydrogen radial distribution functions of discretized models of SPC/E water at $T = 400$ K. The curves are the same as Fig. 4.12.

the continuum model are shown in Figs. 4.18, 4.19, and 4.20. The models that show flat profiles also show continuum-like radial distribution for all pairs $g(\text{OO})$, $g(\text{OH})$, and $g(\text{HH})$.

In Fig. 4.21, the profiles of seven discretized models and the continuum model at $T = 640$ K, above the critical point for continuum SPC/E model, are shown. As expected, the profiles for all the models are flat and there is no underlying structure in the fluids. The oxygen-oxygen radial distributions for the same models are shown in Fig. 4.22, and the same trend is observed. The same trend for this temperature for all the seven discretized models was also observed by Lock [109].

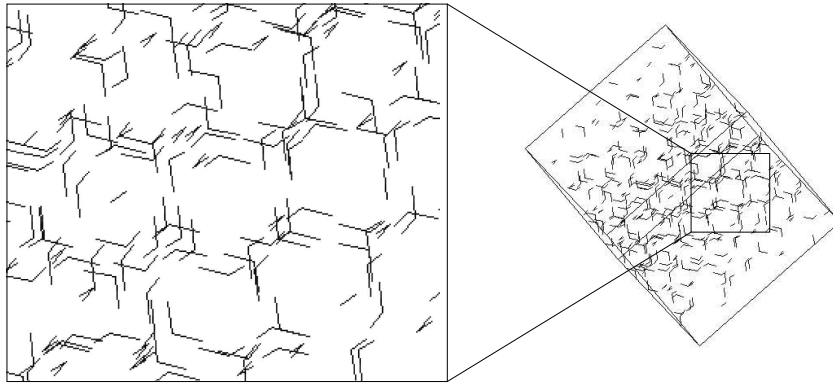


Figure 4.16: Snapshot of a configuration of SPC/E water at $T = 400$ K. with $\zeta = 11$.

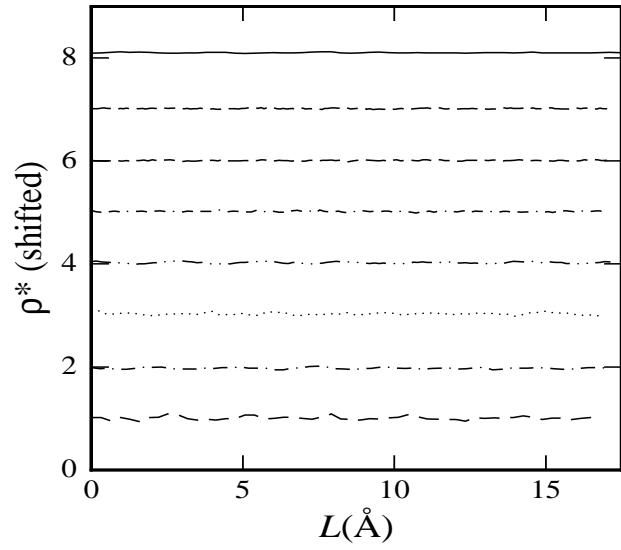


Figure 4.17: Density profile of discretized models of SPC/E water at $T = 550$ K. The curves from bottom to top are for $\zeta = 10, 11, 12, 20, 21, 22, 30,$ and ∞ .

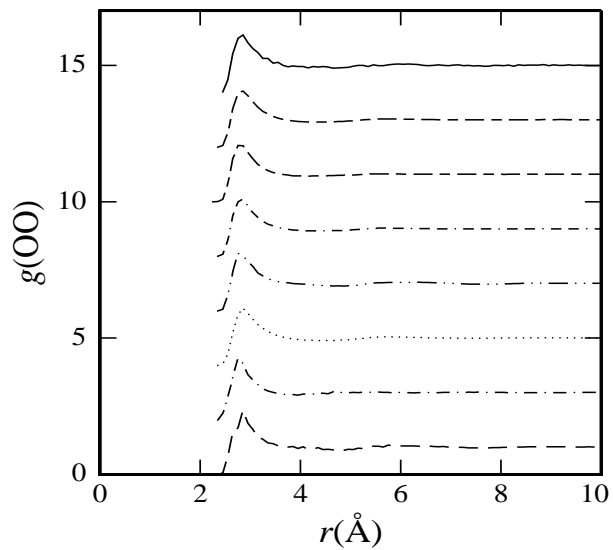


Figure 4.18: Oxygen-oxygen radial distribution functions of discretized models of SPC/E water at $T = 550$ K. The curves are the same as Fig. 4.17.

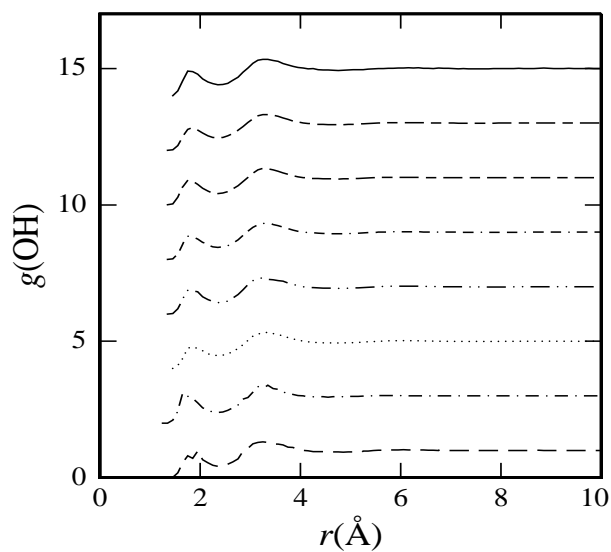


Figure 4.19: Oxygen-hydrogen radial distribution functions of discretized models of SPC/E water at $T = 550$ K. The curves are the same as Fig. 4.17.

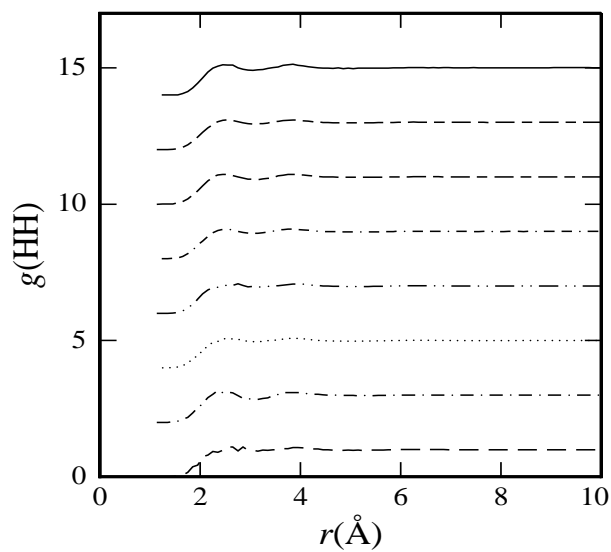


Figure 4.20: Hydrogen-hydrogen radial distribution functions of discretized models of SPC/E water at $T = 550$ K. The curves are the same as Fig. 4.17.

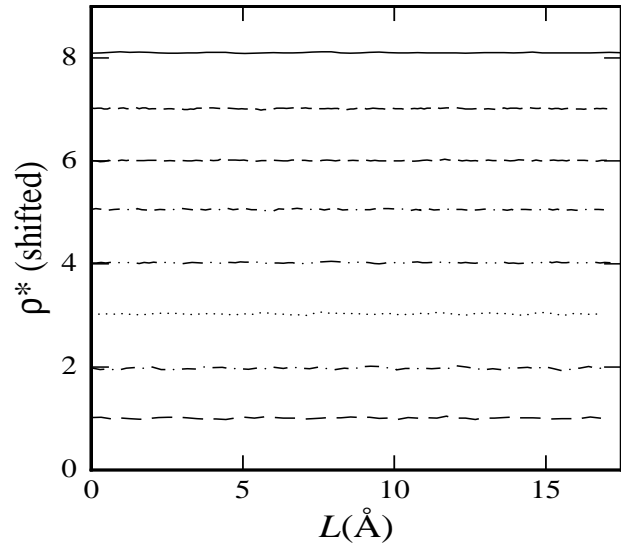


Figure 4.21: Density profile of discretized models of SPC/E water at $T = 640$ K. The curves are the same as Fig. 4.17.

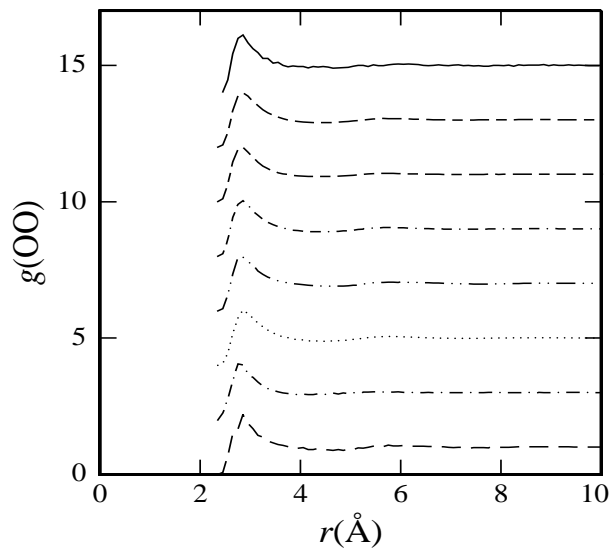


Figure 4.22: Oxygen-oxygen radial distribution functions of discretized models of SPC/E water at $T = 640$ K. The curves are the same as Fig. 4.17.

4.4 Conclusions

In conclusion, we can safely say that even small changes in the lattice discretization parameter, ζ , can have a large effect on the structural properties of the water models studied. When water models are discretized in lattice space, the allowable values for bond length, bond angle, and dipole moment are not exactly the same as the continuum values and could cause the strange results observed. For example both the average bond length and the average dipole moment of molecular structures used for the water model with lattice discretization parameter of $\zeta = 11$, have the largest deviation from the continuum value. We postulate that the large deviations for both the average bond length and the average dipole moment are among the reasons for the odd behavior observed for both the density profile and the radial distribution functions of the water model at $T = 400$ K. On the other hand, the average dipole moment of the molecular structures used for the water model with $\zeta = 21$ has the smallest deviation from the continuum counterpart and the average bond length deviation from its continuum counterpart is small and less than 0.4%; consequently normal behavior is observed for both density profile and radial distribution functions at $T = 400$ K. There is no direct relation between the behavior of other water models with $\zeta = 10, 12, 20,$ and 22 and the deviation of both their average bond lengths and average dipole moments from the continuum counterparts. At this point no final explanation can be given for the relations among the deviations observed between the average bond length, bond angle, and average dipole moment from their continuum counterparts and the structural properties studied in this work. No peculiar behavior is observed for either of the water models at $T = 550$ K, whereas Lock [109] sees abnormal behaviors for some of the water models at $T = 550$ K. The only difference between our calculations and the

calculations done by Lock for the water models is that Lock uses canonical simulations from the beginning, whereas we initially use grand canonical simulations to obtain the high density structural configuration as an initial configuration for the later canonical simulations. Since all the calculations are done in the high density region, we postulate that the systems reach equilibrium only after a considerable time and that might be the source of the difference between the results observed by us and by Lock [109]. This subject is open for further investigation and we discuss it briefly in Chapter 8.

Chapter 5

Lattice Discretization Effects on the Critical Parameters of Model Non-polar and Polar Fluids¹

5.1 Introduction

We have observed that small changes in the lattice discretization parameter, ζ , can have either small or large effects on the thermodynamic and structural properties of the fluids calculated using fine lattice discretization technique. As a long-term motivation is to build fine-lattice models reproducing properties of real systems, it is desirable to understand the influence of intermolecular potentials on the approach of thermodynamic and structural properties to the continuum limit.

In the study of Panagiotopoulos [110] on a cubic lattice for a simple electrolyte model known as the restricted primitive model (RPM), both critical temperature

¹All of the results presented in this chapter have also been published in [66].

and critical density were found to decrease on increasing the lattice discretization parameter ζ . The deviations of the critical parameters from the continuum ($\zeta \rightarrow \infty$) values were found to scale as $1/\zeta^2$. At this stage we are interested in studying the exact effects of the lattice discretization parameter for potential models other than RPM and in investigating whether the same strong effect of the lattice discretization parameter on critical parameters, mainly the critical temperature and the critical density, can be observed. We study this effect for simple monatomic and diatomic non-polar systems with soft-core short range interactions. We also investigate this effect on more complicated polar systems such as two-bead and three-bead chains with hard-core interactions.

The outline of this chapter is as follows: Section 5.2 is devoted to a brief description of computational methods used to obtain the critical parameters. Section 5.3 presents the critical temperature and critical density as functions of the discretization lattice parameter for a range of fluids from simple non-polar to three beads polar chains. Finally, conclusions are presented in Section 5.4.

5.2 Simulation methods

We used grand canonical Monte Carlo (GCMC) simulations in cubic boxes of dimension L^3 , under periodic boundary conditions, along with multihistogram reweighting. As in previous chapters, new microstates were generated by a mixture of 50% replacement and 50% addition/annihilation with the standard Metropolis acceptance/rejection criteria [50]. The acceptance ratio of the unbiased insertion/removal steps was 10% near the critical point. The finite-size scaling concepts of Bruce-Wilding [18, 22, 23] were used for obtaining the critical temperature and critical density. The critical temperature and critical density obtained by this

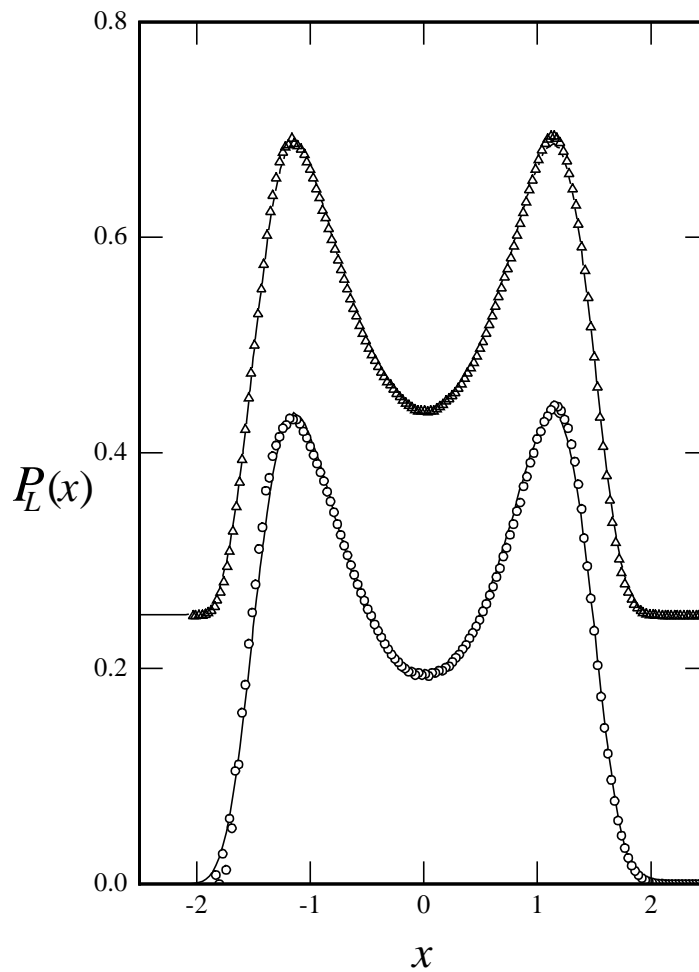


Figure 5.1: Matching of the scaled order parameter distribution to the universal curve for the Ising three-dimensional universality class, indicated by the continuous line for the dumbbell model with $\zeta = 10$. Open circles: $L^* = 12$ and open triangles: $L^* = 15$.

technique are system size dependent and are expected to vary asymptotically as $1/L^{-(\theta+1)/\nu}$ and $1/L^{-(1-\alpha)/\nu}$, where θ , α and ν are Ising universality class exponents [7]. An example of the matching of some of our data to the universal curve is shown in Fig. 5.1. Additional details of the computational approach can be found in Chapter 4.

5.3 Results and discussion

5.3.1 Non-polar model

Two variants are considered for the non-polar model, “monomer” and “dimer” with one and two Buckingham exponential-6 sites respectively. All quantities are made dimensionless by using σ and ϵ as the characteristic length and energy scales for the non-polar model. For example, T^* represents the temperature divided by ϵ/k_B , where k_B is the Boltzmann’s constant; ρ^* represents the density multiplied by σ^3 . An α value of 14 has been used for all the models with Exp-6 interactions. At the beginning of the runs the translationally invariant intermolecular potential is stored in an array of dimension $(L/\zeta)^3$, which accelerates the calculation of the energies during the runs by a factor of 10. In addition to the Exp-6 interactions in the central simulation box, long range corrections according to the method of Theodorou and Suter [83] were applied. To speed up the calculations, all possible orientations for the models studied (except the monomer, which only has one possible orientation) are generated at the beginning of the simulation and stored in a “reservoir.” Once the simulation gets started, a random configuration is selected from the reservoir to be added to the system. The number of configurations (NC) for the tethered dimers increases with the degree of lattice discretization.

For example, there are 6 distinct configurations for $\zeta = 2$ and 318 for $\zeta = 10$, respectively, for dimer systems restricted to remain at a reduced bond lengths, $l^* = l/\sigma$, between 1 and 1.2. However, in order to have the maximum consistency between the systems with different lattice discretization parameters, we selected the same 6 set of distinct configurations for all the systems with different degrees of discretization.

We summarize our results for the critical temperature and critical density for specific lattice discretization parameters in Tables 5.1 and 5.2 . Statistical uncertainties were estimated from independent runs at identical conditions with different random number seeds (algorithm ran2 in Ref [84]) and are reported in parentheses in units of the last decimal place. All the non-polar models with short range interactions show excellent matching to Ising-type criticality. The very small values of the field mixing parameter, s , confirm the symmetry of the non-polar systems. Figs. 5.2 and 5.3 show the dependence of the effective reduced critical temperature, T_c^* , on the inverse lattice discretization parameter for monomer and dimer models, respectively. The best fit was obtained by having the critical temperatures scaled as $1/\zeta^6$ and $1/\zeta^7$ for monomer and dimer models, respectively. Power-law least squares fitting, taking into account the statistical uncertainties, was used to obtain the best exponent. The points for $\zeta < 5$ do not follow the trend of higher values of ζ and were excluded from the extrapolation. Statistical uncertainties for the critical temperatures are comparable to symbol size. As shown in Table 5.1, the critical temperatures and critical densities for values of $\zeta = 10$ and $\zeta = 15$ fall within each other's statistical uncertainties for the monomer model with $L^* = 7$. These results and the high value of the exponent obtained for this model, discouraged us from doing more calculations for values of $\zeta \geq 10$ for the other non-polar models with

Table 5.1: Critical parameters for the “Exp-6 monomer” model.

L^*	ζ	$-\mu_c$	$-s$	T_c^*	ρ_c^*
7	1	4.149(2)	0.01(2)	1.887(4)	0.503(7)
	2	3.911(6)	0.03(1)	1.479(4)	0.354(4)
	3	3.529(2)	0.01(9)	1.301(5)	0.322(2)
	4	3.488(4)	0.01(9)	1.272(3)	0.321(2)
	5	3.472(1)	0.01(1)	1.267(2)	0.324(1)
	6	3.456(3)	0.03(1)	1.258(1)	0.320(4)
	7	3.456(4)	0.03(2)	1.256(3)	0.320(3)
	10	3.453(3)	0.03(3)	1.254(2)	0.319(6)
	15	3.453(3)	0.03(3)	1.254(7)	0.319(9)
10	1	4.133(2)	0.01(1)	1.898(5)	0.500(2)
	2	3.900(4)	0.02(9)	1.483(4)	0.352(9)
	3	3.519(2)	0.01(6)	1.307(6)	0.323(3)
	4	3.478(2)	0.01(6)	1.277(3)	0.322(2)
	5	3.464(2)	0.01(9)	1.271(4)	0.322(9)
	6	3.449(1)	0.01(9)	1.264(6)	0.322(9)
	7	3.446(4)	0.01(3)	1.261(4)	0.322(2)
	10	3.444(4)	0.01(9)	1.259(2)	0.320(9)

Table 5.2: Critical parameters for the “Exp-6 dimer” model.

L^*	ζ	$-\mu_c$	$-s$	T_c^*	ρ_c^*
10	1	8.419(7)	0.01(9)	2.711(5)	0.432(4)
	2	7.480(8)	0.02(4)	2.185(9)	0.341(9)
	3	6.69(1)	0.02(9)	1.926(7)	0.320(5)
	4	6.412(1)	0.01(9)	1.824(7)	0.31(2)
	5	6.348(1)	0.02(3)	1.801(3)	0.308(9)
	6	6.330(7)	0.02(1)	1.796(5)	0.309(5)
	7	6.325(6)	0.02(1)	1.795(9)	0.308(7)
	10	6.326(4)	0.02(1)	1.794(6)	0.30(1)

different system sizes. In Figs. 5.4 and 5.5 the apparent critical temperature, T_c^* , as a function of scaling variable $(L^*)^{-(\theta+1)/\nu}$ for the system with $\zeta = 10$ are shown. We used values appropriate for the Ising universality class for the correction-to-scaling exponent, $\theta = 0.52$ and for the correlation length exponent, $\nu = 0.630$ both from Ref.[7]. The points fall on approximately straight lines. The critical densities decrease on increasing ζ values for both monomer and dimer models. No specific trend has been observed for the critical densities with different values of ζ for the two non-polar models studied, partly as a result of the higher statistical uncertainties associated with the calculation of the critical density.

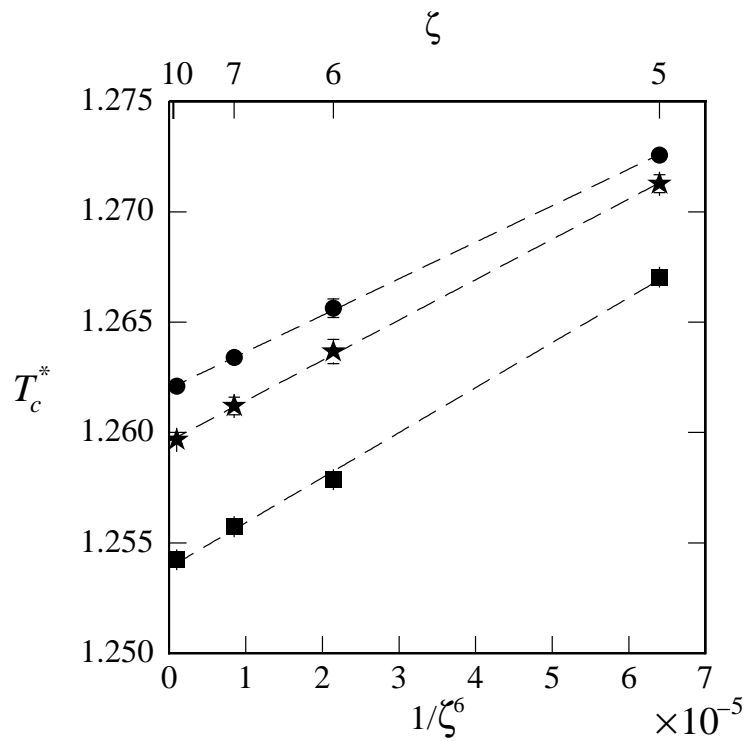


Figure 5.2: Reduced critical temperature, T_c^* , as a function of $1/\zeta^6$ for the “Exp-6 monomer” model with $L^* = 7$ (filled squares), $L^* = 10$ (filled stars), and $L^* = 12$ (filled circles). The dashed line shows the power-law least squares fitting to the data.

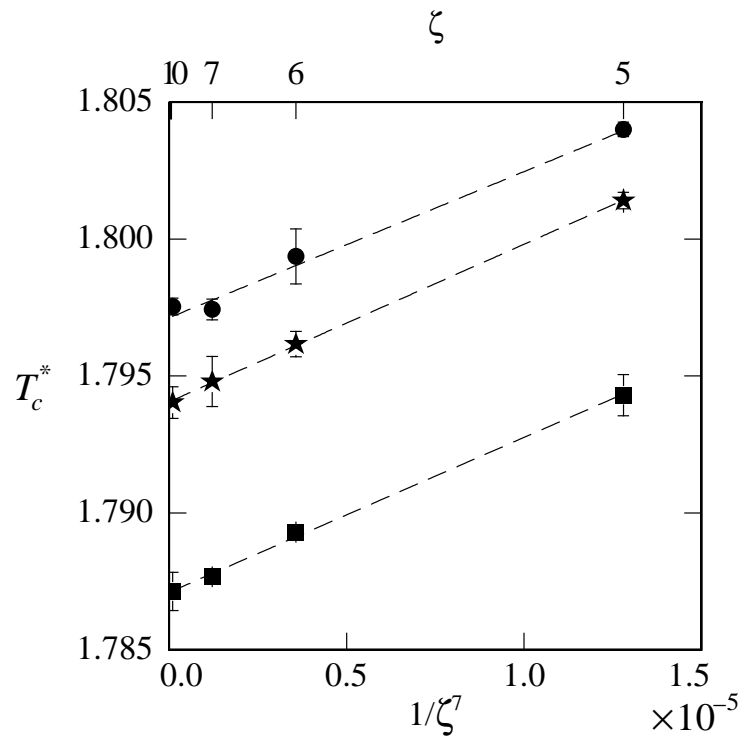


Figure 5.3: Reduced critical temperature, T_c^* , as a function of $1/\zeta^7$ for the “Exp-6 dimer” model with $L^* = 7$ (filled squares), $L^* = 10$ (filled stars), and $L^* = 12$ (filled circles). The dashed line shows the power-law least squares fitting to the data.

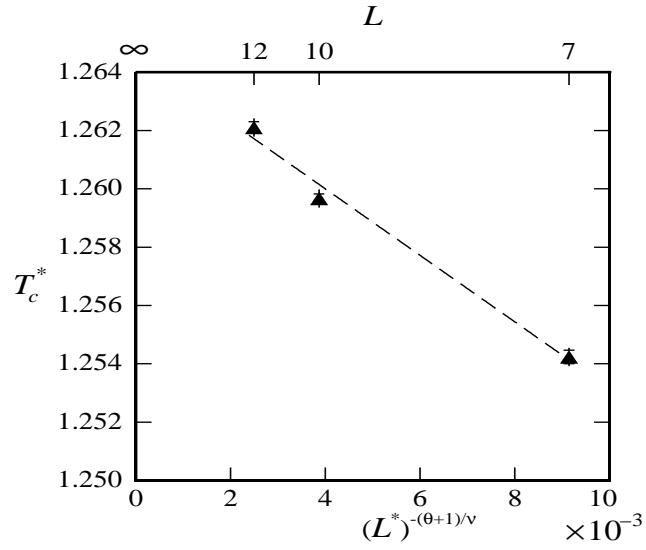


Figure 5.4: Reduced critical temperature, T_c^* , as a function of $(L^*)^{-(\theta+1)/\nu}$ with $\zeta = 10$, for the “Exp-6 monomer” model.

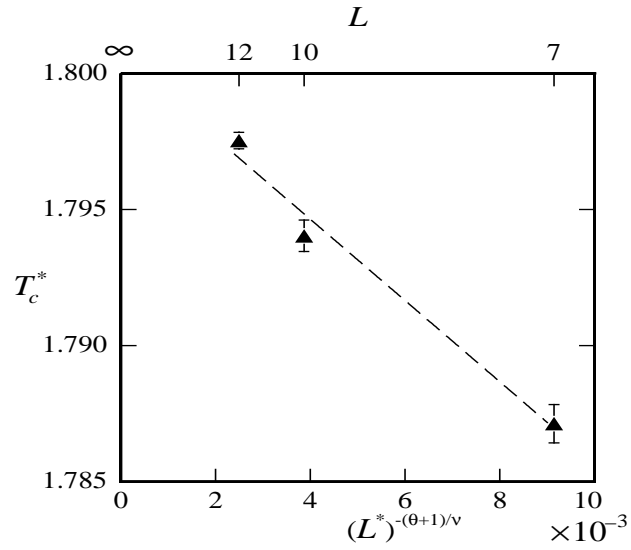


Figure 5.5: Reduced critical temperature, T_c^* , as a function of $(L^*)^{-(\theta+1)/\nu}$ with $\zeta = 10$, for the “Exp-6 dimer” model.

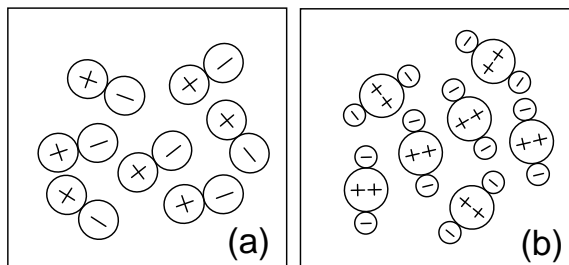


Figure 5.6: Schematic illustration of two polar models considered in this work. (a) The “dumbbell” model; (b) the “trimer” model.

5.3.2 Polar model

We have studied two different models for the polar part of our investigation. The first model considered is a two-bead chain which we refer to as “dumbbell”. It consists of two hard spheres in contact, each with diameter σ . The other model that we have investigated is a three-bead chain referred to as “trimer”. For this model, the center bead and side beads have diameters of 2σ and 1σ , respectively. A schematic view of the models is presented in Fig. 5.6. The Coulombic interaction between two charged sites i and j is defined as:

$$U_{Coul}(ij) = \begin{cases} \infty & \text{if } r < \sigma \\ \frac{q_i q_j}{D r_{ij}} & \text{if } r \geq \sigma \end{cases} \quad (5.1)$$

Where q_i and q_j are charges of sites i and j that are separated by distance r_{ij} and D represents the dielectric constant of the structureless medium. σ is the hard-core diameter for the monatomic model. For both models, reduced temperature and density are defined via $T^* = kTD\sigma/q^2$ and $\rho^* = N\sigma^3/L^3$ where N represents the total number of beads existing in the system. For the unlike molecular collision diameter we used

$$\sigma_{ij} = (\sigma_{ii} + \sigma_{jj})/2 \quad (5.2)$$

Table 5.3: Structural parameters for the dumbbell models. “NC” is the number of configurations with bond length between 1σ and 1.2σ on the lattice with discretization parameter ζ . “DM” and “CH” are the average molecular dipole moment (for the “fixed charge model”) and average electrostatic charge (for the “fixed dipole model”), respectively.

ζ	3	5	7	10	15
NC	30	102	138	318	1158
DM	4.80	4.87	4.83	4.84	4.85
CH	1.00	0.9806	0.9936	0.9915	0.9898

The Ewald summation was applied for polar systems with 518 Fourier-space wave vectors, $k = 5$ real-space damping parameter, and conducting boundary conditions at infinite distance, $\epsilon_\infty = \infty$. The translationally invariant intermolecular potential is stored in an array of size $(L/\zeta)^3$, which accelerated the calculation of the energies by a factor of 100. For the dumbbell case study, the reservoir structural configurations have the same orientations as for the Exp-6 dimer model, but in this case all the possible orientations are used. In the first set of simulations (“fixed charge”) each of the beads carries a unit of charge. In the second set of simulations (“fixed dipole”), all configurations have identical molecular dipole moments, so the charges on each bead vary somewhat. The structural parameters in the two sets of simulations are shown in Table 5.3. Fig. 5.7 shows the dependence of the effective reduced critical temperature, T_c^* , on the inverse lattice discretization parameter squared, $1/\zeta^2$, for both sets of data. It is shown that the critical temperature

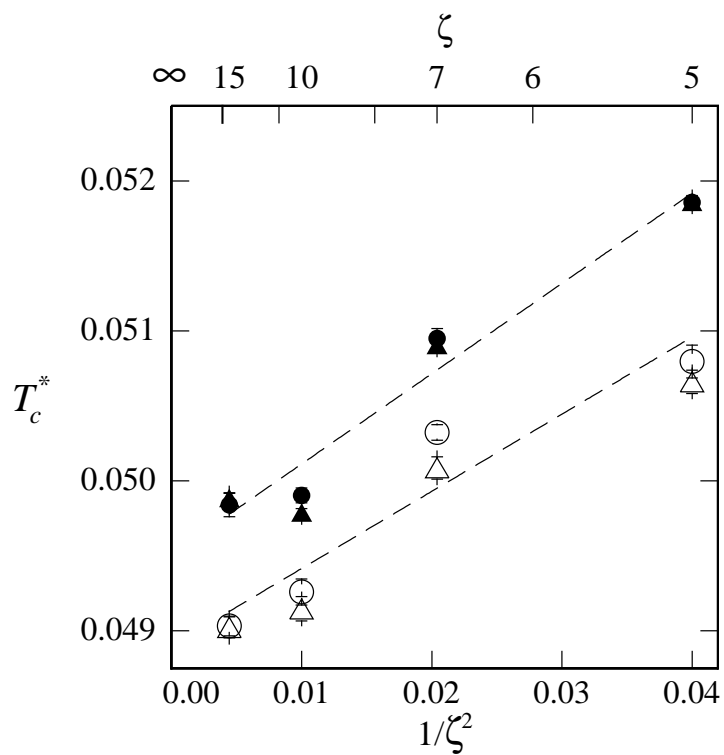


Figure 5.7: Reduced critical temperature, T_c^* , as a function of $1/\zeta^2$ for the “dumb-bell” model with $L^* = 12$, same charge (filled triangles), same dipole (open triangles) and with $L^* = 15$, same charge (filled circles), same dipole (open circles). The dashed line shows the power-law least squares fitting to the data.

values follow almost the same trend as for the restricted primitive model [110], except that some moderate odd-even effect can be observed. We postulate that the distinct number of configurations enforced by fine lattice structure for models with different values of ζ is responsible for this feature. Critical densities decrease on increasing ζ values, with no particular trend. Comparable values for the critical temperature and critical density are available from [111] for $\zeta = 10$ with 318 configurations and reduced bond length, $l^* = l/\sigma$, of 1 – 1.2.

For the trimer case study, as for the dumbbells, the reduced bond lengths ($l^* = l/\sigma$) between the center bead and the side beads were restricted to 1 - 1.2. The angle between the two center-side bonds was fixed to 180° . The center bead carries a positive charge while the side beads carry negative charges. The charge of the center bead is always twice as large as that of the side beads. No intramolecular interaction has been considered within the beads of a single molecule. All the configurations have the same quadrupole moments by having different charges assigned to either of the beads. The critical parameters are summarized in Table 5.4. In accounting for the ζ effect on critical temperatures, no specific trend has been observed within the narrow range of variations compare to the dumbbell model. Likewise the dumbbell model, the odd-even effect has to do with the distinct number of configurations for models with different ζ values. The narrow range of variations for the critical densities precludes us from being able to make a precise judgement about the effect of the lattice discretization parameter on this set of data. The good matching of our data to the Ising-class is an indication but not a proof of Ising-type criticality for the polar models studied.

Table 5.4: Critical parameters for the “dumbbell” and “trimer” models, with identical dipole and quadrupole moments.

Model	L^*	ζ	$-\mu_c$	$-s$	$100T_c^*$	ρ_c^*
dumbbell	12	5	1.3025(3)	0.68(3)	5.07(8)	0.12(1)
		7	1.3245(9)	0.69(4)	5.10(8)	0.11(2)
		10	1.3025(4)	0.69(3)	4.91(8)	0.11(1)
		15	1.2970(4)	0.69(3)	4.90(7)	0.11(1)
	15	5	1.3025(9)	0.69(5)	5.08(9)	0.11(2)
		7	1.3243(4)	0.69(2)	5.03(5)	0.11(1)
		10	1.3024(5)	0.69(4)	4.93(9)	0.11(1)
		15	1.2969(5)	0.69(6)	4.90(6)	0.10(3)
trimer	12	5	3.6362(3)	0.26(1)	2.62(3)	0.07(1)
		7	3.6391(7)	0.26(3)	2.59(4)	0.07(2)
		10	3.6120(5)	0.26(2)	2.66(2)	0.07(1)
	15	5	3.6362(9)	0.26(2)	2.62(4)	0.07(2)
		7	3.6392(9)	0.26(2)	2.59(4)	0.07(1)
		10	3.5589(9)	0.26(0)	2.66(1)	0.07(1)

5.3.3 Non-polar + polar model

The effect of the lattice discretization parameter, ζ , has been considered for this model, in which the potential contains both the short- and long range parts described in previous sections. The short range interactions influence the charge ordering in such a way that the critical temperature is approximately the same as for the dimer model. This model consists of a two-bead chain with one Exp-6 site on each bead and a unit positive and a unit negative charge on each bead as well. All the configurations have reduced bond lengths between 1-1.2. As for the non-polar systems (discussed in Section 5.3.1), the same set of 6 distinct configurations are used for all the systems with different degrees of discretization in order to have the maximum consistency between the systems with different lattice discretization parameters. Fig. 5.8 shows the dependence of the effective reduced critical temperature, T_c^* , on the inverse lattice discretization parameter to the ninth, $1/\zeta^9$, for this model. We interpret the slightly larger value of the exponent compared to the exponents obtained for non-polar models as due to the fact that this model encompasses both short- and long range interactions.

5.4 Conclusions

In this work, we have addressed the issue of how to estimate the effect of the lattice discretization parameter, ζ , on the critical parameters of various model fluids. Specifically, we have considered the Exp-6 soft-core model for non-polar fluids. The data suggest that deviations of the critical temperatures scale as $1/\zeta^{6\pm 1}$ and $1/\zeta^{7\pm 2}$ for monomer and dimer models respectively. The same effect of ζ on critical temperatures for both Exp-6 model of this study and Lennard-Jones [64] model

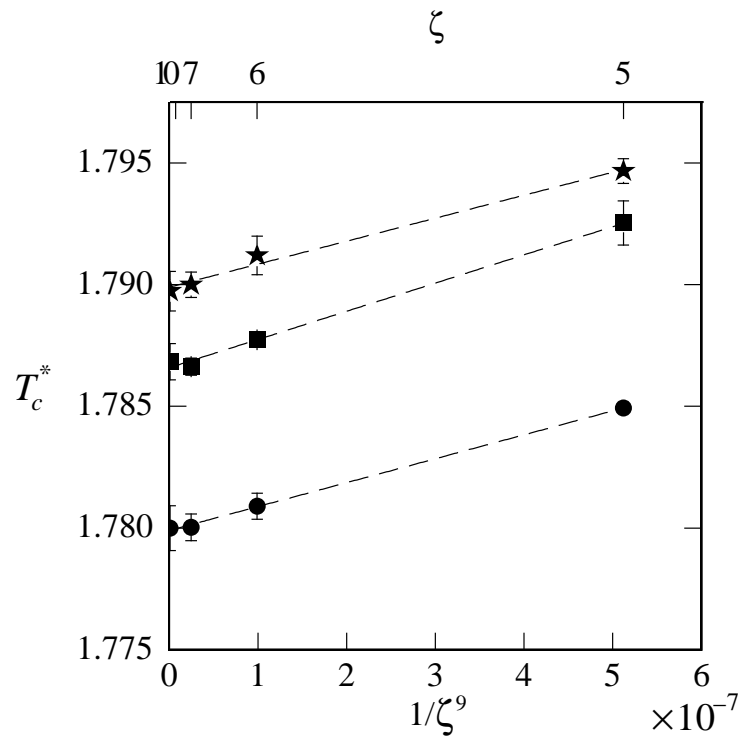


Figure 5.8: Reduced critical temperature, T_c^* , as a function of $1/\zeta^9$ for the “Polar+Exp-6” model with $L^* = 7$ (filled squares), $L^* = 10$ (filled stars), and $L^* = 12$ (filled circles). The dashed line shows the power-law least squares fitting to the data.

of Panagiotopoulos in [3] can be observed for values of $\zeta = 1, 2, 3, 5,$ and 10 . No precise comparison between the two models can be carried out, since only one value of ζ exceeding 5 considered in the earlier study.

Deviations of the critical temperatures are stronger by a factor of 5 for polar models (dipolar dumbbells), compared to the non-polar fluids, and scale as $1/\zeta^{2\pm 0.5}$. The exponent found in the present study for polar fluids is essentially identical to the exponent found for the restricted primitive ionic model [110]. The strong similarities found by Romero-Enrique *et al.* [112] between true ionic fluids and corresponding “tethered dimer” fluids are likely to be responsible for the agreement between the exponents for ionic and polar models.

For the model with both Coulombic and Exp-6 interactions, the critical temperatures scale as $1/\zeta^{9\pm 1}$ for different integer values of ζ . Within the narrow range of critical densities for different values of discretization parameter, no particular trend has been found for the various models studied. The critical density values decrease as the ζ values increase for all the fluids considered in this paper, except the trimer model. The computational cost to estimate precisely the location of the critical density is prohibitively high with the methods of the present work.

Based on these observations, the lattice discretization parameter effect is more pronounced for polar fluids than the non-polar fluids. This is contrary to the intuitive idea that the presence of the lattice influences primarily short range structures. However, the dipole-dipole interactions are dominant forces in the polar fluids (dumbbell model) as found by Romero-Enrique *et al.* [112]. It is possible that the dipole interactions among the neutral clusters at close contact coupled with existing long range forces are sensitive to the degree of lattice discretization. For the quadrupolar interactions (trimer model) the sensitivity is much less. In

the non-polar fluids on the other hand, the interactions are purely driven by homogeneous short range contacts, which are influenced by the lattice discretization to a minor extent. The concept of the repulsive part of the intermolecular potential being responsible for these effects is open to further theoretical investigation.

Chapter 6

Determination of Second Virial Coefficients by Grand Canonical Monte Carlo Simulations¹

6.1 Introduction

The equation of state of a low density gas can be described by the virial expansion. The virial expansion expresses the compressibility factor as a power series in the density, with temperature dependent coefficients known as virial coefficients. The second virial coefficient provides information regarding the intermolecular interactions between a pair of molecules. Similarly the third, fourth, etc. virial coefficients represent deviations from ideal behavior when collisions involving three, four, etc. molecules become important in the gas. Consequently, at low densities, deviations from ideality are adequately described by the second virial coefficient,

¹The results presented in this chapter have also been submitted to Fluid Phase Equilibria.

whereas at higher densities more virial coefficients must be used. The second virial coefficient is an important parameter for determining the thermodynamic properties of the vapor phase and it can be measured experimentally over a large temperature range to within a few percent for many systems. The virial expansion truncated after three terms is [62, 113]:

$$Z = \frac{\beta P}{\rho} = 1 + B_2\rho + B_3\rho^2. \quad (6.1)$$

Z is the compressibility factor, β is the reciprocal temperature $\beta = 1/k_B T$, where k_B is Boltzmann's constant and T is the temperature, P is the pressure, ρ is the density, B_2 is the second virial coefficient, and B_3 is the third virial coefficient. For monatomic particles, the intermolecular potential depends only upon the separation of the two particles and the analytical value for second virial coefficient can be obtained by integrating the orientational and conformational averages of the Mayer f - function corresponding to binary interactions as [62]:

$$B_2 = -\frac{1}{2V} \int \int [e^{-\beta U(\mathbf{r}_{12})} - 1] d\mathbf{r}_1 d\mathbf{r}_2, \quad (6.2)$$

where $U(\mathbf{r}_{12})$ is the intermolecular potential between two particles. As is shown by Eq. 6.2 for spherical monatomic systems, B_2 is simply obtained by the integral calculation over Boltzmann's factor. For more complex systems, such as polyatomic fluids and mixtures, the main difficulty of virial coefficient calculations is the inevitable multidimensional integration which requires intensive computation.

Initially the primary goal was to calculate the second virial coefficient for different model and real fluids and compare them in a very precise way. However, precise calculation of B_2 using GCMC simulations proved to be too complicated. Therefore the main concern in this report is to investigate the possibility of calculating the second virial coefficient using the grand canonical Monte Carlo (GCMC)

ensemble for any system of interest and to examine the range of its accuracy. To the author’s best knowledge, the only previous application of GCMC to calculate the second virial coefficient has been by Errington and Panagiotopoulos for some real fluids [95, 114]. The main motivation for all the cases studied by Errington and Panagiotopoulos was to confirm the credibility of the new intermolecular potential models for the different fluids studied through comparison between their second virial coefficient values and the existing experimental values.

The outline of this chapter is as follows: Section 6.2 is devoted to a brief description of computational methods used to obtain the second virial coefficient. Section 6.3 presents the second virial coefficient values for a variety of model and real fluids. The conclusions are summarized in Section 6.4.

6.2 Methods

We used GCMC simulation for calculating the second virial coefficient. Periodic boundary conditions with minimum image convention are enforced [50, 51]. A new microstate is generated by a mixture of 50% replacement and 50% addition/annihilation with the standard Metropolis acceptance/rejection criteria [48]. The acceptance ratio of the unbiased insertion/removal steps was around 60% at the states with few particles. Microstates with varying values of energy, E , and particle number, N , are sampled throughout the simulation and stored in a two-dimensional histogram $f(N, E; \beta, \mu)$. The histogram $f'(N, E; \beta', \mu')$ for a new state with a different temperature, T' , and chemical potential, μ' , not too far away from state (T, μ) , can be obtained from $f(N, E; \beta, \mu)$ via the simple rescaling:

$$\frac{f'(N, E; \beta', \mu')}{f(N, E; \beta, \mu)} = \exp[-(\beta' - \beta)E + (\beta'\mu' - \beta\mu)N], \quad (6.3)$$

without the need to perform any additional simulations. Properties of interest, such as mean configuration energy, $\langle E \rangle_{\mu,\beta}$, mean number of particles, $\langle N \rangle_{\mu,\beta}$, and mean density, $\langle \rho \rangle_{\mu,\beta}$ can subsequently be obtained in terms of weighted sums or moments of the appropriate histogram, e.g.,

$$\langle X \rangle_{\mu,\beta} = \frac{\sum_{N,E} X f(N, E; \beta, \mu)}{\sum_{N,E} f(N, E; \beta, \mu)}. \quad (6.4)$$

The pressure of a system can be obtained from the following expression. If the conditions for run 1 are (μ_1, V, β_1) and for run 2 (μ_2, V, β_2) then

$$C_2 - C_1 = \ln \frac{\Xi(\mu_2, V, \beta_2)}{\Xi(\mu_1, V, \beta_1)} = \beta_2 P_2 V - \beta_1 P_1 V. \quad (6.5)$$

Eq. 6.5 can be used to obtain the absolute value of the pressure for one of the two runs, provided that the absolute pressure can be estimated for the other run. Typically, this is done by performing simulations for low density states for which the system follows the ideal-gas equation of state, $PV = Nk_B T$. In this sense, the histogram collected is reweighted for a series of chemical potentials to accumulate the $p - \rho - T$ data along the isotherm for which the simulation was run. Through simulations studies, we have investigated that the ideal gas state behavior can be observed for a range of $(10^{-3} - 10^{-2})$ particles which can be obtained using the methodology explained earlier and consequently the pressure can be evaluated with high degree of accuracy. The absolute pressure, density, and temperature are fitted to Eq. 1 with approximately 0.5 and 2 particles as the lower and upper bound of the fitting range, respectively. Surprisingly, we have observed that having a single histogram with a few particles is sufficient for evaluating the second virial coefficient within a few percent. Nevertheless, it is important for the fitted data to have a value of ≥ 0.9999 for their coefficient of determination parameter (R -squared

value) which is defined as:

$$R^2 = 1 - \frac{\sum_i (y_i - \hat{y}_i)^2}{\sum_i (y_i - \bar{y})^2}, \quad (6.6)$$

where y_i , \bar{y} , and \hat{y}_i are the actual sampled data, their mean value, and the predicted values after regression respectively.

In this work, we apply the concept of fine-lattice discretization method [2] for the calculations, where the essence of the method is to perform calculations on a simple cubic lattice of spacing a and particle diameter σ , with pre-computed interactions between all the lattice sites for computational efficiency. A value of $\zeta \geq 10$ has been considered for all the cases studied in this communication. In addition to the pairwise additive intermolecular interactions in the central simulation box, long range corrections according to the method of Theodorou and Suter [83] were applied. Statistical uncertainties were obtained by performing three duplicate sets of runs at identical condition with different seeds for random number generator. The “ran2” routine of Ref. [84], which has a period of 2.3×10^{18} and no low-order serial correlations, was used. A typical run of 10×10^6 Monte Carlo steps in a $5 \times 5 \times 5$ box at the gas state took less than one minute on a Pentium III 1 GHz workstation.

6.3 Results and discussion

We first calculated the second virial coefficient of hard-core model with reduced hard-core diameter of 1 which was found to be within 0.5% of its exact value, $\frac{2\pi}{3}\sigma^3$, where σ is the hard-core diameter. B_2 was also calculated at several temperatures for both Lennard-Jones [64] (abbreviate as “LJ” from this point on) and Exponential-6 Buckingham [68] (abbreviate as “Exp-6” from this point on) models and compared with their analytical values. The analytical values of

second virial coefficient on a lattice can be obtained as:

$$B_2(T; \zeta) = -\frac{1}{2} \left(\sum_{l_x, l_y, l_z} [e^{-\beta U(l_x, l_y, l_z)} - 1] \right) \times \lambda^3. \quad (6.7)$$

The conventional distance spacing, r , for the continuous potential model is replaced by la where indexes (l_x, l_y, l_z) label the successive lattice sites in space and λ is the lattice spacing. We summarize the reduced second virial coefficient, $B_2^* = B_2/(2\pi\sigma^3/3)$, for two model fluids studied at various reduced temperature, $T^* = k_B T/\epsilon$, where ϵ is the well depth of the potential and σ is the characteristic size parameter for which potential is zero, in Table 6.1, where numbers in parentheses indicate statistical uncertainties in units of the last digit of the corresponding value. As is shown the second virial coefficient values are systematically slightly smaller than the analytical value but most of them are within the statistical uncertainties. With a numerical example we will show why it is almost impossible to obtain more precise results for the second virial coefficient using grand canonical Monte Carlo simulations. The results of two simulations performed under identical conditions with two different seeds show that although the partition functions and number of particles (the only two independent degrees of freedom) are the same with less than 0.5 percent deviation, the second virial coefficient results are different by around 10 percent which obviously conveys that the possibility of having a few percent deviation for B_2 is impossible. We believe that statistical noise is the reason for this behavior. To avoid the possibility of adding to the statistical noise due to the insufficient sampling, the Monte Carlo steps were progressively lengthened until the calculated values for B_2 became stable. Each process was completed with 10×10^9 Monte Carlo steps. But even for every long run, we get systematic deviations from analytical value.

Two polyatomic models are also considered for this study, ethane and propane.

Table 6.1: Reduced second virial coefficient, calculated analytically and by simulation for both “LJ” and “Exp-6” models with $L^* = 5$.

Model	T^*	$B_2^*(\text{simulation})$	$B_2^*(\text{analytical})$
LJ	1.0	-2.57(3)	-2.54
	1.2	-1.86(3)	-1.84
	1.4	-1.40(4)	-1.38
	1.6	-1.07(2)	-1.05
	1.8	-0.83(3)	-0.81
	2.0	-0.63(1)	-0.63
Exp-6	1.0	-2.46(2)	-2.40
	1.2	-1.77(4)	-1.73
	1.4	-1.34(5)	-1.29
	1.6	-1.03(4)	-0.98
	1.8	-0.79(4)	-0.75
	2.0	-0.59(1)	-0.58

A united-atom description of the molecules for both models has been considered. The nonbonded interactions between groups on different molecules are described by “LJ” potential. The potential parameters are taken from Vega *et al.* [115] with $\epsilon_{\text{CH}_3-\text{CH}_3}/k_{\text{B}} = 104$, $\epsilon_{\text{CH}_2-\text{CH}_2}/k_{\text{B}} = 49.7$ (in K), and $\sigma_{\text{CH}_3-\text{CH}_3} = \sigma_{\text{CH}_2-\text{CH}_2} = 3.923$ Å. In their work, methyl and methylene groups have been modelled as “LJ” interaction sites equal in size but differing in energy well depth to reproduce experimental values of second virial coefficients of a number of *n*-alkanes in a broad range of temperatures. It should be noted that these parameters have been optimized for *n*-alkanes between four and sixteen number of carbons and the energetic interaction between pairs of -CH₂ or -CH₃ groups systematically decreases for molecules of increasing lengths, perhaps as a consequence of a partial screening of the bare site-site interactions by the surrounding groups [116]. Nevertheless we have constructed our models with these parameters optimized for *n*-alkane with four carbon numbers and it may be a source for some deviations between the calculated second virial coefficient values and their experimental data. The values of the “LJ” interactions between chemically different groups are obtained from the Lorentz-Berthelot combining rules.

All possible orientations for both ethane and propane models were generated at the beginning of the simulation, stored in a reservoir, and once the simulation got started, a random configuration was selected from the reservoir to be added to the system. The CH₃-CH₃ and CH₃-CH₂ bond lengths were restricted to remain between 1.7-1.9Å and 1.64-1.72Å for the ethane and propane models, respectively, and the bond bending angle was set to remain between 178-180° for the propane model [4]. The second virial coefficients of ethane and propane are displayed in Figs. 6.1 and 6.2. The results show that the new method can be used to reli-

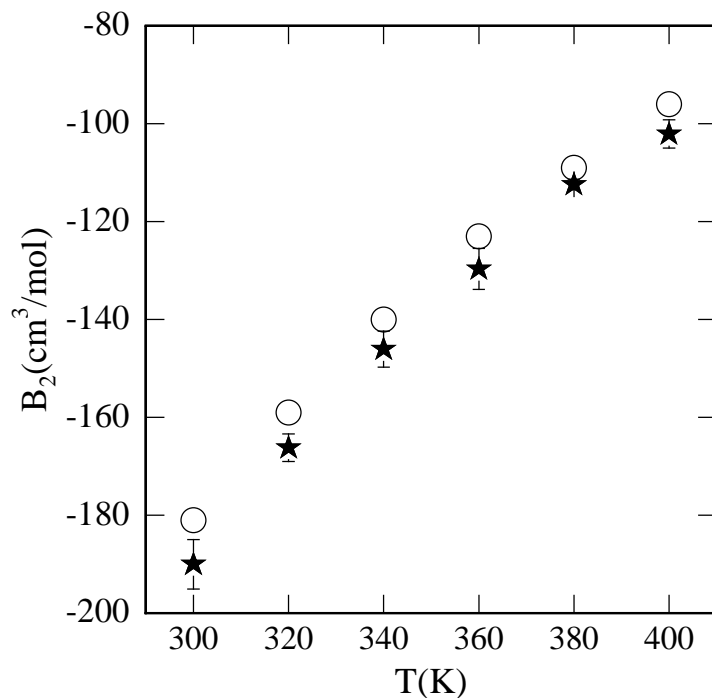


Figure 6.1: Second virial coefficient for ethane, B_2 , as a function of temperature, T . The stars represent calculations for the “ethane” model using GCMC with $L^* = 5$ and circles represent the experimental data [8].

ably predict the second virial coefficient within few percent over a large range of temperatures. The propane model is in better agreement with the experimental data than the ethane model. This is not surprising, given the fact that energetic interactions values chosen for the propane model should be more precise considering the fact that the optimized values for butane have been chosen from Vega *et al.*[115].

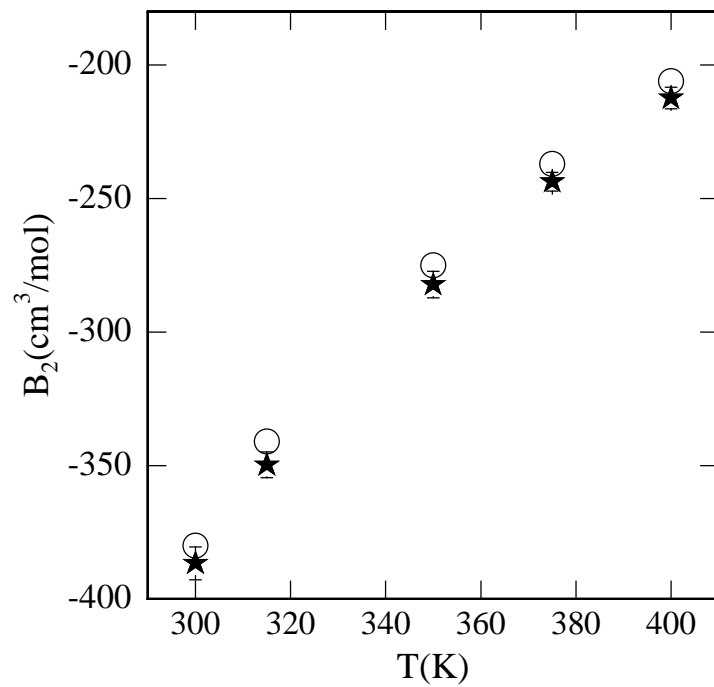


Figure 6.2: Second virial coefficient for propane, B_2 , as a function of temperature, T . The stars represent calculations for the “propane” model using GCMC with $L^* = 5$ and circles represent the experimental data [8].

6.4 Conclusions

In summary, a simple and effective prescription to calculate the second virial coefficient, $B_2(T)$, using grand canonical Monte Carlo method has been provided. Second virial coefficient for a various model and real fluids were also determined and comparisons were made with the analytical and experimental values, respectively. In general, the method was able to produce the second virial coefficient to within an accuracy of a few percent.

Chapter 7

Theory of Fine-lattice

Discretization for Near Critical Fluids

7.1 Introduction

In this chapter, we present the results of a theoretical study of fine-lattice discretization concept near the critical region. This work was conducted under the supervision of Professor Michael E. Fisher and some extensions of it are still in progress.

The study was motivated by recent simulations by Panagiotopoulos [110] on a simple cubic lattice for the electrolyte model known as the restricted primitive model (RPM). Both the critical temperature and the critical density were found to decrease on increasing the lattice discretization parameter, ζ . The deviations of the critical parameters from the continuum values ($\zeta \rightarrow \infty$) were found to scale approximately as $1/\zeta^2$. Our goal here is to understand theoretically this

relationship and also to see the effects of the lattice discretization parameter, ζ , on critical parameters for a variety of other fluid models. A schematic view of a two-dimensional hard-core model is shown in Fig. 2.2, where the cell size is represented by λ . The full circle represents the particle diameter, σ , and the dashed line circle encloses the excluded points. The ratio σ/λ is defined as the lattice discretization parameter ζ ; this basically controls how closely the lattice system approaches the continuum limit. In order to be consistent with previous work on this subject [117], from now on we denote the lattice spacing by a (previously by λ) and the hard-core diameter by b (previously by σ).

The notion of lattice spacing, a , is introduced as the ratio of the hard-core [110] or soft-core [66] diameter to the lattice discretization parameter. Here, we use n as the lattice discretization parameter, when it only takes integer values, whereas the ζ notation will be used when the lattice discretization parameter can take any positive real value. It will be shown how the new definition of a as a non-integral fraction of the hard-core diameter, b , can improve the convergence of the critical parameters in the lattice environment to their continuum values. The aim is to propose new methods for improving the rate of convergence of the critical parameters evaluated on lattices to their continuum counterparts.

We present the theoretical framework of our calculations in Section. 7.2 and describe its practical implementation in one-dimensional space $d = 1$ for hard-core and a variety of other potential models in Section 7.3. Section 7.4 is devoted to a brief description of the van der Waals (abbreviated as VdW from this point on) method for calculating critical parameters in $d \geq 2$ dimensional space and some background about the theory of the number of lattice points inside a circle or sphere defining the hard-core. The dependence of the second virial coefficient on

the lattice discretization parameter for both hard-core and a soft-core potentials is discussed in the last section.

7.2 Theoretical background

In this section a theoretical formulation following the work of Fisher *et al.* [117] for the effect of lattice discretization parameter, n , on critical parameters is presented. We will consider a linear one-dimensional system ($d = 1$) of length L . If $\Xi(\beta, z; L)$ is the grand canonical partition function of the system at temperature $T = 1/k_B\beta$, with k_B being the Boltzmann's constant, and at activity z , that is normalized so as to approach the density as $z \rightarrow 0$ at fixed T , then the partition function can be defined as

$$\Xi(\beta, z; L) = \beta p L, \quad (7.1)$$

where p is the appropriate one-dimensional pressure. It is more effective to calculate the thermodynamic properties of the system by investigating the Laplace transform of Ξ shown as

$$\Psi(\beta, z; s) = \int_0^\infty e^{-sL} \Xi(\beta, z; L) dL. \quad (7.2)$$

This integral is absolutely convergent for all values of s with a real part exceeding the abscissa of convergence, s_0 , defined as [117]

$$s_0 = s_0(\beta, z). \quad (7.3)$$

As s approaches s_0 from above along the real axis, $\Psi(\beta, z; s)$ diverges to infinity as a simple pole [118]. All the thermodynamic properties can be obtained by solving the equation

$$\beta p = s_0(\beta, z). \quad (7.4)$$

For the discretized lattice model the partition function is defined as

$$\Xi(\beta, z; L) = \sum_{N=0}^{\infty} \sum_{E_N} e^{-\beta E_N + \beta \mu N} \quad (7.5)$$

or equivalently

$$\Xi(\beta, z; L) = \sum_{N=0}^{\infty} e^{\beta \mu N} \sum_{l_1=1}^L e^{-\beta \varphi_{l_1}} \sum_{l_2=1}^{L-l_1} e^{-\beta \varphi_{l_2}} \dots \sum_{l_{N-1}=1}^{L-(l_1+l_2+\dots+l_{N-2})} e^{-\beta \varphi_{l_{N-1}}}, \quad (7.6)$$

where a is the lattice spacing and the index l labels the successive occupied lattice sites as l_1, l_2, \dots, l_{N-1} , while $\varphi_l = \varphi(la)$ (with $l = 0, 1, 2, \dots$), denotes the values of the potential function on discretized sites. Assuming that the first particle is fixed at the origin and that each particle interacts only with its nearest neighbor, we can introduce the generating function

$$\Psi(\beta, z; s) = \sum_{N=1}^{\infty} z^N [\mathcal{L}\{e^{-\beta \varphi_l}\}]^{N-1} = z \sum_{N=1}^{\infty} [zJ(s)]^{N-1}, \quad (7.7)$$

where the Laplace transform of the Boltzmann factor associated with the potential φ_l is

$$J(s) = \sum_{l=0}^{\infty} e^{-las} \exp(-\beta \varphi_l) \quad ; \quad l = 0, 1, 2, \dots, n, n+1, \dots \quad (7.8)$$

It can be concluded that

$$\Psi(\beta, z; s) = \frac{z}{1 - zJ(s)}, \quad (7.9)$$

where the activity is

$$z = \exp(\beta \mu). \quad (7.10)$$

The abscissa of convergence, s_0 , is evidently determined by the solution of the equation

$$zJ(s) = 1 \quad (7.11)$$

and consequently [119–123] we have

$$J(\beta p) = \frac{1}{z} \quad (7.12)$$

and

$$J'(\beta p) = -\frac{1}{\rho z}, \quad (7.13)$$

where ρ is the mean number of particles per unit length. The present one-dimensional model does not, of course, exhibit any phase transition, but by considering the corresponding van der Waals limit [124, 125], the equation of state can be expressed as

$$p = p_0(\rho, T) - \bar{\epsilon} b \rho^2, \quad (7.14)$$

where p_0 is the pressure as a function of ρ and T for the model with only hard-core interaction, while the second part $\bar{\epsilon} b \rho^2$ (equivalent to the van der Waals “ a ”) is chosen so as to match the exact high-temperature behavior of the second virial coefficient which results when the attractive interactions are included. The equation of van der Waals was the first successful attempt to formulate an equation of state exhibiting a critical point. This equation is presently viewed as one of a large class of equations of state that are called “classical” or “mean-field” equations, and although it fails to describe the behavior of real fluids with any degree of accuracy over most of the thermodynamic surface, it nonetheless exhibits some important features of real fluids like vapor-liquid condensation and the presence of a critical point.

7.3 The one-dimensional models

7.3.1 Hard-core model

The hard-core potential abbreviated as “HC” is defined as

$$\varphi_l = \begin{cases} \infty & \text{if } l a < b \\ 0 & \text{if } l a \geq b \end{cases} \quad (7.15)$$

where b is the hard-core diameter or equivalently hard-rod length. The conventional distance spacing, r , for a continuous potential is replaced by la where the index l labels the successive lattice sites and a is the lattice spacing. The lattice spacing, a , is defined as $a = \frac{b}{n}$ where n is an integer value. As our goal is to extend the definition of a in later studies, we use the notation b_0 for the hard-core diameter of the potential, when it is an exact integer factor of the lattice spacing as

$$b_0 = an. \quad (7.16)$$

The p_0 in Eq. 7.14 is found to be

$$p_0 = \frac{k_B T}{a} \ln \left(\frac{1 - (n-1)a\rho}{1 - an\rho} \right). \quad (7.17)$$

One of the common features of the van der Waals equation of state is that it assumes an analytical dependence of the pressure (or the Helmholtz free energy) on temperature and volume, while the critical points are characterized by conditions $\left(\frac{\partial p}{\partial \rho}\right)_T = 0$, $\left(\frac{\partial^2 p}{\partial \rho^2}\right)_T = 0$, and $\left(\frac{\partial^3 p}{\partial \rho^3}\right) \neq 0$. Therefore we find

$$b_0 \rho_c = \frac{(2n-1) - (n^2 - n + 1)^{\frac{1}{2}}}{3(n-1)} \quad (7.18)$$

and

$$\frac{k_B T_c}{\epsilon} = 2b_0 \rho_c (1 - b_0 \rho_c) \left(1 - b_0 \rho_c + \frac{b_0 \rho_c}{n}\right). \quad (7.19)$$

In the continuum limit when $n \rightarrow \infty$, one obtains $b_0 \rho_c \rightarrow \frac{1}{3}$ and $\frac{k_B T_c}{\epsilon} \rightarrow \frac{8}{27}$.

If we represent the asymptotic behavior of the deviation of the critical density and the critical temperature from their continuum limits as Δ_n , we can assume in general that

$$\Delta_n \approx \frac{A}{n^\psi} [1 + \dots], \quad (7.20)$$

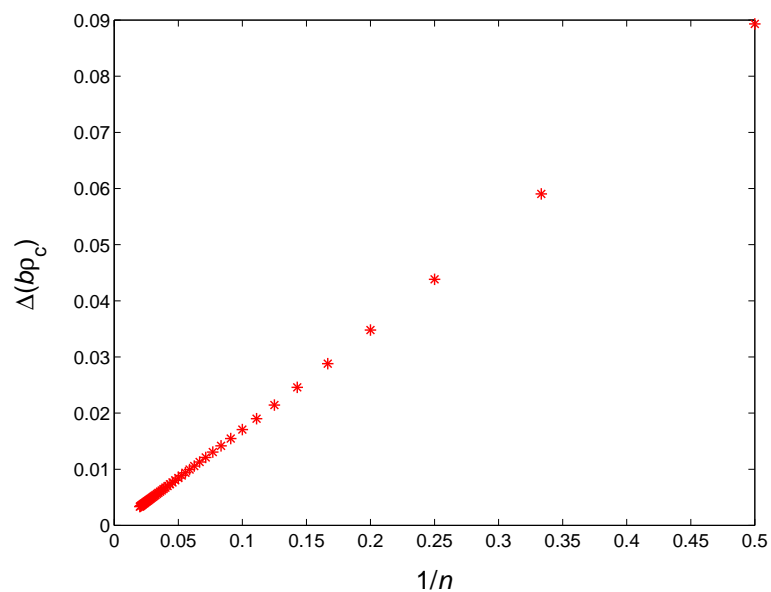


Figure 7.1: Reduced critical density as a function of $1/n$ for HC Model.

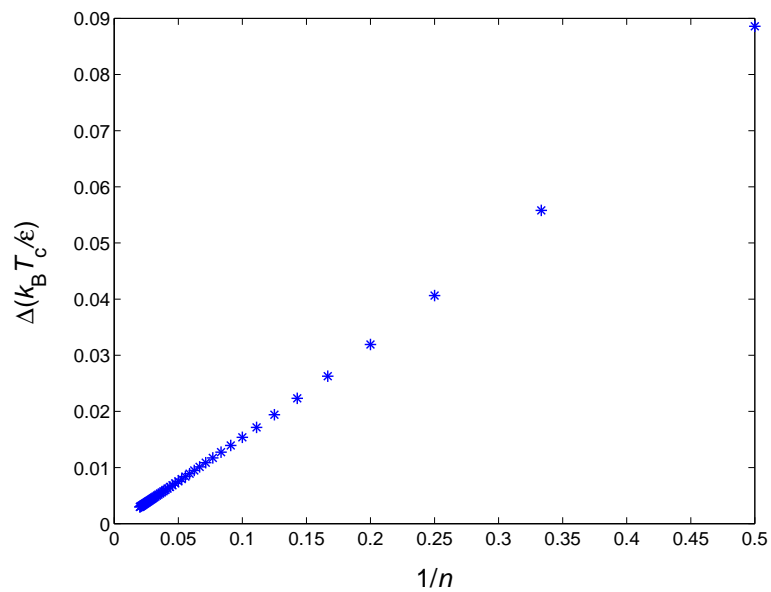


Figure 7.2: Reduced critical temperature as a function of $1/n$ for HC Model.

where ψ is an exponent we wish to know. The asymptotic behavior of the critical density, the critical temperature, and the critical pressure are found from

$$\Delta(b_0\rho_c) = b_0\rho_c^{(n)} - b_0\rho_c^{(\infty)} = \frac{1}{6n}\left(1 + \frac{1}{4n} + \frac{1}{4n^2} + \dots\right), \quad (7.21)$$

$$\Delta\left(\frac{k_{\text{B}}T_c}{\epsilon}\right) = \frac{k_{\text{B}}T_c^{(n)}}{\epsilon} - \frac{k_{\text{B}}T_c^{(\infty)}}{\epsilon} = \frac{4}{27n}\left(1 + \frac{3}{8n} + \dots\right), \quad (7.22)$$

and

$$\Delta\left(\frac{b_0p_c}{\epsilon}\right) = \frac{1}{n}\left(1 + \frac{1}{4n} + \dots\right). \quad (7.23)$$

Figs. 7.1 and 7.2 show the dependence of the critical density and the critical temperature on the inverse lattice discretization parameter. Both the critical temperature and the critical density decrease hyperbolically with increasing n .

7.3.2 New approach for choosing the lattice spacing in hard-core model

To understand properly the nature of the lattice discretization effect, one must go beyond the common definition of lattice spacing and introduce new definitions for both lattice spacing and critical parameters and possible new approaches for evaluating them. Here, we extend the choice of lattice spacing, a , from only integer fractions of the hard-core diameter, b , to arbitrary non-integer (≥ 1) fractions. This is equivalent to allowing the value of ζ defined as $\zeta = \frac{b}{a}$ to take arbitrary positive real values. Our main motivation for this extension is the observation that the values of the potential function φ_l on the lattice sites are insensitive to the choice of ζ for $\zeta \in (n-1, n]$, $n = 1, 2, 3, \dots$. This property is illustrated in Fig. 7.3. The question is whether any particular choice of ζ in the interval $(n-1, n]$ will result

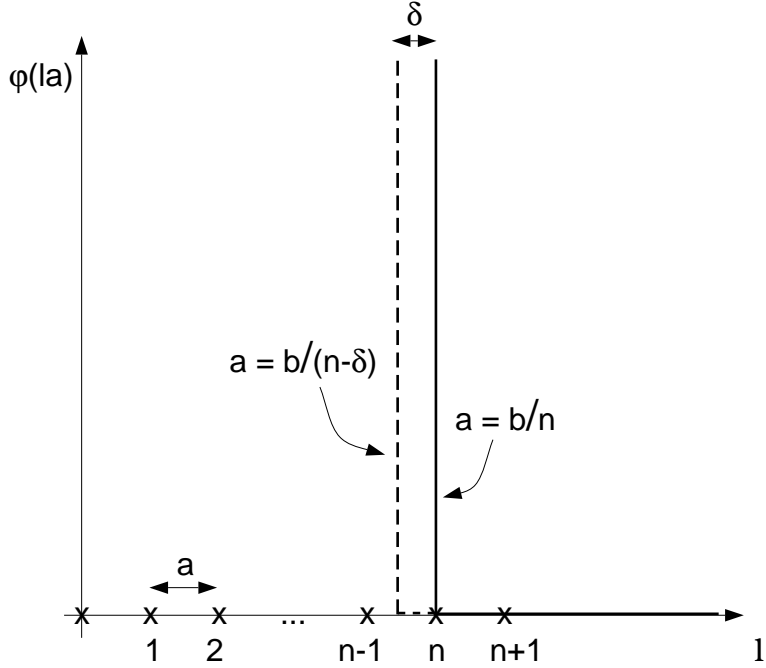


Figure 7.3: The insensitivity of the discretized potential function to the value of δ .

in a faster convergence of critical parameters to their continuum counterparts. For this purpose, from now on, we represent ζ as $\zeta = n - \delta$ with $0 \leq \delta < 1$ and try to obtain the optimum value of δ . In the following, we will answer the above question for the HC potential via two different approaches.

First approach:

In this part, we will prove that by matching the second virial coefficient, B_2 , in both continuum and lattice spaces, we can improve the convergence of the critical density and the critical temperature in lattice space to their continuum counterparts. From Eq. 7.17, we conclude that the hard-core part of the van der Waals equation in lattice space is:

$$\beta p_0 = \rho + \left(1 - \frac{1}{2n}\right) b_0 \rho^2 + \dots, \quad (7.24)$$

and in continuum-space we have

$$\beta p_0 = \frac{\rho}{1 - \rho b} = \rho + b\rho^2 + b^2\rho^3 + \dots, \quad (7.25)$$

where $B_2 = b$ and the third virial coefficient $B_3 = b^2$. Matching the second virial coefficient in both spaces, we can conclude that

$$a = \frac{b}{n - 1/2}. \quad (7.26)$$

Now by considering the new definition for lattice spacing, a , we have

$$\Delta(b_0\rho_c) = b_0\rho_c^{(n)} - b_0\rho_c^{(\infty)} = \frac{1}{8n^2} \left[-1 + \mathcal{O}\left(\frac{1}{n}\right) + \dots \right]. \quad (7.27)$$

Comparing Eq. 7.27 with its counterparts for $a = \frac{b}{n}$, it is clear that the $1/n^2$ factor implies an improvement over in the rate of the convergence for the critical density compared to the original definition of a simply as b/n . According to our definition of $\zeta = \frac{b}{a}$ in previous chapters, this result suggests that the sequence of systems with $\zeta^{(n)} = n - 1/2$ results in a faster convergence to the continuum values.

Second approach:

Let us define:

$$\rho_c^\dagger(n) = an\rho_c^{(n)} = b_0\rho_c^{(n)} \quad (7.28)$$

to be the critical density of the case with $b = b_0 = an$ and

$$\rho_c^*(\zeta) = b\rho_c(\zeta) \quad (7.29)$$

the critical density of the case with $b = a(n - \delta)$. Since the critical density only depends on the potential function and, as stated earlier, the φ_l values are the same for both cases, we can write

$$\rho_c^*(\zeta) = b\rho_c^{(n)} = \frac{\zeta}{n}\rho_c^\dagger(n). \quad (7.30)$$

Using Eq. 7.18 then

$$\rho_c^*(\zeta) = \frac{\zeta}{2n - 1 + \sqrt{n^2 - n + 1}}, \quad (7.31)$$

which, after a few steps, can be written as

$$\rho_c^*(\zeta) = \frac{1}{3} \frac{\zeta}{n - \frac{1}{2} + \frac{C}{n} + \mathcal{O}(\frac{1}{n^2})}, \quad (7.32)$$

where C is a constant. Finally, setting $\zeta = n - \delta$ gives

$$\rho_c^*(\zeta) = \frac{1}{3} \left[1 + \left(\frac{1}{2} - \delta \right) \frac{1}{n} + \frac{\tilde{c}(n)}{n^2} + \dots \right]. \quad (7.33)$$

Eq. 7.33 clearly shows that the optimal value of δ that cancels the $1/n$ term is $\delta = 1/2$ and with this choice, $\rho_c^*(\zeta)$ approaches the continuum value with $1/n^2$ speed. This result obviously is in agreement with what was given by the first approach.

7.3.3 Square-well model

Here, we assume that φ_l is a general square-well abbreviated as “SW” potential of depth $\epsilon \geq 0$ with b the diameter of the hard-core and $[b-c)$ the width of the well, so that

$$\varphi_l = \begin{cases} \infty & \text{if } la < b \\ -\epsilon & \text{if } b \leq la < c \\ 0 & \text{if } la \geq c. \end{cases} \quad (7.34)$$

As before, the conventional distance spacing, r , for continuous potential is replaced by la , where the index l labels the successive lattice sites and a is the lattice spacing. The function $J(s)$ given by Eq. 7.8 is then readily evaluated and the $\rho(\beta, s)$ can be obtained as a consequence. The spinodals can now be obtained from the conditions

$$\beta p = s(\rho; \beta) - \epsilon \beta \rho^2 \quad (7.35)$$

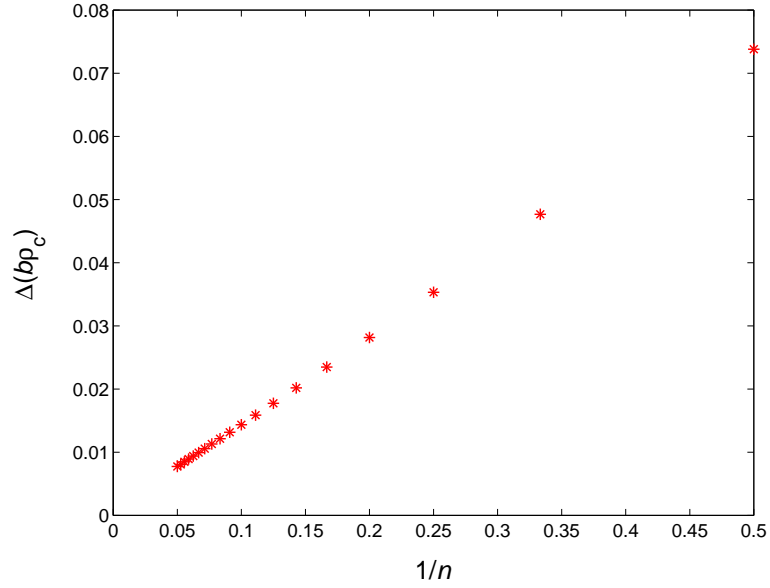


Figure 7.4: Reduced critical density as a function of $1/n$ for SW Model.

and

$$Y(\rho, T) = \frac{\partial(\beta p)}{\partial(\rho)} = s'(\rho\beta) - \epsilon\beta\rho \quad (7.36)$$

and consequently the critical temperature and critical density can be obtained. Figs. 7.4 and 7.5 show the critical density and the critical temperature versus $1/n$. We find that the critical parameters decrease linearly upon increasing $1/n$.

7.3.4 New approach for choosing the lattice spacing in square-well model

Let the lattice spacing be defined as:

$$a = \frac{b}{n - \delta}, \quad (7.37)$$

where b , n , and δ are the hard-core diameter, lattice discretization parameter, and an arbitrary optimization parameter, respectively. Obviously this is a discretized

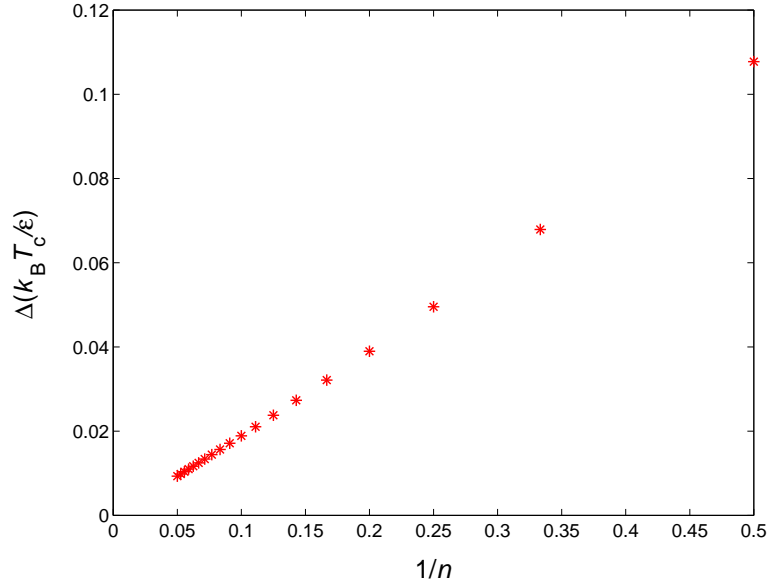


Figure 7.5: Reduced critical temperature as a function of $1/n$ for SW Model.

system with $\zeta = n - \delta = b/a$. For potentials for which their second virial coefficients are temperature dependent, we can match the second virial coefficient of the lattice and continuum models at the critical temperature and find the optimum value for δ by numerically solving

$$B_2^\infty(T_c) + b\beta_c^\infty \epsilon = B_2^n(T_c; \delta) + b\beta_c^n \epsilon, \quad (7.38)$$

where

$$B_2^\infty(T_c) = -\frac{1}{2} \int [\exp(-\beta_c \varphi(r)) - 1] dr \quad (7.39)$$

is the second virial coefficient in continuum-space at the critical temperature and

$$B_2^n(T_c; \delta) = -\frac{1}{2} \sum_{l=-\infty}^{l=+\infty} [\exp(\beta_c \varphi_l) - 1] a \quad (7.40)$$

is the second virial coefficient in lattice space. We hope that, as for the hard-core model, this choice of δ results in a faster convergence of critical parameters. We postulate that the value of δ might be n dependent and may vary for different

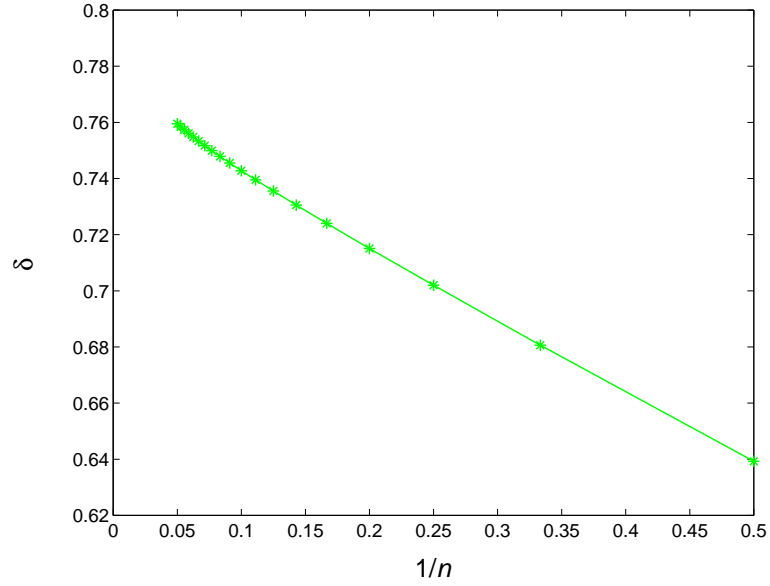


Figure 7.6: Optimization factor δ as a function of $1/n$ for SW model.

potentials. Fig. 7.6 shows the resulting values of δ for each n . In order to investigate the effect of δ on critical density, we redefine density, ρ , as the average number of particles per hypercubes of side a ; that is $\rho \propto \langle N \rangle / a^d$, then

$$\frac{\rho}{\rho_0} \approx \frac{(\frac{b}{n})^d}{(\frac{b}{n-\delta})^d} \quad (7.41)$$

and subsequently

$$\rho \approx (1 - \frac{\delta}{n})^d \rho_0 = \lambda_L^d \rho_0 = \lambda_\rho \rho_0 \quad (7.42)$$

where

$$\rho_0 = \text{density with } a_0 = \frac{b}{n} \quad (7.43)$$

and

$$\rho = \text{rescaled density with } a = \frac{b}{n-\delta}. \quad (7.44)$$

Here, λ_ρ serves as a length scale factor and we hope that the new scaled density converges to its continuum value faster than the original density. We can also consider rescaling the temperature or $\beta = 1/k_B T$ by matching the T -derivatives as:

$$\frac{\partial B_2^\infty}{\partial T}(T = T_c) = \frac{\partial B_2^n(\lambda_T T_c; \delta)}{\partial T} \quad (7.45)$$

in order to have a faster convergence of the critical temperature. Unfortunately, our initial results did not confirm our expectations and the rescaled quantities converged at almost the same rate as the original data. This problem needs further investigation and is the subject of our ongoing research. In the remaining subsections, the smoothness of the repulsive part of the interaction is varied in order to investigate that effect on the convergence rate of the critical parameters to their continuum values in systems with integer values of lattice discretization parameter. The same concept of defining a real positive lattice discretization parameter can be applied to all the models studied in the following sections ($d = 1$) and in order to find the optimal values for density and temperature scaling factors.

7.3.5 Logarithmic hard-core model

The potential model abbreviated as “LGHC” is defined as:

$$\varphi_l = \begin{cases} \infty & \text{if } la < b \\ \epsilon \ln\left(\frac{1}{la - b}\right) & \text{if } b \leq la < c \\ 0 & \text{if } la \geq c \end{cases} \quad (7.46)$$

As before, the conventional distance spacing, r , for continuous potential is replaced by la where index l labels the successive lattice sites and a is the lattice spacing. Fig. 7.7 shows the typical shapes of the Boltzmann factor ($\exp(\beta\varphi_l)$) for this potential function for different values of $\beta\epsilon$. The interaction potential is taken to

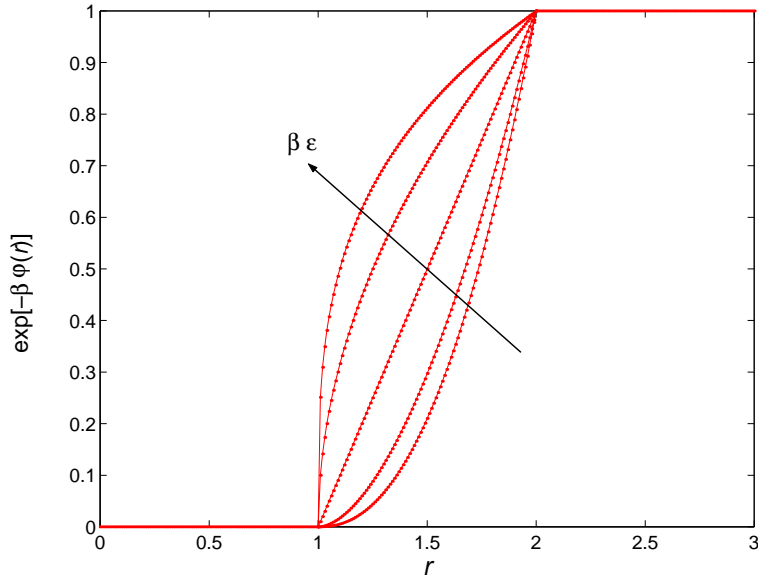


Figure 7.7: Boltzmann factor with different values of $\beta\epsilon$.

be made up of a hard-core part where b is the hard-core diameter and a smooth repulsive part defined in the $[b,c]$ area. Compared to the previous models, the change of the shape of the potential function in the $[b-c]$ area is responsible for the smoothness of the repulsive interaction of the potential model. Similar to the SW model, the critical temperature and critical density can be obtained numerically through Eqs. 7.8, 7.35 and 7.36. In the first set of calculations, the results have been obtained by assuming no temperature effect ($\beta\epsilon = 1$) on the potential by using the following format for Eq. 7.8 with $b = na$ and $c = 2b$.

$$J(s) = \sum_{l=n}^{l=2n-1} (la - b)e^{-las} + \sum_{l=2n}^{\infty} e^{-las}. \quad (7.47)$$

In the second set of calculations, some temperature effects are taken into consideration by setting $\beta\epsilon = \frac{1}{2}\beta_c\epsilon$ where β_c is the corresponding critical temperature

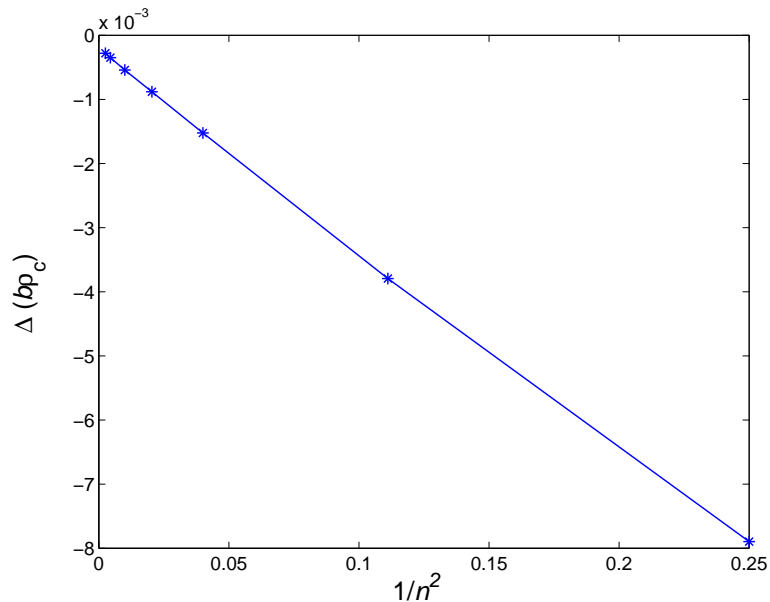


Figure 7.8: Reduced critical density as a function of $1/n^2$ for LGHC model with no temperature effect.

obtained from the first set of calculations. In this case Eq. 7.8 becomes

$$J(s) = \sum_{l=n}^{l=2n-1} (la - b)^{\beta\epsilon} e^{-las} + \sum_{l=2n}^{\infty} e^{-las}. \quad (7.48)$$

For simplicity, a value of $\epsilon = 1$ has been considered for all calculations. Figs. 7.8 and 7.9 show the critical density and the critical temperature for different values of n for the first set of calculations. Both critical temperature and critical density increase upon increasing n for the first set of calculations. Whereas for the second set of calculations where we consider some temperature effect for the potential, both critical temperature and critical density decrease on increasing the lattice discretization parameter, n . The data are shown in Figs 7.10 and 7.11. Nonetheless, in both cases the deviations of the critical parameters scale as $1/n^2$ which is indicative of a faster convergence for this family of potential functions. The discrepancy between these results and the results for the hard-core model might

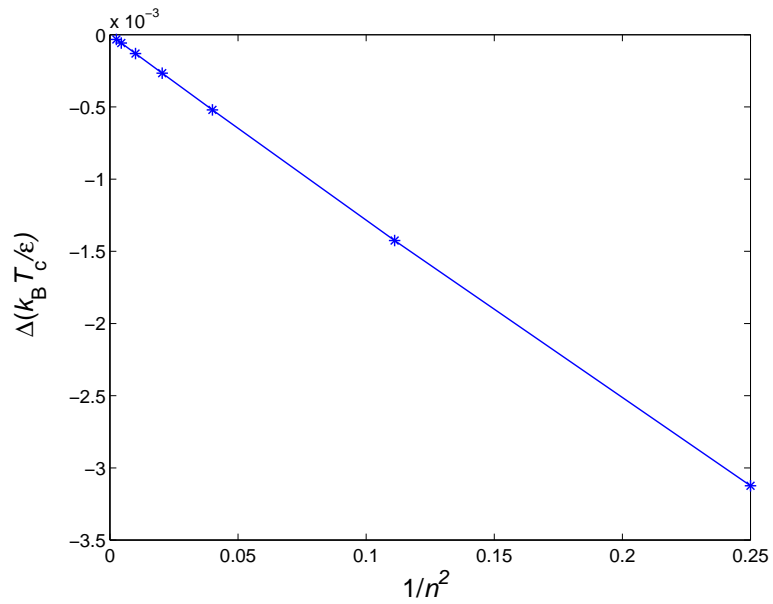


Figure 7.9: Reduced critical temperature as a function of $1/n^2$ for LGHC model with no temperature effect.

be due to the abrupt jump in the Mayer function, $1 - e^{-\beta\phi(r)}$, present in the latter model.

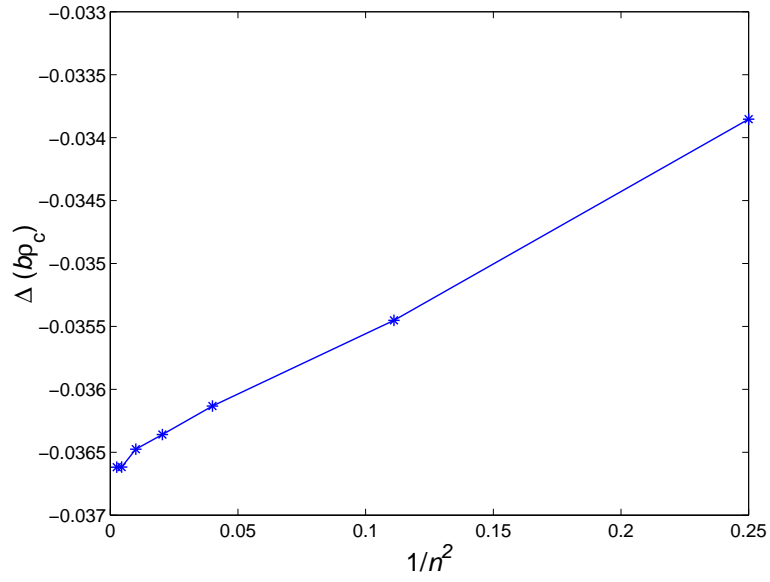


Figure 7.10: Reduced critical density as a function of $1/n^2$ for LGHC model with some temperature effect.

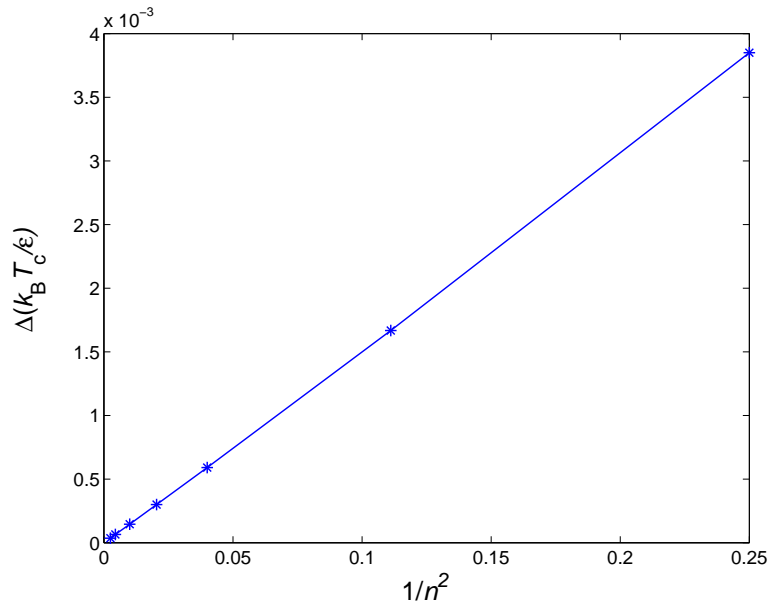


Figure 7.11: Reduced critical temperature as a function of $1/n^2$ for LGHC model with some temperature effect.

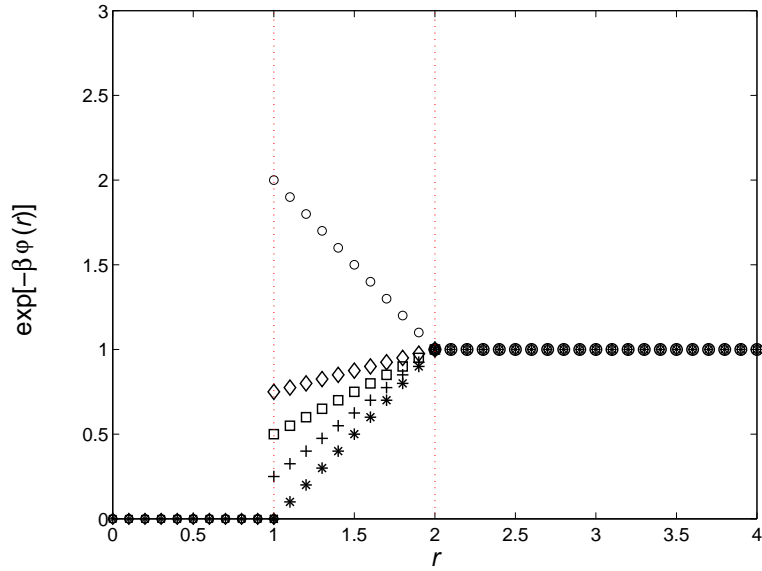


Figure 7.12: Different logarithmic potential models with $y_0 = 0.0$ (stars), $y_0 = 0.25$ (crosses), $y_0 = 0.5$ (open squares), $y_0 = 0.75$ (open diamonds), and $y_0 = 2.0$ (open circles).

7.3.6 Logarithmic hard-core model with a jump

The potential abbreviated as LGHCj model is defined as:

$$\varphi_l = \begin{cases} \infty & \text{if } la < b \\ -\epsilon \ln[(1 - y_0)(la - b) + y_0] & \text{if } b \leq la < c \\ 0 & \text{if } la \geq c \end{cases} \quad (7.49)$$

As before, the conventional distance spacing, r , for continuous potential is replaced by la where the index l labels the successive lattice sites and a is the lattice spacing. As in the case of the LGHC model, the potential implies a hard-core with diameter b and a repulsive well in the $[b-c)$ interval. As shown in Fig. 7.12, the repulsive part of the function starts to decay at some arbitrary value y_0 , whereas for the LGHC model the repulsive part starts to decay right at the hard-core.

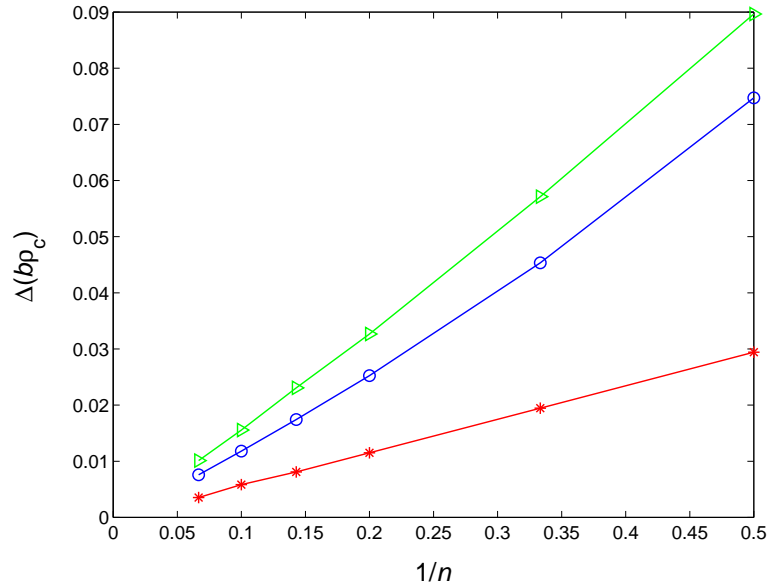


Figure 7.13: Reduced critical density as a function of $1/n$ for LGHCj Model with no temperature effect with $y_0 = 0.25$ (open stars), $y_0 = 0.5$ (open circles) and $y_0 = 0.75$ (right triangles).

In Figs. 7.13 and 7.14, we show the critical density and critical temperature for different LGHCj models with no temperature effect. As can be seen, the critical parameters decrease on increasing $1/n$ values almost linearly. The critical density and critical temperature for different LGHCj models for the second set of calculations are shown in Figs. 7.15 and 7.16, where there exists some temperature effect. For the $y_0 = 2.0$ case, as shown, the critical parameters decrease on increasing $1/n$ value linearly for both sets of calculations as shown in Figs. 7.17, 7.18, 7.19, and 7.20.

We may conclude that it is the presence of the finite jump in the Boltzmann factor $\exp[-\beta\varphi(r)]$, or, equivalently, in the Mayer factor, that leads to the slower, $1/n$ decay of the critical parameters to their continuum values.

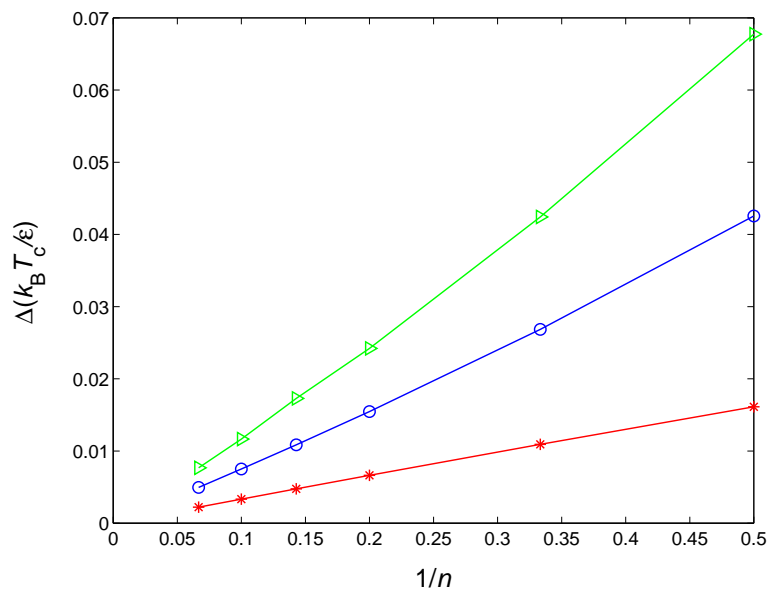


Figure 7.14: Reduced critical temperature as a function of $1/n$ for LGHCj model with no temperature effect. Symbols are the same as Figure 7.13.

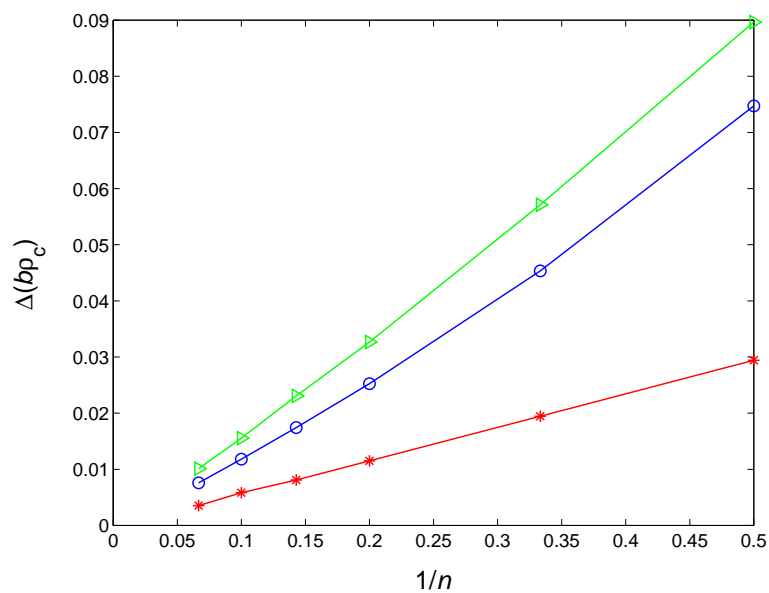


Figure 7.15: Reduced critical density as a function of $1/n$ for LGHCj model with some temperature effect. Symbols are the same as Figure 7.13.

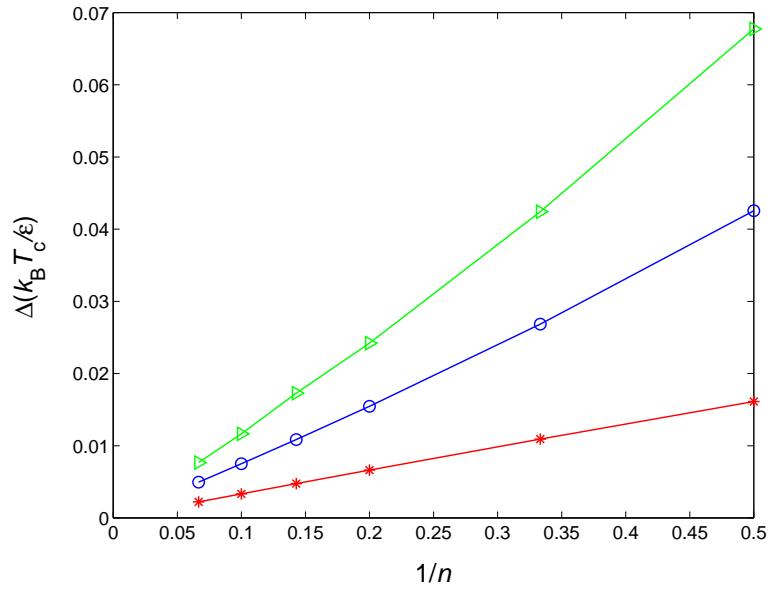


Figure 7.16: Reduced critical temperature as a function of $1/n$ for LGHCj model with some temperature effect. Symbols are the same as Figure 7.13.

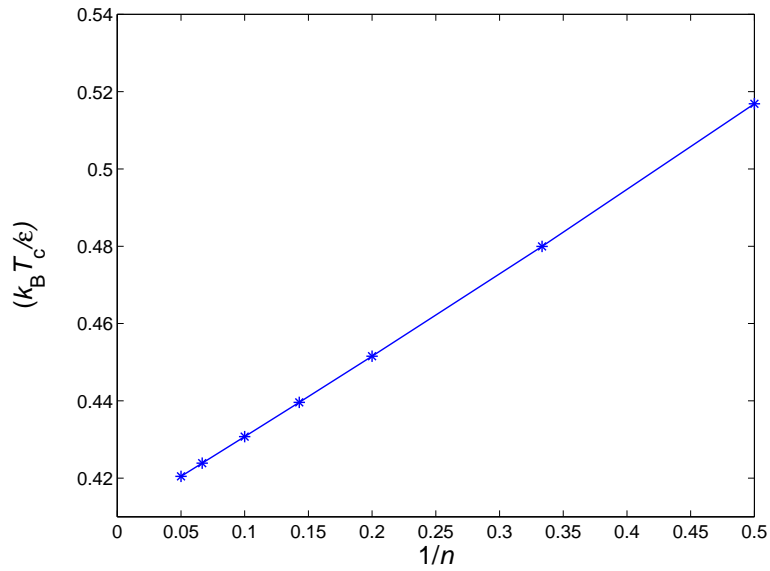


Figure 7.17: Reduced critical temperature as a function of $1/n$ for LGHCj model with $y_0 = 2.0$ and no temperature effect considered.

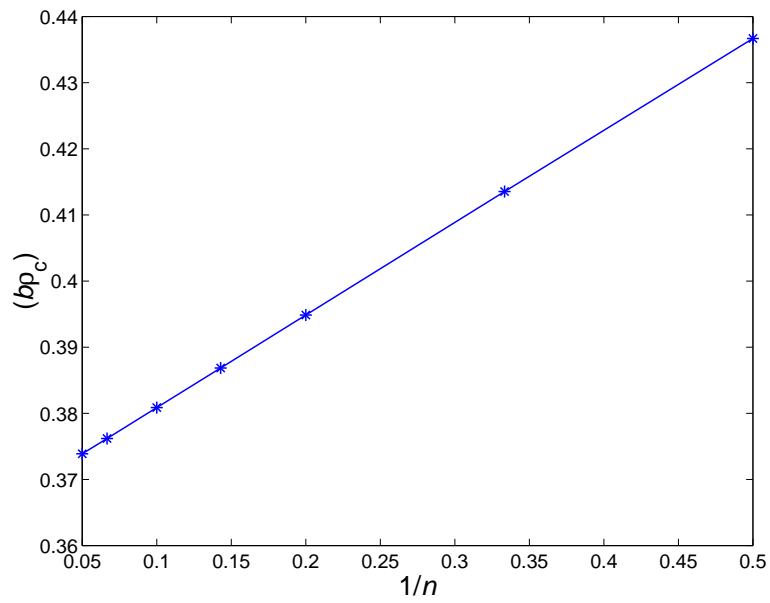


Figure 7.18: Reduced critical density as a function of $1/n$ for LGHCj model with $y_0 = 2.0$ and no temperature effect considered.

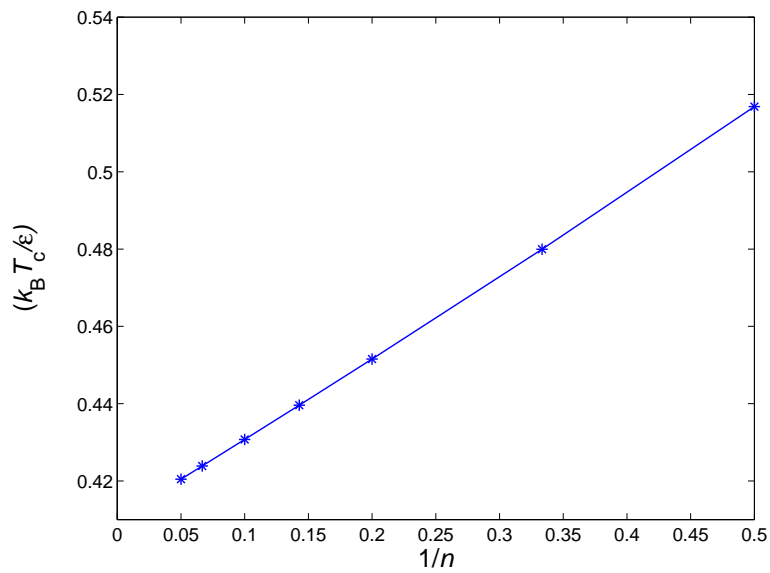


Figure 7.19: Reduced critical temperature as a function of $1/n$ for LGHCj model with $y_0 = 2.0$ when some temperature effect is considered.

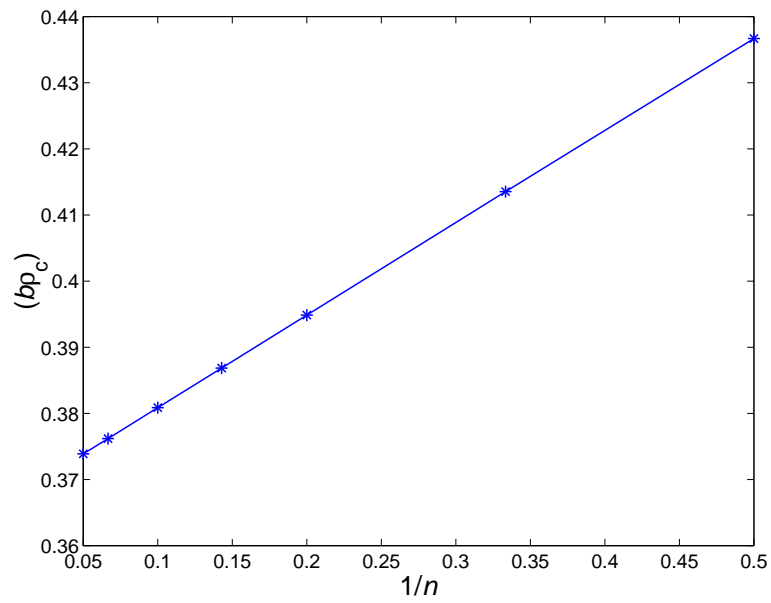


Figure 7.20: Reduced critical density as a function of $1/n$ for LGHCj model with $y_0 = 2.0$ when some temperature effect is considered.

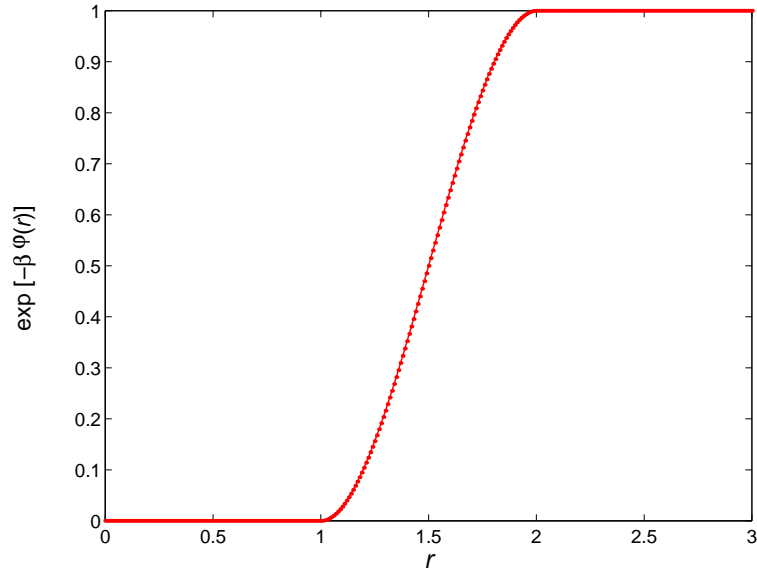


Figure 7.21: Boltzmann factor, $\exp[-\beta\varphi(r)]$, vs. distance, r , for cubic model.

7.3.7 Cubic model

The cubic potential model is defined as:

$$\varphi_l = \begin{cases} \infty & \text{if } la < b \\ -\epsilon \ln[1 + a_1(la - a_2) - a_3(la - a_4)^{a_5}] & \text{if } b \leq la < c \\ 0 & \text{if } la \geq c \end{cases} \quad (7.50)$$

As before, the conventional distance spacing, r , for continuous potential is replaced by la where index l labels the successive lattice sites and a is the lattice. The a_i parameters are chosen such that the Boltzmann factor $\exp(-\beta\varphi_l)$ behaves like Fig. 7.21 with a saddle point in the middle and a smooth variation with a continuously varying slope. In Figs. 7.22 - 7.25 we show the critical density and critical temperature for the cubic model for both sets of calculations where there exists no and some temperature effect, respectively. As seen, the critical parameters now increase linearly with $1/n^4$, which is indicative of a considerably faster convergence

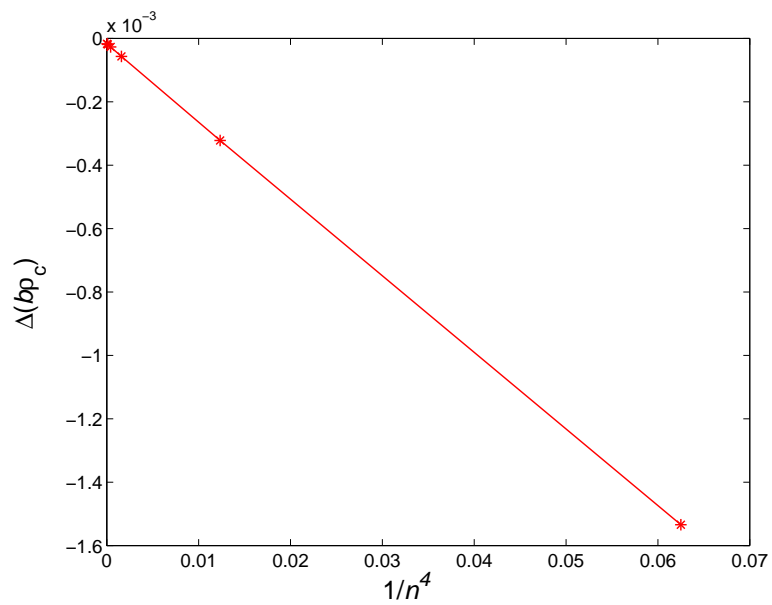


Figure 7.22: Reduced critical density as a function of $1/n^4$ for cubic model with no temperature effect.

for this family of potential functions.

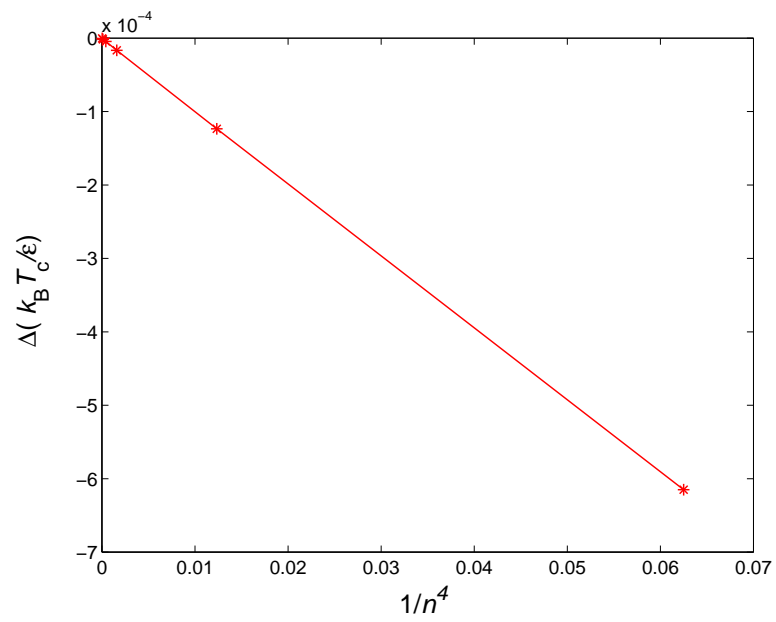


Figure 7.23: Reduced critical temperature as a function of $1/n^4$ for cubic model with no temperature effect.

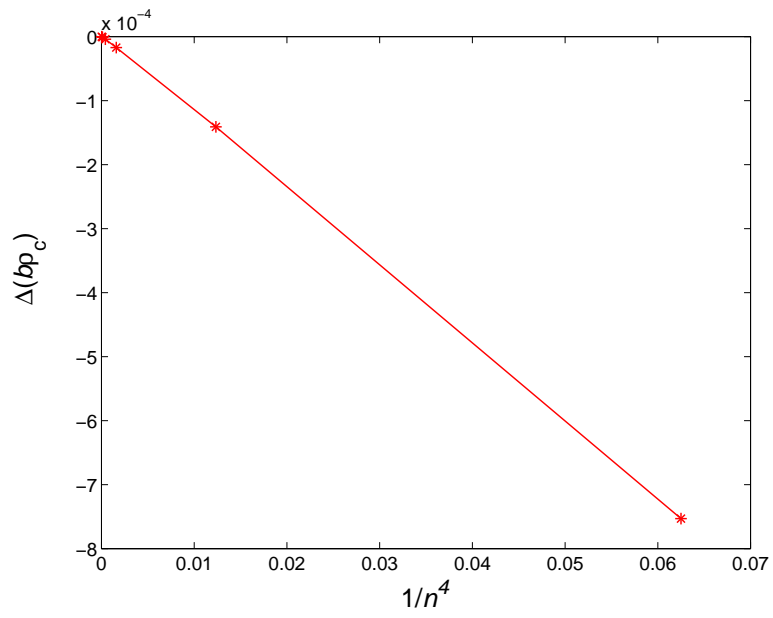


Figure 7.24: Reduced critical density as a function of $1/n^4$ for cubic model with some temperature effect.

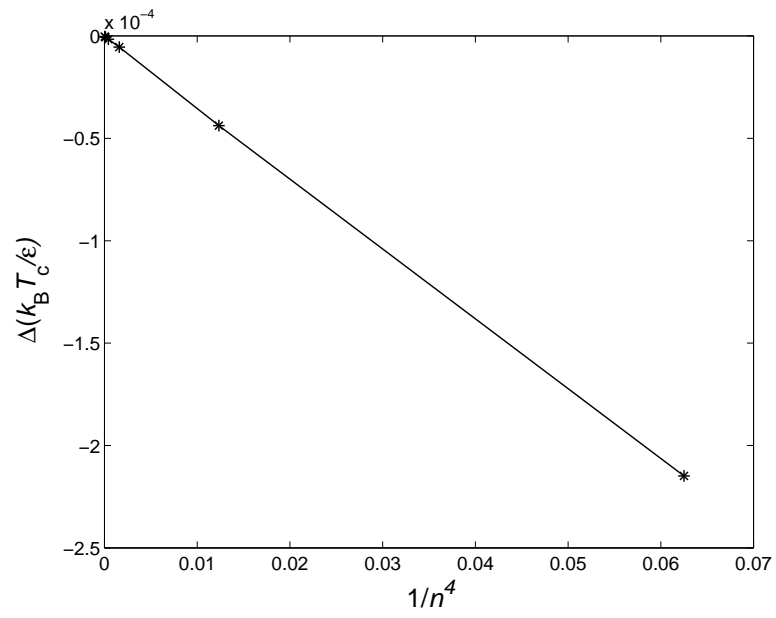


Figure 7.25: Reduced critical temperature as a function of $1/n^4$ for cubic model with some temperature effect.

7.4 Higher-dimensional models

For $d \geq 2$, the logical step is to extend the theory presented above to higher dimensions to find the critical parameters. However, in a less complex way, with the virial expansion theory, we can obtain a semi-exact solution for the hard-core model studied in two and three dimensions. The virial expansion is defined as [62]

$$\begin{aligned} \frac{p}{k_{\text{B}}T} &= \rho + B_2(T)\rho^2 + \mathcal{O}(\rho^3) + \dots \\ &= \rho \{1 + [b^0(T) + b^1(T)]\rho + \mathcal{O}(\rho^2) + \dots\}, \end{aligned} \quad (7.51)$$

where b^0 and b^1 are the second virial coefficients corresponding to the repulsive and attractive part of the potential, respectively. Within the VdW approximation, we have

$$\beta p \cong \frac{\rho}{1 - b^0(T)\rho} + b^1(T)\rho^2. \quad (7.52)$$

To obtain the VdW limit ($R_0 \rightarrow \infty$), one may postulate that the attractive part of the potential has the form

$$\phi^1(r) = -\frac{\epsilon}{R_0^d} \Phi\left(\frac{r}{R_0}\right), \quad (7.53)$$

with, in addition, the normalization condition

$$\int \Phi(x) d^d x = 1, \quad (7.54)$$

when $R_0 \rightarrow \infty$ this implies

$$b^1(T) \rightarrow -\frac{\epsilon}{T}. \quad (7.55)$$

We can conclude that all the deviations from the continuum limit must arise from $b^0(T)$ which is defined as [62]

$$b^0(T) = 1/2 \int d^d r \left[1 - e^{-\phi^0(r)/k_{\text{B}}T}\right]. \quad (7.56)$$

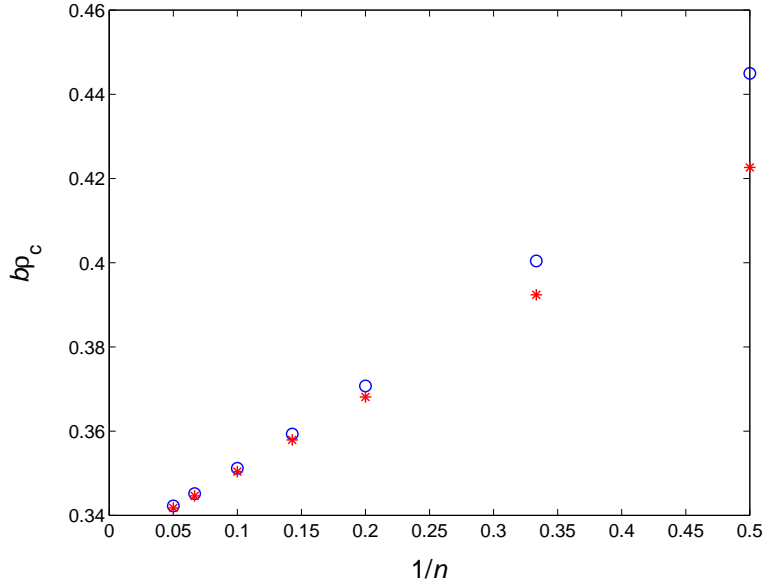


Figure 7.26: Reduced critical density obtained with both analytical (full stars) and VdW approximation method (open circles) for a one-dimensional system.

Obviously for the discretized model we have

$$b^0(T, \zeta) = 1/2 \sum_{l,m,n} \left[1 - e^{-\phi^0(\bar{r})/k_B T} \right] \quad (7.57)$$

with $\bar{r} = (l, m, n)a$, and $a = \frac{b}{\zeta}$. Finally, for a HC potential model we have:

$$b^0(T, \zeta) = 1/2 \frac{N(\zeta)}{\mathcal{W}}, \quad (7.58)$$

where $N(\zeta)$ is the number of lattice points covered by the hard-core with a scaling constant of \mathcal{W} . The calculation of $N(\zeta)$ is particularly crucial, since it provides insight into the number of the lattice discretization points covered by the hard-core. In Figs. 7.26 and 7.27, we show the critical density and critical temperature calculated analytically and via numerical analysis by using the VdW approximation for the HC model in one-dimensional space. As is shown, the results obtained with

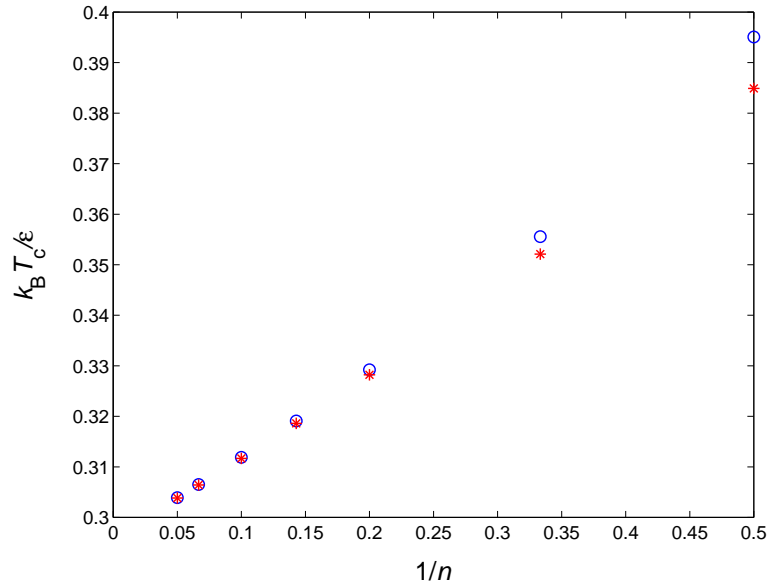


Figure 7.27: Reduced critical temperature obtained with both analytical (full stars) and VdW approximation method (open circles) for a one-dimensional system.

both methods agree for large values of n . In Figs. 7.28 and 7.29, we show the critical density and critical temperature obtained via VdW approximation for HC model for a three-dimensional system. As seen the critical parameters now decrease fairly rapidly as n increases.

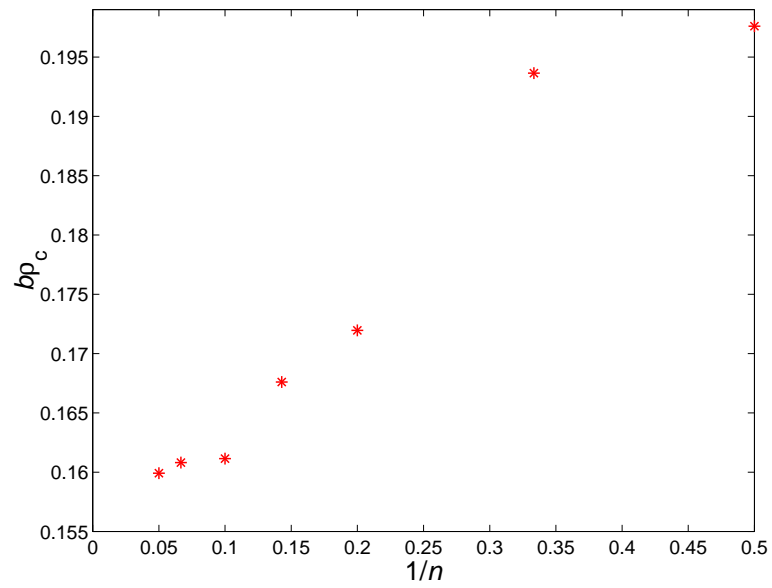


Figure 7.28: Reduced critical density obtained via VdW approximation method in $d = 3$.

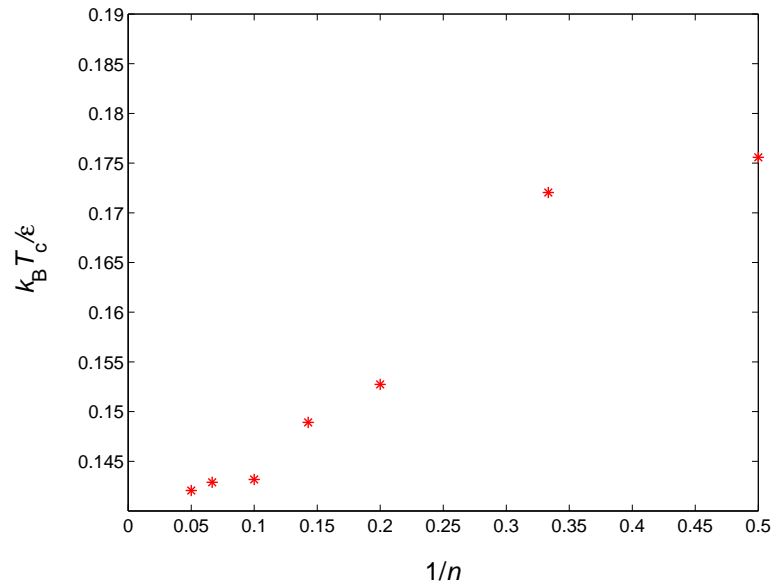


Figure 7.29: Reduced critical temperature obtained via VdW approximation method in $d = 3$.

7.4.1 Lattice discretization theory

Let

$$N(R) = \text{Cardinality} \{X \in Z^d : |X| \leq R\}, \quad (7.59)$$

where $N(R)$ is the number of lattice points inside a circle of radius R or a sphere of radius R centered at the origin, for $d = 2$ and $d = 3$, respectively. Here $X = (l_1, l_2, \dots, l_d)$ denotes the coordinates of the integer points satisfying the specified conditions. Let us put $R = \zeta a$, where a is the lattice spacing. For simplicity in the remaining part of this chapter we set $a = 1$. We would like to study the asymptotic behavior of

$$\frac{N(R)}{V(R)} = 1 + \mathcal{E}rror(R), \quad (7.60)$$

where $V(R)$ is the area of a circle with radius R or the volume of a sphere with radius R centered at the origin, for $d = 2$ and $d = 3$, respectively. In the continuum limit

$$N(R) = V(R) \rightarrow \pi R^2 \quad \text{for } d = 2, \quad (7.61)$$

$$N(R) = V(R) \rightarrow \frac{4}{3}\pi R^3 \quad \text{for } d = 3. \quad (7.62)$$

We may reasonably postulate that

$$\mathcal{E}rror(R) \sim \frac{1}{R^\psi}, \quad (7.63)$$

where $\mathcal{E}rror(R)$ is the error in approximating the sphere volume in d dimensions by the interior lattice sites. A theoretical study of this problem for $d = 2$ may be found in [126–128], where it is shown that $\psi = 3/2$ and an analytical formula for calculating the scaling constant is also provided. In what follows, we will study the asymptotic behavior of $\mathcal{E}rror(R)$ or how the error in volume, namely,

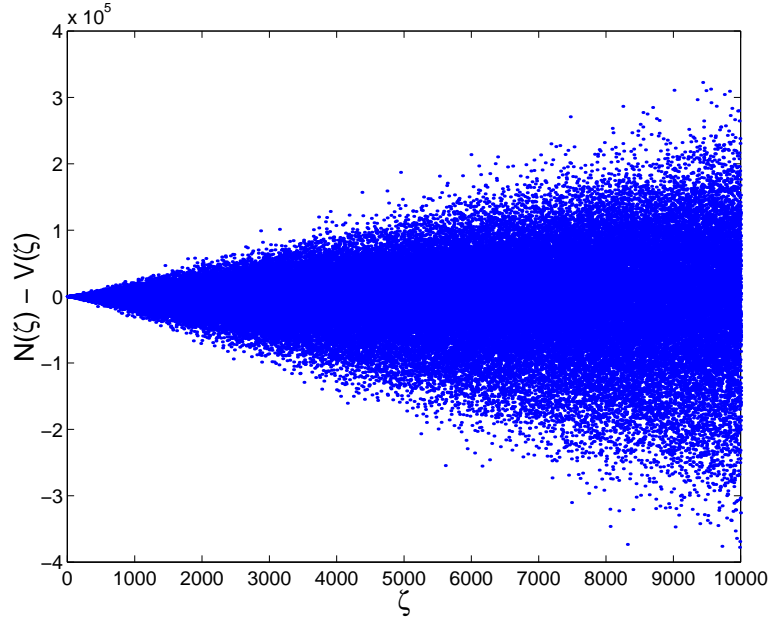


Figure 7.30: $N(\zeta) - V(\zeta)$ for different values of ζ in $d = 3$.

$[N(R) - V(R)]$, varies with R . Fig. 7.30 shows the error for values of $\zeta = 1 - 10000$.

7.4.2 Approximation of the error

Following an argument proposed by Prof. M. E. Fisher, let $A_R = C_d R^{d-1}$ be the area of a sphere of radius R . By intersection with the lattice cells this area is divided up into surface elements of mean area $A_0 \cong c_d a^{d-1}$ for $R/a \gg 1$, where c_d is an appropriate constant. Hence, the mean number of such elements is:

$$S_R \cong \frac{A_R}{A_0} = s_d \left(\frac{R}{a} \right)^{d-1}, \quad (7.64)$$

where $s_d = \frac{C_d}{c_d}$. Each surface element cuts a cell and, depending on the location of the cell, the cell center will be inside or outside of the R -sphere. As $R/a \rightarrow \infty$, we expect the probability of the center remaining in either region to approach $1/2$

and the error is either $+1/2$ or $-1/2$ on average. It follows that the total mean square error should thus be:

$$\langle \Delta N^2 \rangle \approx S_R \delta_d^2, \quad (7.65)$$

where $\Delta N = N(R) - V(R)$ and with $\delta_d \cong \frac{1}{2}$. Therefore we expect

$$\Delta N_{RMS}(R) \cong \sqrt{S_R} \delta_d = \delta_d \sqrt{s_d} \left(\frac{R}{a} \right)^{\frac{d-1}{2}}. \quad (7.66)$$

The root mean square errors (RMS), normalized according to this conclusion, (and smoothed with a running average window of lengths 3 and 5) are shown in Figs. 7.31, 7.32 and 7.33. The smoothed data are also shown in Fig. 7.34 in histogram form. The results clearly show that the absolute error normalized by $1/\zeta^{\frac{d-1}{2}}$ fluctuates around a constant value which is in good agreement with Eq. 7.66 and also the results of [126–128]. Hence, for common special cases we have

$$\begin{aligned} \Delta N_{RMS}(R) &= \delta_1 \sqrt{S_1} && \text{if } d = 1 \\ \Delta N_{RMS}(R) &= \delta_2 \sqrt{S_2} (R/a)^{1/2} && \text{if } d = 2 \\ \Delta N_{RMS}(R) &= \delta_3 \sqrt{S_3} (R/a)^1 && \text{if } d = 3. \end{aligned} \quad (7.67)$$

Finally, the fractional error at the ζ discretization level can be expressed as:

$$\frac{\Delta N(R)}{V(R)} \sim \frac{1}{R^{\frac{d+1}{2}}} \sim \frac{1}{\zeta^{\frac{d+1}{2}}}. \quad (7.68)$$

The fractional error for both $d = 2$ and $d = 3$ are shown in Figs. 7.35 and 7.36, respectively. As evident, the fractional error varies over a range bounded by $+c_+/\zeta^{3/2} > 0$ and $-c_-/\zeta^{3/2} < 0$, where c_+ and c_- are positive constants for $d = 2$. The same trend is observed for $d = 3$, where the fractional error varies over a range bounded by $+c_+/\zeta^2 > 0$ and $-c_-/\zeta^2 < 0$, where c_+ and c_- are positive constants, as expected from Eq. 7.68.

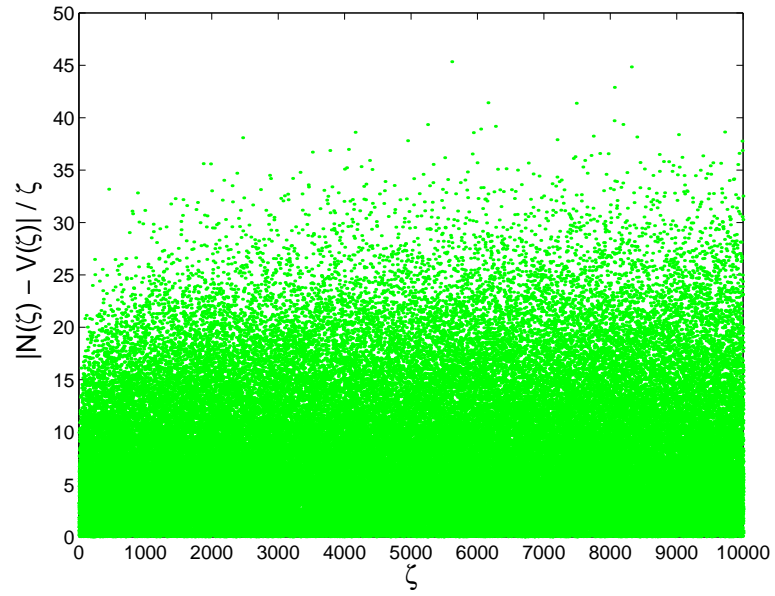


Figure 7.31: RMS versus ζ for $d = 3$.

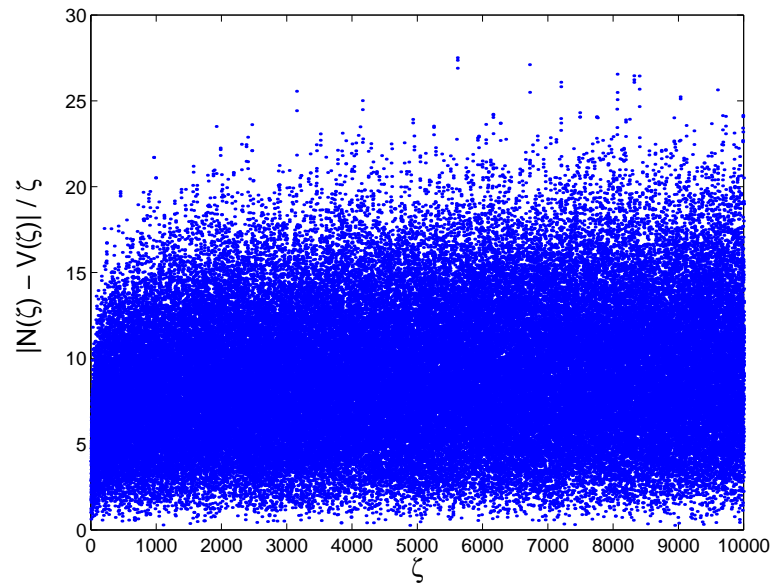


Figure 7.32: RMS being smooth with 3 points versus ζ for $d = 3$.

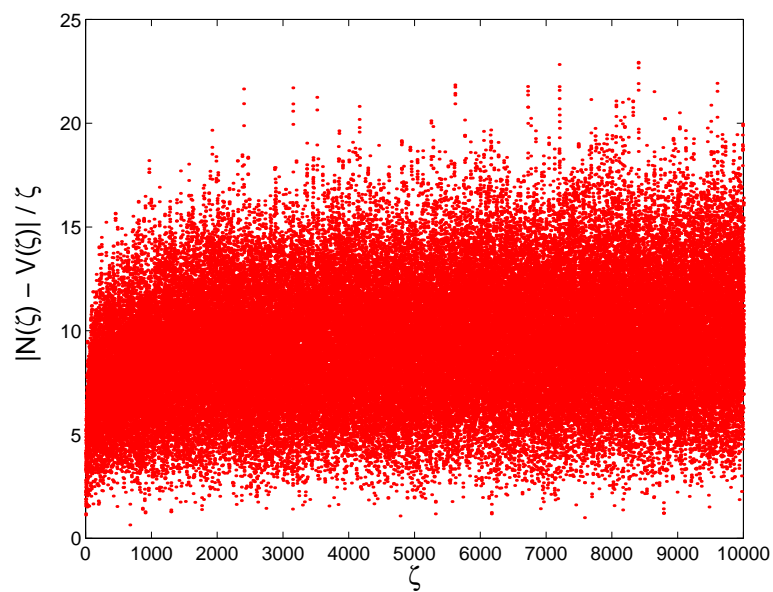


Figure 7.33: RMS being smooth with 5 points versus ζ for $d = 3$.

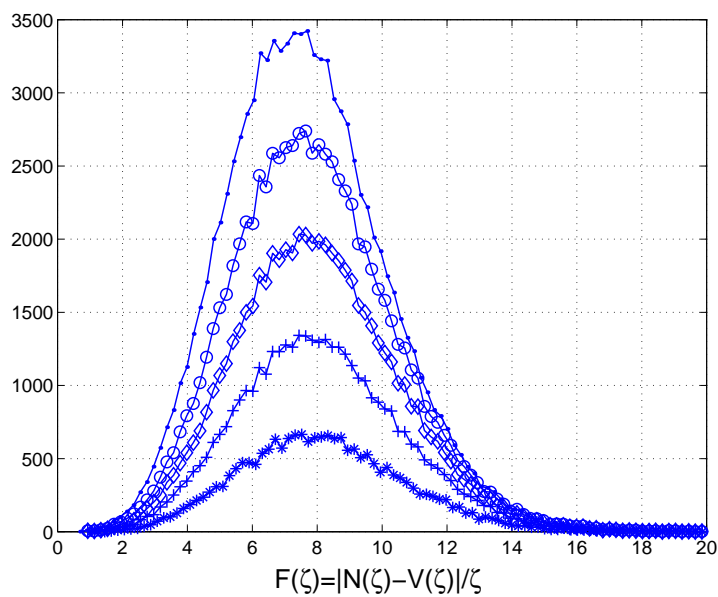


Figure 7.34: The plots from top to bottom are for $\zeta = 1 - 10000, 1000 - 10000, 2000 - 10000, 4000 - 10000, \dots$, and $8000 - 10000$ for $d = 3$, respectively.

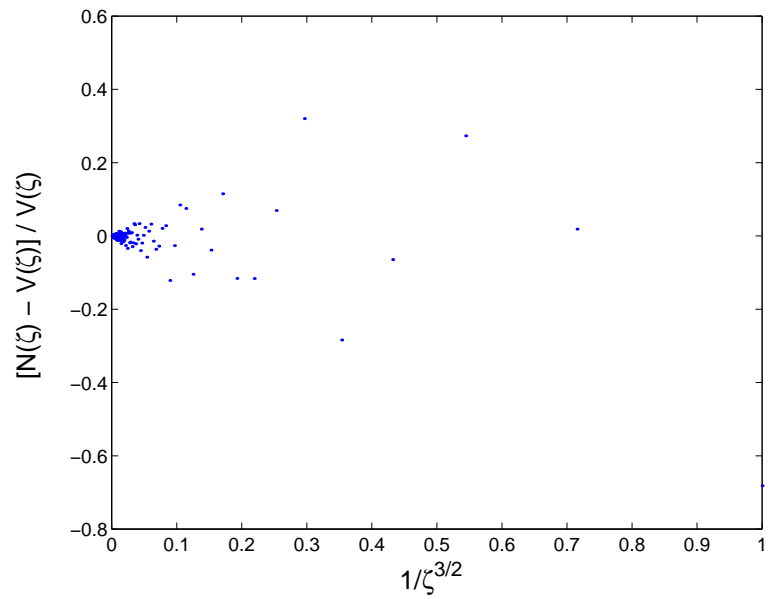


Figure 7.35: The fractional error for $d = 2$ versus $1/\zeta^{3/2}$.

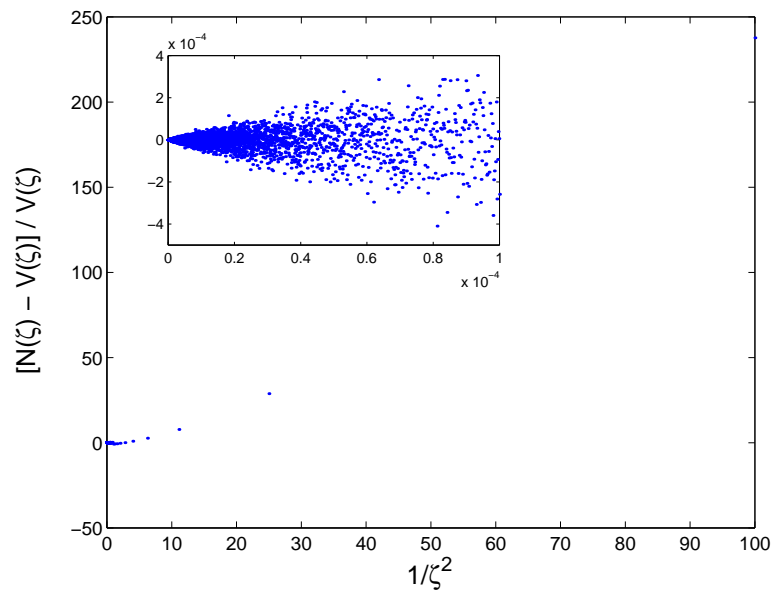


Figure 7.36: The fractional error for $d = 3$ versus $1/\zeta^2$.

In Fig. 7.37 we show the second virial coefficient of the HC model for different values of ζ . The data suggest that deviations of the second virial coefficients scale as $1/\zeta^2$. The exponent found in the present study for the HC model is essentially identical to the exponent found for the critical temperatures and critical densities of the restricted primitive model (RPM) by Panagiotopoulos [110]. The potential function for the RPM is made up of a hard-core and a smoothly varying Coulombic long range part. We may conclude that the hard-core part of the potential is responsible for the exponent observed in this study. Fig. 7.38 shows the dependence of the second virial coefficients of a standard soft-core potential, namely, the Lennard-Jones potential [64], at the dimensionless critical temperature, $T_c^* = k_B T/\epsilon = 1.299$, on the inverse lattice discretization parameter scaled to the 6th power. This exponent is also in agreement with the exponent that has been found for the critical parameter dependence on the inverse lattice discretization parameter for a soft-core potential model (as found via the simulation studies reported in Chap. 5). Finally, in summary, the behavior of the second virial coefficient under discretization, which may easily be studied numerically if not so readily by analytical means, appears to provide a reliable guide to the rate of convergence to the expected in estimating critical parameters.

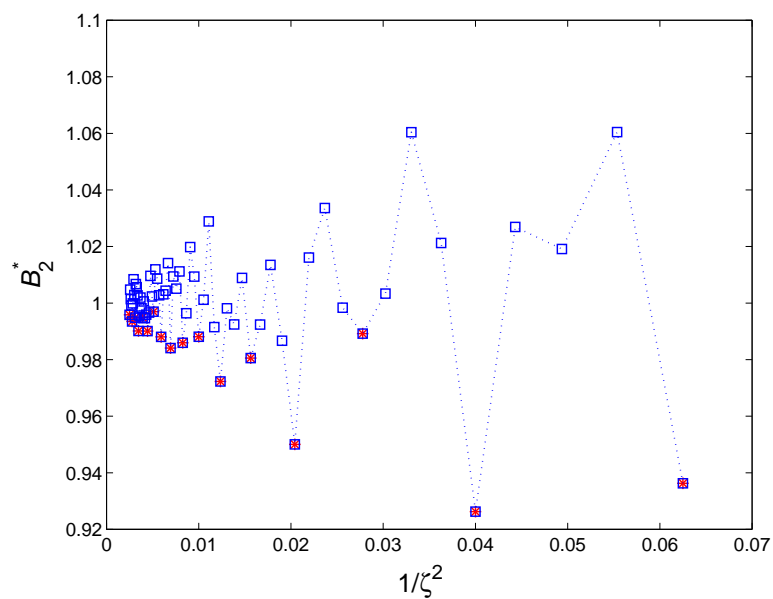


Figure 7.37: Second virial coefficient for the hard-core model with integer (stars) and real (open squares) values of ζ .

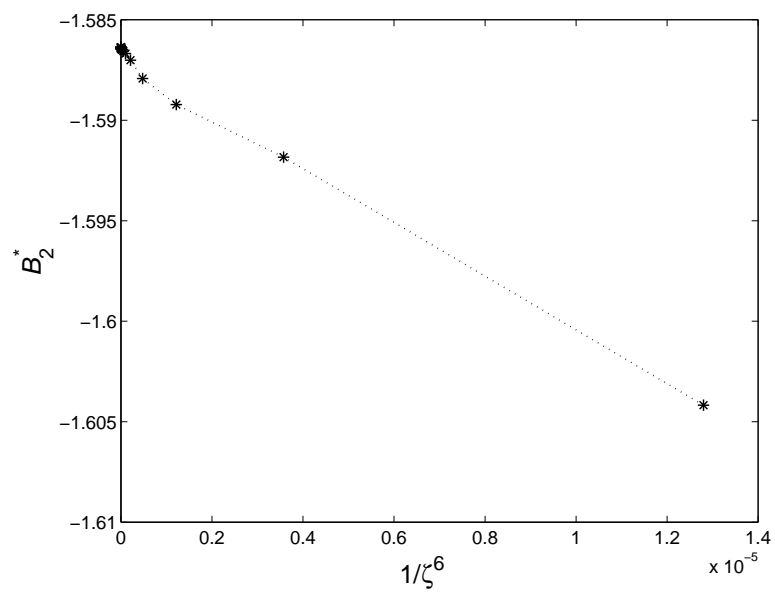


Figure 7.38: Second virial coefficient for the LJ model at $T_c^* = 1.299$.

Chapter 8

Summary and Suggestions for Future Work

In this dissertation we have focused on the development of the fine lattice discretization methodology pioneered by Panagiotopoulos and Kumar [2] to allow for calculation of structural and thermodynamic properties, mainly phase equilibria and critical parameters, of various model and real fluids. A wide range of fluids was studied, from simple model Buckingham Exp-6 particles to polar multi-segment real molecules which include both dispersive and Coulombic interactions. We have investigated various phenomenological approaches to see how well the lattice models incorporate the models when the continuum limit is approached. Grand canonical histogram reweighting simulations and mixed-field finite-size scaling analysis were used to determine the phase coexistence properties and critical parameters. Structural properties, mainly density profile and radial distribution functions, were calculated using canonical simulations.

To evaluate the fine-lattice discretization technique, the phase behavior and critical parameters of diatomic molecules, carbon dioxide, and water were calcu-

lated using this method and the results were compared to the continuum counterparts. In comparison with the previous calculations in continuum-space, the lattice discretization technique appears to have a superior efficiency; indeed the lattice calculations can run up to two orders of magnitude faster than the continuum calculations for polar models. Overall, there is good agreement between the phase equilibria and critical parameters of the models studied in both lattice and continuum spaces. Small deviations in the low density region can be observed for carbon dioxide and water models. On the one hand, we postulate that system-size effects are responsible for these deviations; but the computational cost to calculate the properties of interest in larger systems is prohibitively high with the methods of the present work and the available CPU capacity. On the other hand, when real models are discretized in lattice space, the allowable values for bond length, bond angle, dipole moment, quadrupole moment, etc. must, in general, deviate from the continuum values. This can lead to sizeable errors owing to the restrictions placed on separation distances, where a site's location can be described only by an integer between zero and the box dimensionless length in all the directions.

We have also investigated the structural properties of the SPC/E water model with different lattice discretization parameters, ζ . It was found that even very small changes in the lattice spacing can have a large effect on the overall structural properties of these models. For example, $\zeta = 11$ shows frozen structures at $T = 400$ K, while some discretized models show only minor underlying structures and some others do not exhibit any underlying structure. The underlying structures in radial distribution functions are not as pronounced as in the density profiles and, except for $\zeta = 11$ and, to a minor extent for $\zeta = 22$, no specific structures are observed for other lattice models.

One of the primary and important parameters defined in the lattice discretization technique is the lattice discretization parameter, ζ . We have investigated extensively the effect of the lattice discretization parameter on the critical parameters, mainly critical temperature and critical density, for a variety of model polar and non-polar models. Both critical temperature and critical density decrease on increasing ζ . The critical temperature scales as $1/\zeta^\alpha$, where the exponent fitted was $\alpha = (6 \pm 2)$ for the non-polar and $\alpha = (2 \pm 0.5)$ for the polar fluids. The large difference in α values between non-polar and polar fluids results from a much weaker effect of discretization on the critical parameters of non-polar fluids.

Grand canonical multihistogram reweighting Monte Carlo calculations using the fine-lattice discretization methods were carried out to obtain the second virial coefficients for a number of systems of interest. A fast and efficient methodology to estimate the second virial coefficient was presented. It was shown that the methodology yields very good estimates of the second virial coefficient and agreement with analytical and experimental values at about 2% for a variety of model and real fluids, respectively.

The thesis concludes with a comprehensive theoretical study of the effect of the lattice discretization parameter on critical parameters such as critical temperature and critical density. For low values of lattice discretization parameter, the underlying lattice may have a strong effect on the thermodynamic and structural properties of the system, whereas for values greater than 10, the properties have essentially identical behavior to their continuum counterparts. In one-dimensional space ($d = 1$), we have investigated the problem analytically for the hard-core potential model and numerically for the square-well and a variety of logarithmic hard-core potentials. It was found that the deviations in the values of the critical

parameters decrease hyperbolically with increasing lattice discretization parameter, n , while for the logarithmic hard-core potential models the smoothness of the repulsive part of the function is mainly responsible for the rate of convergence. The notation n is used for the lattice discretization parameter when it only takes integer values whereas the ζ notation has been used when the lattice discretization parameter can take any positive real values. We presented a numerical study of two-dimensional ($d = 2$) and three-dimensional ($d = 3$) cases and investigated the dependence on the lattice discretization parameter of the number of lattice points, $N(R)$, contained in a circle or sphere of radius R (equal to the hard-core diameter). The distribution of $N(R)$ varies in a “noisy” fashion around a definite form.

Based on the results of the researches reported in this thesis on both simulation and theoretical aspects, a number of projects for future work are possible. As the internal structural properties of a molecule such as bond length, bond angle, dipole moment, etc., must be altered to force each site of the molecule to span an integral number of lattice spaces while adhering as closely as possible to continuum values, this technique can lead to sizeable errors with respect to the exact values of the internal properties. In order to further investigate both thermodynamic and structural properties of models studied in lattice space and to see how closely the lattice models reach their continuum counterparts, it is important to have a clear picture of the effects of the lattice discretization on the internal structural properties of the fluids and consequently on the properties of interest.

As a long-term motivation is to build fine-lattice models reproducing properties of any real systems and their mixtures, the lattice discretization technique should be applicable for calculating the properties of molecules with any number of sites. For molecules with more than three sites, the torsional angle is also an added

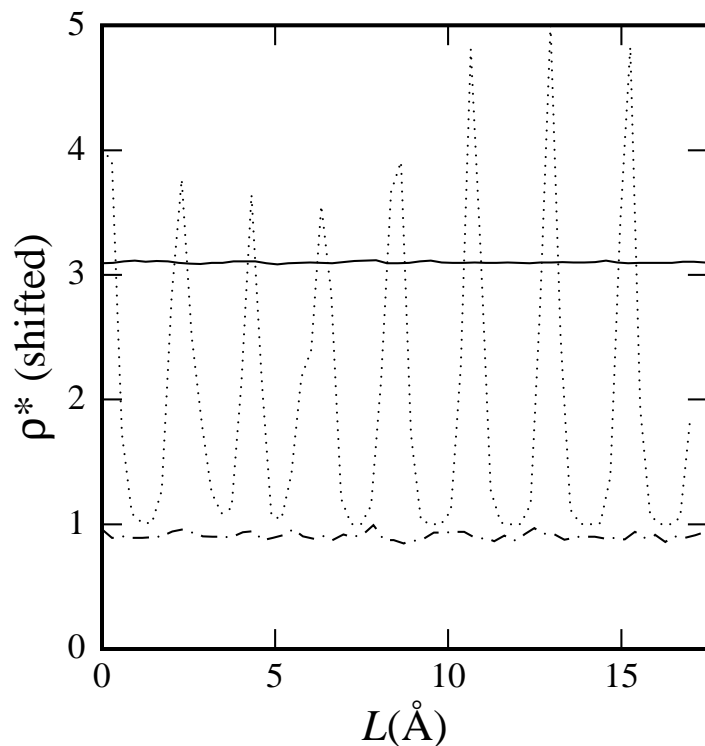


Figure 8.1: Density profile of water models at $T = 400$ K with $\zeta = 11$: Buckingham Exp-6 model (dashed-dotted line), SPC/E model (dotted line), and continuum model (solid line).

parameter to the internal degrees of freedom and some of the effects of lattice discretization on the properties of interest might be due to this added parameter. Overall, having a clear understanding of the effects of internal structural properties on the properties of interest with a constant lattice discretization parameter, ζ , is essential for the usefulness of further calculations on real fluids in lattice space.

We have observed that small changes in the lattice spacing can have a large effect on the structural properties, especially the density profile, of the SPC/E water model. It will be useful to examine this effect for other models with different

intermolecular interactions which can lead us to see whether the peculiar behavior is due to the nature of the intermolecular potential or is related to the internal structural properties of the models. For example, the density profile of the water model with an Exp-6 profile having a lattice discretization value of $\zeta = 11$ at $T = 400$ K is shown in Fig. 8.1: no strong underlying structures (such as seen for SPC/E water with $\zeta = 11$) now appear. There is also the possibility namely, that the distinct configurational structures of the molecules combined with the chosen potential model cause this effect. In another perspective, some of the models show some periodic behavior in their density profile, although these periodic effects are not as pronounced as those of the water models studied by Lock [109]. In particular, the direct correlation between the characteristic size of the potential and the periodic bond length of the density profile function should be studied thoroughly.

We have not identified any specific trends regarding the effect of the lattice discretization parameters on the critical densities of the non-polar and polar model fluids studied in Chapter 5. This is partly a result of the higher statistical uncertainties associated with the calculation of the critical density. The technique used recently by Kim and Fisher [129] to precisely calculate the critical parameters of the RPM and square-well fluid can be applied to the models studied in Chapter 5 and the precise effect of lattice discretization on critical densities could be investigated. In Chapter 5 we also found that the effect of lattice discretization on critical temperatures is weaker for a model with combined dispersive and Coulombic interactions than for a model with only dispersive interactions. This is in contrast to our belief that the added Coulombic part should make the dependence somewhat stronger. These models need further investigation owing to the marked similarities between these model fluids and real fluids in nature.

Following suggestions made by Prof. M. E. Fisher, one may consider a number of interesting open problems for further investigation on the theoretical side. For hard-core models, the density is made dimensionless using the hard-core diameter via $\rho^* = \rho\sigma^d$, where σ is the hard-core diameter and d is the dimensionality of the space. We may write

$$\rho^* = \rho\sigma^d = \rho \frac{V(\zeta)}{\frac{4}{3}\pi(\zeta/\sigma)^d}, \quad (8.1)$$

where ζ is the lattice discretization parameter and $V(\zeta)$ is the volume excluded by ζ . By replacing $V(\zeta)$ by $N(\zeta)a^d$, where $N(\zeta)$ is the actual number of points excluded by ζ and a is the lattice spacing, a new scaling factor for density can be defined as

$$\rho^\dagger = \rho\sigma^d \frac{N(\zeta)}{\frac{4}{3}\pi\zeta^d} = \rho\sigma^{\dagger 3}. \quad (8.2)$$

We postulate that using this new scaling factor may well result in a faster convergence of the density calculated in lattice space to its continuum value. Since the second virial coefficient has the same dimension as the hard-core diameter, scaling the density with the second virial coefficient is also another possibility which needs further investigation.

The temperature is normally made dimensionless by setting $T^* = \frac{k_B T}{\epsilon}$, with $\epsilon = \frac{|q_i q_j|}{D\sigma}$, where q_i and q_j are the charges on nearest neighbor sites i and j and D represents the dielectric constant of the structureless medium. However, we can define a new scaling factor for the lattice system by averaging the contact energy of the lattice surface of the hard-core instead of using only its diameter since ϵ relates to the energy of closest approach. Then one should study how fast the new scaled temperature converges to its continuum value with the hope of improvement.

BIBLIOGRAPHY

- [1] W. L. Jorgensen, J. D. Madura, and C. J. Swenson, *J. Am. Chem. Soc.*, **106**, 813 (1984).
- [2] A. Z. Panagiotopoulos and S. K. Kumar, *Phys. Rev. Lett.*, **83**, 2981 (1999).
- [3] A. Z. Panagiotopoulos, *J. Chem. Phys.*, **112**, 7132 (2000).
- [4] J. R. Errington and A. Z. Panagiotopoulos, *J. Phys. Chem. B*, **103**, 6314 (1999).
- [5] D. Ambrose and C. Tsonopoulos, *J. Chem. Eng. Data*, **40** (1995).
- [6] NIST - Chemistry WebBook, <http://webbook.nist.gov/chemistry>, 1982.
- [7] R. Guida and J. Zinn-Justin, *J. Phys. A*, **31**, 8103 (1998).
- [8] *Handbook of Chemistry and Physics*, 1995.
- [9] J. K. Johnson, J. A. Zollweg, and K. E. Gubbins, *Mol. Phys.*, **78**, 591 (1993).
- [10] A. Z. Panagiotopoulos, *Mol. Phys.*, **61**, 813 (1987).
- [11] B. Smit, P. Smedt, and D. Frenkel, *Mol. Phys.*, **68**, 931 (1989).
- [12] A. Z. Panagiotopoulos, *Mol. Phys.*, **63**, 527 (1988).

- [13] K. K. Mon and K. Binder, *J. Chem. Phys.*, **96**, 6989 (1992).
- [14] J. R. Reght and A. Z. Panagiotopoulos, *Molec. Phys.*, **80**, 843 (1993).
- [15] A. Z. Panagiotopoulos, *Int. J. Thermophys.*, **15**, 1057 (1994).
- [16] J. P. Valleau, *J. Chem. Phys.*, **108**, 2962 (1998).
- [17] J. J. Potoff and A. Z. Panagiotopoulos, *J. Chem. Phys.*, **109**, 10914 (1998).
- [18] N. B. Wilding, *Phys Rev. E*, **52**, 602 (1995).
- [19] J. J. Potoff and A. Z. Panagiotopoulos, *J. Chem. Phys.*, **109**, 10914 (1998).
- [20] A. M. Ferrenberg and R. H. Swendsen, *Phys. Rev. Lett.*, **61**, 2635 (1988).
- [21] A. M. Ferrenberg and R. H. Swendsen, *Phys. Rev. Lett.*, **63**, 1195 (1988).
- [22] N. B. Wilding and A. D. Bruce, *J. Phys.:Condens. Matter*, **4**, 3087 (1992).
- [23] A. D. Bruce and N. B. Wilding, *Phys. Rev. Lett.*, **68**, 193 (1992).
- [24] A. Z. Panagiotopoulos, V. Wong, and M. A. Floriano, *Macromolecules*, **31**, 912 (1998).
- [25] J. Errington and A. Z. Panagiotopoulos, *J. Chem. Phys.*, **109**, 1093 (1998).
- [26] P. Ewald, *Ann. Phys.*, **64**, 253 (1921).
- [27] E. Madelung, *Phys. Z.*, **19**, 524 (1918).
- [28] I. Carmesin and K. Kremer, *Macromolecules*, **21**, 2819 (1988).
- [29] H. P. Deutsch and K. Binder, *J. Chem. Phys.*, **94**, 2294 (1991).

- [30] A. Kolinski, L. Jaroszewki, P. Rotkiewicz, and J. Skolnick, *J. Phys. Chem. B*, **102**, 4628 (1998).
- [31] A. Kolinski, P. Rotkiewicz, B. Ilkowski, and J. Skolnick, *Proteins*, **37**, 592 (1999).
- [32] N. Rathore and J. de Pablo, *J. Chem. Phys.*, **116**, 7225 (2002).
- [33] P. Doruker and W. L. Mattice, *Macromolecules*, **31**, 1418 (1998).
- [34] G. Orkoulas and A. Z. Panagiotopoulos, *J. Chem. Phys.*, **110**, 1581 (1999).
- [35] A. Ciach and G. Stell, *J. Chem. Phys.*, **114**, 3617 (2001).
- [36] R. Dickman and G. Stell, *Simulation and Theory of Electrostatic Interaction in Solutions*, edited by L. R. Pratt and G. Hummer. AIP, Woodbury, 1999.
- [37] M. E. Fisher, *Rep. Prog. Phys.*, **30**, 615 (1967).
- [38] L. P. Kadanoff, *Rev. Mod. Phys.*, **39**, 395 (1967).
- [39] B. Widom, *J. Chem. Phys.*, **43**, 3898 (1965).
- [40] R. B. Griffiths, *Phys. Rev.*, **158**, 176 (1967).
- [41] A. Z. Patashinskii and V. L. Pokrovskii, *Sov. Phys. JEPT*, **23**, 292 (1966).
- [42] B. Widom, *Physica*, **73**, 107 (1974).
- [43] N. Metropolis, N. R. A. W. Rosenbluth, and A. H. Teller, *J. Chem. Phys.*, **21**, 1087 (1953).
- [44] J. P. Valleau and D. N. Card, *J. Chem. Phys.*, **57**, 5457 (1972).
- [45] G. M. Torrie and J. P. Valleau, *Chem. Phys. Lett.*, **28**, 578 (1974).

- [46] G. M. Torrie and J. P. Valleau, *J. Comp. Phys.*, **23**, 187 (1977).
- [47] A. Z. Panagiotopoulos, *J. Phys.: Condens. Matter*, **12**, R25 (2000).
- [48] N. Metropolis, A. W. Rosenbluth, M. N. Rosenbluth, A. N. Teller, and E. Teller, *J. Chem. Phys.*, **21**, 1087 (1953).
- [49] D. P. Landau and K. Binder, *A Guide to Monte Carlo Simulations in Statistical Physics*, Cambridge University press, 2000.
- [50] D. Frenkel and B. Smit, *Understanding Molecular Simulation*, Academic Press, London, 1996.
- [51] A. P. Allen and D. J. Tildesley, *Computer Simulation of Liquids*, Clarendon Press, Oxford, 1987.
- [52] J. V. Sengers and J. M. H. Levelt Sengers, *Progress in Liquid Physics*, edited by C. A. Croxton, Wiley, Chichester, UK, 1987.
- [53] M. S. Green, M. Vicentini-Missoni, and J. M. H. Levelt Sengers, *Phys. Rev. Lett.*, **18**, 1113 (1967).
- [54] M. Vicentini-Missoni, J. M. H. Levelt Sengers, and M. S. Green, *Phys. Rev. Lett.*, **22**, 389 (1969).
- [55] M. Vicentini-Missoni, R. I. Joseph, M. S. Green, and J. M. H. Levelt Sengers, *Phys. Rev. B*, **1**, 2312 (1970).
- [56] Y. C. Kim, Ph.D. Thesis, University of Maryland (2002).
- [57] N. D. Mermin, *Phys. Rev. Lett.*, **26** (1971).
- [58] J. J. Rehr and N. D. Mermin, *Phys. Rev. A*, **8** (1973).

- [59] C. N. Yang and C. P. Yang, Phys. Rev. Lett., **13**, 303 (1964).
- [60] M. E. Fisher and G. Orkoulas, Phys. Rev. Lett., **85**, 696 (2002).
- [61] M. E. Fisher, G. Orkoulas, and A. Z. Panagiotopoulos, Phys. Rev. E, **63**, art No 051507 (2001).
- [62] D. A. McQuarrie, *Statistical Mechanics*, University Science Books, 2000.
- [63] P. Debye and E. Hückel, Phys. Z., **24** (1923).
- [64] J. E. Lennard-Jones, Proc. R. Soc. London, Ser. A, **106**, 441 (1924).
- [65] J. E. Lennard-Jones, Proc. R. Soc. London, Ser. A, **106**, 463 (1924).
- [66] S. Moghaddam and A. Z. Panagiotopoulos, J. Chem. Phys., **18**, 7556 (2003).
- [67] A. J. Stone, *The Theory of Intermolecular Forces*, Clarendon Press, Oxford, 1996.
- [68] R. A. Buckingham, Proc. R. Soc. London, Ser. A, **168**, 264 (1938).
- [69] J. N. Israelachvili, *Intermolecular and Surface Forces*, Academic Press Inc., San Diego, 1992.
- [70] M. Oobatake and T. Ooi, Progress of Theoretical Phys., **48**, 2132 (1972).
- [71] J. Barojas, D. Levesque, and B. Quentrec, Phys. Rev A, **7**, 1092 (1973).
- [72] P. S. Y. Cheung and J. G. Powles, Mol. Phys., **30**, 921 (1975).
- [73] J. R. Sweet and W. A. Steele, J. Chem. Phys., **47**, 3029 (1967).
- [74] K. Singer, A. Taylor, and V. L. Singer, Mol. Phys., **33**, 1757 (1976).

- [75] K. Singer, J. V. L. Singer, and A. J. Taylor, *Mol. Phys.*, **37**, 1239 (1979).
- [76] J. G. Powles and K. E. Gubbins, *Mol. Phys. Lett.*, **38**, 405 (1975).
- [77] C. Kriebel, A. Muller, M. Mecke, J. Winkelmann, and J. Fischer, *Int. J. Thermo.*, **17**, 1349 (1996).
- [78] G. Gallassi and D. J. Tildesley, *Molecular simulation*, **13**, 11 (1994).
- [79] M. G. Martin and J. I. Siepmann, *J. Phys. Chem. B*, **102**, 2569 (1998).
- [80] B. Chen, M. Martin, and J. I. Siepmann, *J. Phys. Chem. B*, **102**, 2578 (1998).
- [81] S. K. Nath, F. A. Escobedo, and J. de Pablo, *J. Chem. Phys.*, **108** (1998).
- [82] S. K. Nath and J. de Pablo, *J. Phys. Chem. B*, **103**, 3539 (1999).
- [83] D. N. Theodorou and U. W. Suter, *J. Chem. Phys.*, **82**, 955 (1985).
- [84] W. H. Press, S. A. Teukolsky, W. T. Vetterling, and B. P. Flannery, *Numerical Recipes in FORTRAN*, 2nd ed. Cambridge University Press, Cambridge, 1992.
- [85] B. Smit, S. Karaborni, and J. I. Siepmann, *J. Chem. Phys.*, **102** (1995).
- [86] E. Kiran and J. M. H. Levelt-Sengers, *Supercritical Fluids Fundamentals for application*, Kluwer Academic Publishers, 1993.
- [87] J. D. Bernal and R. H. Fowler, *J. Chem. Phys.*, **97**, 13841 (1993).
- [88] F. H. Stillinger and A. Rahman, *J. Chem. Phys.*, **60**, 1545 (1974).
- [89] W. L. Jorgensen, *J. Chem. Phys.*, **77**, 4156 (1982).

- [90] W. L. Jorgensen, J. Chandrasekhar, J. D. Madura, R. W. Impley, and M. L. Klein, *J. Chem. Phys.*, **79**, 926 (1983).
- [91] H. J. C. Berendsen, J. P. M. Postma, W. F. V. Gunsteren, and J. Hermans, *Intermolecular Forces*, edited by B. Pullman Reidel, Dordrecht, Holland, 1981.
- [92] H. J. C. Berendsen, J. R. Grigera, and T. P. Straatsma, *J. Phys. Chem.*, **91**, 6269 (1987).
- [93] G. C. Boulougouris, I. G. Economou, and D. N. Theodorou, *J. Phys. Chem. B*, **102**, 1029 (1998).
- [94] J. R. Errington, G. C. Boulougouris, I. G. Economou, A. Z. Panagiotopoulos, and D. N. Theodorou, *J. Phys. Chem.*, **102**, 8865 (1998).
- [95] J. R. Errington and A. Z. Panagiotopoulos, *J. Phys. Chem. B*, **102**, 7470 (1998).
- [96] S. W. Rick, S. Stuart, and B. J. Berne, *J. Chem. Phys.*, **101**, 6141 (1994).
- [97] M. Medeiros and M. E. Costas, *J. Chem. Phys.*, **107**, 2012 (1997).
- [98] I. M. Svishchev, P. G. Kusalik, J. Wang, and R. J. Boyd, *J. Chem. Phys.*, **105**, 4742 (1996).
- [99] A. Wallqvist and B. J. Berne, *J. Phys. Chem.*, **97**, 13841 (1993).
- [100] A. A. Chialvo and P. T. Cummings, *J. Phys. Chem.*, **105**, 8274 (1996).
- [101] M. Martin, B. Chen, and J. I. Siepmann, *J. Chem. Phys.*, **108**, 3384 (1998).
- [102] M. Sprik and M. L. Klein, *J. Chem. Phys.*, **89**, 7556 (1988).

- [103] B. Chen, J. Xing, and J. I. Siepmann, *J. Chem. Phys. B*, **104**, 2391 (2000).
- [104] B. Chen, J. J. Potoff, and J. I. Siepmann, *J. Chem. Phys. B*, **104**, 2378 (2000).
- [105] J. G. Harris and K. H. Yung, *J. Phys. Chem.*, **99** (1995).
- [106] J. R. Errington, Ph.D. Thesis, Cornell University (1999).
- [107] S. Natarajan and J. K. Maranas, *J. Phys. Chem.*, **118** (2003).
- [108] J. S. Rowlinson, *Liquids and Liquid Mixtures*, Butterworth, London, 1969.
- [109] C. S. Lock, M.S.E. Thesis, Princeton University (2003).
- [110] A. Z. Panagiotopoulos, *J. Chem. Phys.*, **116**, 3007 (2002).
- [111] J. M. Romero-Enrique, G. Orkoulas, A. Z. Panagiotopoulos, and M. E. Fisher, *Phys. Rev. Lett.*, **85**, 4558 (2000).
- [112] J. M. Romero-Enrique, L. F. Rull, and A. Z. Panagiotopoulos, *Phys. Rev. E*, **66**, 041204 (2002).
- [113] J. O. Hirschfelder, C. F. Curtiss, and R. B. Bird, *Molecular Theory of Gases and Liquids*, John Wiley and Sons, Inc., 1967.
- [114] J. R. Errington and A. Z. Panagiotopoulos, *J. Chem. Phys.*, **111**, 9731 (1999).
- [115] A. L. R. C. Vega, *J. Chem. Phys.*, **105**, 4223 (1996).
- [116] A. L. Rodriguez and J. J. Freire, *Mol. Phys.*, **63**, 591 (1988).
- [117] M. E. Fisher and B. Widom, *J. Chem. Phys.*, **50**, 3756 (1969).

- [118] M. E. Fisher, unpublished work reported at the Second Eastern Theoretical Physics Conference, Chapel Hill, N.C., 25 October 1963 and at the Institut des Hautes Etudes Scientifiques, Bures-sur-Yvette, Paris, 26 April 1965.
- [119] F. Gursev, Proc. Camb. Phil. Soc., **46**, 182 (1950).
- [120] Z. W. Salsburg, R. W. Zwanzig, and J. G. Kirkwood, J. Chem. Phys., **21**, 1098 (1953).
- [121] R. Kikuchi, *ibid.*, **23**, 2327 (1955).
- [122] J. L. Lebowitz, J. K. Percus, and I. J. Zucker, Bull. Chem. Phys. Soc., **7**, 415 (1962).
- [123] S. Katsura and Y. Tago, J. Chem. Phys., **48**, 4246 (1968).
- [124] M. Kac, G. E. Uhlenbeck, and P. Hemmer, J. Math. Phys., **4**, 216 (1963).
- [125] J. L. Lebowitz and O. Penrose, *ibid.*, **4**, 248 (1963).
- [126] P. M. Bleher and F. J. Dyson, Commun. Math. Phys., **160**, 493 (1994).
- [127] P. M. Bleher, F. J. Dyson, and J. L. Lebowitz, Phys. Rev. Lett., **71**, 3047 (1993).
- [128] P. M. Bleher, Z. Cheng, F. J. Dyson, and J. L. Lebowitz, Commun. Math. Phys., **154**, 433 (1993).
- [129] Y. C. Kim, M. E. Fisher, and E. Luijten, Phys. Rev. Lett., **91** (2003).